Orbital Dynamics in Galaxy Clusters

Marcel Christopher Lotz

Munich 2017

Bahndynamiken in Galaxienhaufen

Marcel Christopher Lotz

München 2017

Faculty of Physics
Ludwig Maximilian University, Munich

Master Thesis in Physics
submitted by

Marcel Christopher Lotz

Matriculation Number: 11264745

born on the 16th December, 1991
in Frankfurt am Main, Germany

Conducted at the
University Observatory in Munich in Computational Astrophysics

supervised by
Dr. Rhea-Silvia Remus and Dr. Klaus Dolag

Munich 2017

Abstract

The effect of galactic orbits on a galaxy's internal evolution within a galaxy cluster environment has been the focus of heated debate in recent years. To disentangle this relationship, we investigate the phase space, the orbital evolution and the velocity anisotropy of cluster satellites. Through the use of the hydrodynamic cosmological simulation Magneticum Pathfinder, we evaluate the orbits of subhalos associated with 20 clusters. Thus, we are able to achieve a statistically relevant sample of galaxies inside clusters, which we further split into quiescent and star forming galaxies. This split allows us to observe the internal galactic evolution and study its dependence on the radial distance and anisotropy parameter. We then extend our investigation and consider the evolution from high redshift to present day. This allows us, amongst other considerations, to relate infalling galaxies with their progenitors, so as to understand the star formation history. To evaluate the validity of the simulation-based findings, we compare, where possible, with observations. We find that at redshifts $z < 0.5$ the vast majority of galaxies are quenched through ram-pressure stripping during their first passage.

Contents

Chapter 1

Introduction

1.1 Historical Context

The first recorded observation related to galaxies was made by Democritus in the 5th century BC. He postulated that the distinguishable bright band in the night sky might consist of stars. Eventually, the milky band became known as the Milky Way. However, many centuries later, there was dispute regarding the expanse of the Milky Way. On 26 April, 1920 the dispute unfolded into the Great Debate. Arguing that the Universe was completely composed of the Milky Way, Shapley opposed Curtis, who believed the universe consisted of several separate 'island universes', a term coined by Immanuel Kant. As a result of Edwin Hubble's work, a major paradigm shift occurred, mostly proving Curtis correct (Trimble, 1995). Years later, in 1936, Hubble published the now famous classifications of galaxies. During the 20th century, the field of study rapidly expanded and countless galaxies of varying size, distance and type were discovered.

The scientific knowledge today far extends beyond the revelations of the 20th century. The current paradigm indicates that there are $2 \cdot 10^{12}$ (two trillion) galaxies in the universe up to a redshift of $z = 8$, albeit most are far less massive than the Milky Way (Conselice et al., 2016). These galaxies are distributed through the diverse environments of the observable universe. They inhabit the most dense galaxy clusters as well as the lowest density field environments. As such, they are the fundamental building blocks of cosmological structure and the birthplace of the vast majority of stars.

1.2 Fundamentals of Galaxies

Galaxies have numerous properties, but historically have been classified into two broad types: ellipticals and spirals. The rich variety of galaxies allows for a multitude of evolutionary sequences. Generally, spirals are formed and, through a number of mechanisms involving accretion and interactions, evolve into ellipticals. Independent of the type, a galaxy consists of four distinct regions.

1. The inner part of a galaxy consists of a central **bulge**, which has a super-massive black hole at its center. This region is typically the hottest and most

dynamic part of the galaxy.

2. The central region is encompassed by either a **thin rotating disc** (spiral) or a **spheroidal** (elliptical) stellar component. Independent of the shape, this component is typically far more extensive than the inner region. If star formation occurs, it happens predominantly in the disc.

3. The previous two regions are what is typically associated with a galaxy due to the vast majority of the light originating from these parts. However, the galaxy itself is enveloped by a **galactic gas halo**. The galaxy and its halo interact in an intricate manner, much of which is still very much a topic of research and debate. Nevertheless, it is evident that long-term star formation is supplied by gas accreted from the halo onto the disc. These three distinct regions make up the baryonic component of a galaxy.

4. The baryonic component of the galaxy is, in turn, situated at the center of the **dark matter halo**. In the case of the Milky Way the dark matter halo is responsible for 95% of the galaxy's mass (Battaglia et al., 2005; Kafle et al., 2014).

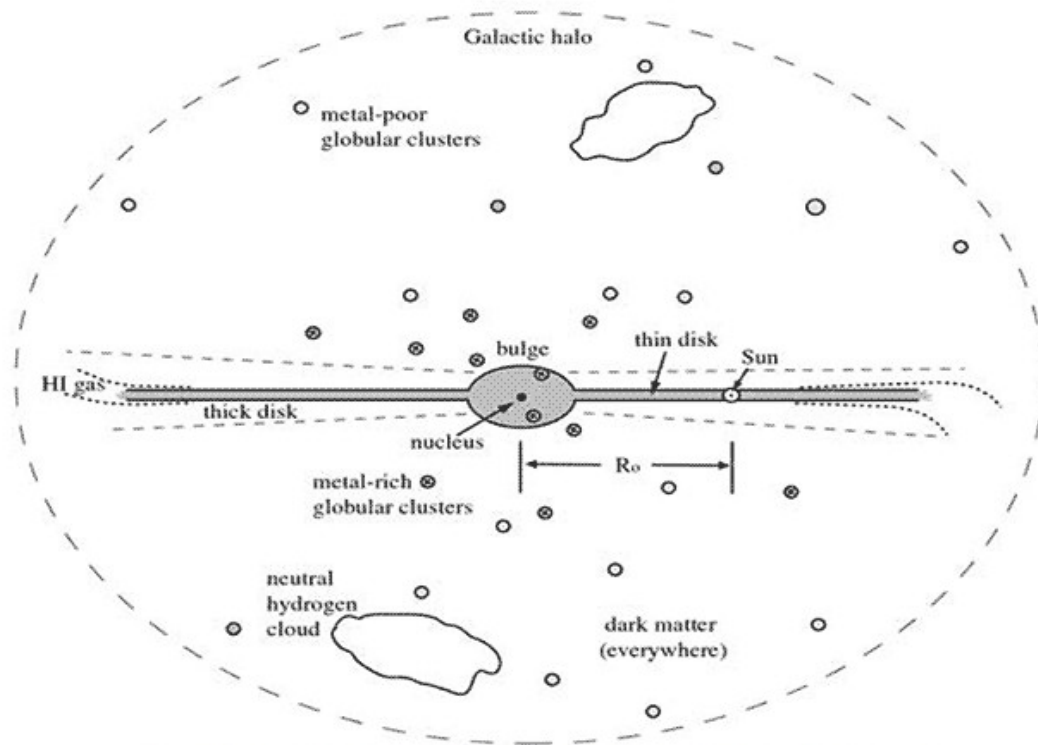

Figure 1.1: Baryonic components of the Milky Way. Figure from GAIA ESO.

Broadly speaking, the difference between spherical and elliptical galaxies can be reduced to whether they are dominated by rotation (spiral) or dispersion (elliptical).

Historically, galaxies were differentiated by color; spirals being blue (star forming) and ellipticals being red (quiescent).

Spiral galaxies are able to form due to the dissipative properties of gas. In contrast to stars or dark matter, gas is able to redistribute its angular momentum and, subsequently, settle into the energetically favourable state of a disc. Through interaction and feedback, the spiral galaxies evolve into ellipticals. Essentially, the low energetic state with aligned angular momentum (disc) is excited to a higher energetic state (spheroid).

1.2.1 Hubble Classifications

In contrast to the current understanding, namely that spirals evolve into ellipticals, the historical classification was exactly contrary to this paradigm. Edwin Hubble believed that ellipticals evolve into spirals as depicted in Figure 1.2 (Hubble, 1926). As a result, ellipticals are often referred to as early-type galaxies, while spirals are considered to be late type galaxies. Despite the evolutionary sequence being reversed, the classifications are still widely used today.
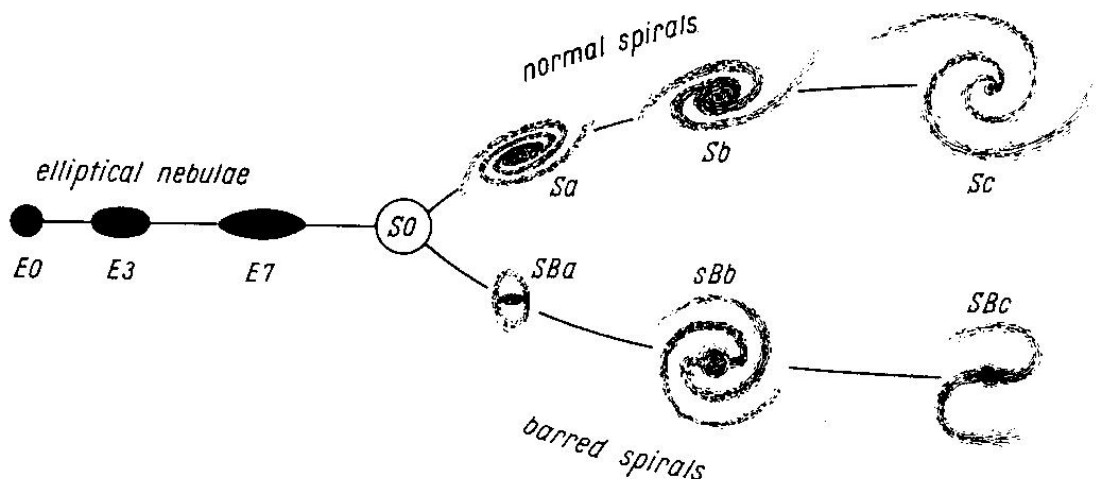
Figure 1.2: Historic Hubble Classifications. On the left elliptical galaxies are depicted, historically referred to as elliptical nebulae. The right side shows normal and barred spirals respectively. Historically, the left are called early-type and the right late-type galaxies. Figure from Hubble (1936).

The classification is primarily based on galaxy morphology. Apart from the two dominant types there exists a third type, namely the lenticular galaxy (S0). This intermediate galaxy is a disc galaxy which no longer has a sufficient amount of interstellar medium (ISM) to sustain star formation. Ellipticals and lenticulars share spectral properties and scaling relations and are thus both considered early-types.

1.2.2 Morphology-Density Relationship

The study of galaxies is always also a study of their environments. A cornerstone of this interlaced subject is the morphology-density relationship. It links the abundance of a specific subset of galaxies to their environment, characterized by the local

density. Hence, it shows a clear correlation between the morphology of a galaxy and its environment.

When considering Figure 1.3, it becomes evident that spiral and irregular galaxies are far more frequent in isolated regions of the universe. In addition, both lenticulars and ellipticals are most abundant in clusters. When considering the current paradigm of galaxy evolution, the following conclusion becomes apparent.

1. Spirals form in low density regions

2. These regions, through time, collapse

3. Mechanisms driven by higher density environments facilitate the evolution of spirals into lenticulars and ellipticals respectively

4. As a result, overdense regions are populated with elliptical type galaxies

This observation by Dressler (1980), shown with up-to-date data in Figure 1.3, essentially became one of the foundations of the current paradigm of galaxy evolution. The process by which spirals evolve into lenticulars and ellipticals respectively is currently one of the most dynamic fields of study within astrophysics. The different evolutionary processes, with an emphasis on the high density cluster environment, are discussed in 1.2.5.

1.2.3   Virial Theorem and Critical Density

To better understand, and, subsequently, disentangle the relationship between a galaxy and its environment, the need for the quantisation of certain observables arises. A natural choice for the parametrisation of the extent of a galactic object is the virial radius, r_{vir}. The virial radius is a quantity derived from the virial theorem:

$$2\langle T \rangle = k \langle U \rangle$$

The theorem connects the average kinetic energy $\langle T \rangle$ with the average potential energy $\langle U \rangle$ of a system via the power k of the potential's radial dependence. In the case of the gravitational potential, $k = -1$. When substituting the kinetic and gravitational potential energy into the virial theorem, it states:

$$\frac{GM}{R} = v^2 \approx \sigma^2,$$

with gravitational constant G, mass M, radius R, velocity v and velocity dispersion σ. The virial radius is defined as the radius at which the velocity dispersion is maximal, subsequently the virial mass is defined as the mass enclosed by the virial radius.

$$R_{vir} \equiv \frac{GM_{vir}}{\sigma^2_{max}}$$

For facilitated application, the virial radius definition is often interchangeably used with the critical radius or r_{200}. This radius is defined with regard to the critical density; the matter density of a spatially flat universe:
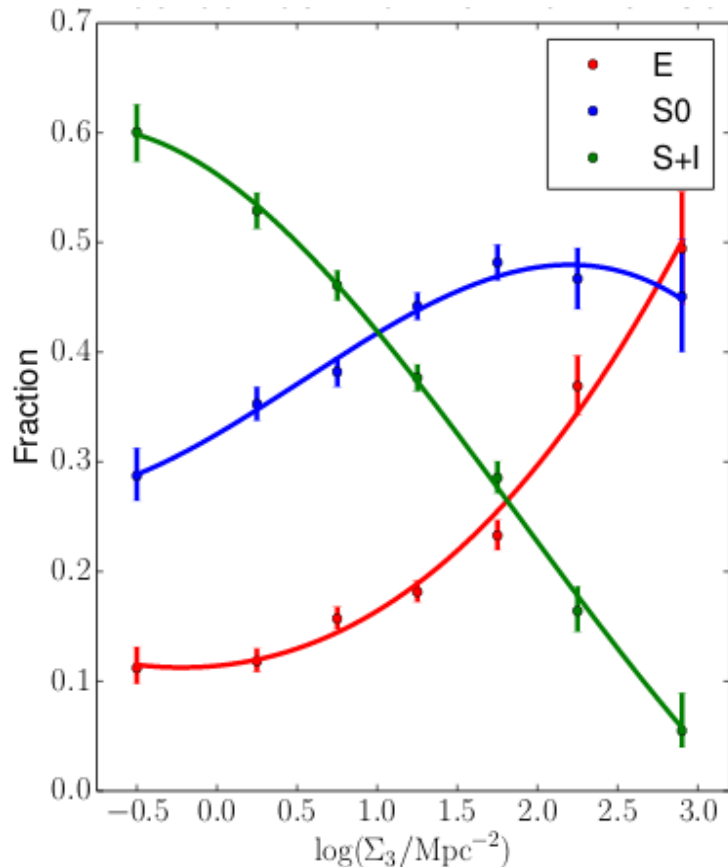
Figure 1.3: Reproduction of the morphology-density relation of Dressler (1980) using up-to-date cluster observations, projected densities to the third nearest neighbour and field-edge or completeness corrections. The morphology-density relation is shown for elliptical galaxies (E), lenticulars (S0) and spirals and irregulars (S+I). Figure from Houghton (2015).

$$\rho_c = \frac{3H^2}{8\pi G}$$

Given the critical density, r_{200} is defined as the radius of the sphere, centred at the minimum of a given potential well, with mass overdensity 200 times the critical density at a given redshift.

The virial velocity is a quantity which gives an impression of typical velocities within a bound system. It is defined as function of virial mass and radius:

$$v_{vir} \equiv \sqrt{\frac{GM_{vir}}{R_{vir}}}$$

1.2.4   NFW Profile

The study of galaxies and galaxy clusters demands the consideration and explanation of the NFW profile. The Navarro-Frenk-White (NFW) profile is a radial density distribution fitted to dark matter in N-body simulations (Navarro et al., 1997). It

characterizes the mass distribution along the radius and is the commonly used profile to describe dark matter halos.

The radial density distribution $\rho(r)$ states:

$$\rho(r) = \frac{\rho_c}{\frac{r}{r_s}\left(1 + \frac{r}{r_s}\right)^2},$$

where ρ_c and the scale radius R_s are free parameters, which are fitted to individual halos. When integrating along the radius, the mass M within a given radius R_{max} is:

$$M = \int_0^{R_{\max}} 4\pi r^2 \rho(r)\, dr = 4\pi\rho_c R_s^3 \left[\ln\left(\frac{r_s + R_{\max}}{R_s}\right) - \frac{R_{\max}}{r_s + R_{\max}}\right]$$

It is to be noted that the total mass diverges; however, considering the R_{200} radius at the edge of a halo provides a meaningful definition:

$$R_{200} = cr_s$$

specifically, it allows an expression in terms of the concentration parameter c and the scale radius r_s. This becomes useful when the necessity arises of comparing complex cosmological structures. In order to deduce inherent quantities like the R_{200} radius, the NFW profile is fitted to a structure, e.g. a cluster, yielding a facilitated method of calculation.

1.2.5   Cluster Environment and Quenching

The relationship between a galaxy's properties and its environment becomes distinctly evident in dense, hot galaxy clusters. A wide variety of quenching mechanisms, i.e. processes inhibiting star formation, are readily available in a cluster environment, including: strangulation, ram-pressure stripping and tidal effects. Galaxies in a cluster environment are, hence, far more likely to have reduced star formation in comparison to 'field' galaxies, i.e. galaxies in less dense environments (Oemler, 1974; Butcher & Oemler, 1978; Dressler, 1980).

The goal of current studies, be they observationally or computationally based, is to disentangle the relative importance and effectiveness of the aforementioned environmental quenching mechanisms. Competing theories weight their relative importance differently. In order to shed light on these mechanisms, an overview is required:

1. Both minor and major **galaxy mergers** are considered most important in less massive environments than clusters. This is due to the high velocity dispersion present in massive systems (Iannuzzi, 2012). Although clusters are dense, the high velocity dispersion of the galaxies does not allow for sufficient contact time, thus inhibiting mergers. In less dense environments however, mergers are a predominant driver of morphological change and hence inevitably impact the star formation (Toomre & Toomre, 1972; Farouki & Shapiro, 1981).

2. The aforementioned high-speed encounters are called **harassment**. Harassment is a driver of strong morphological evolution, easily capable of transforming spirals to ellipticals (Moore et al., 1996). Galaxies do not necessarily experience strong individual high speed encounters, nonetheless, the frequency of high speed encounters in combination with the effects of a clusters global potential is sufficient to have a major impact on galaxy morphology (Moore et al., 1998).

3. In contrast, **strangulation** is associated with galaxies being accreted onto a larger structure. Explicitly, strangulation is the mechanism that removes the hot gas halo enveloping a galaxy (Larson et al., 1980; Iannuzzi, 2012). The subsequent disruption of gas inflow, associated with becoming a satellite of a larger system, leads to a cold gas deprivation within the galaxy and hence the quenching of star formation on long time scales (Weinmann et al., 2006; van den Bosch et al., 2008; Weinmann et al., 2009; von der Linden et al., 2010).

4. Similarly, **starvation** describes the heating of the extended hot gas reservoir required for the continuous supply of star formation. Rather than experiencing the removal of the outer gas halo, galaxies quenched through starvation do not undergo constant rejuvenation. Explicitly, this entails a similar deprivation of cold gas within the galaxy however, the underlying reason driving the lack of fresh cold gas is different. Starvation typically occurs in low density environments, i.e. field galaxies, where the existing reservoir of cold gas is consumed and not renewed. Strangulation and starvation are often used interchangeably to describe processes in which no fresh gas reaches the inner galaxy (Treu et al., 2003).

5. **Ram-pressure stripping** is an escalation of strangulation; it is the process whereby the cold gas component is progressively stripped from the galaxy. This process is especially important in massive clusters with high density intra-cluster medium (ICM), which essentially strips the galaxy while it moves through the cluster (Gunn & Gott, 1972). High pressure and steep pressure gradients within clusters result in the gas effectively being pushed from the galaxy, while the stellar and dark matter component continue on the original trajectory. The impact of ram-pressure stripping is demonstrated by observations in Figure 1.4.

6. Lastly, **tidal effects** represent a different type of mechanism, namely: gravitational interaction. The gravitational interaction occurs both between galaxies and between galaxies and the cluster potential. As a consequence, galaxies are heated, partially stripped and ultimately torn apart, provided the tidal effects are strong enough (Richstone, 1976; Moore et al., 1996).

Apart from quantifying the relative importance of varying quenching mechanisms, another aim in galaxy cluster research is to quantify the regions in which they act. Recent observations have established that galaxy cluster environments extend out to $r \sim (2-3) R_{vir}$, much further than previously assumed (Balogh et al., 2000; Solanes et al., 2002; Verdugo et al., 2008; Braglia et al., 2009; Hansen et al.,
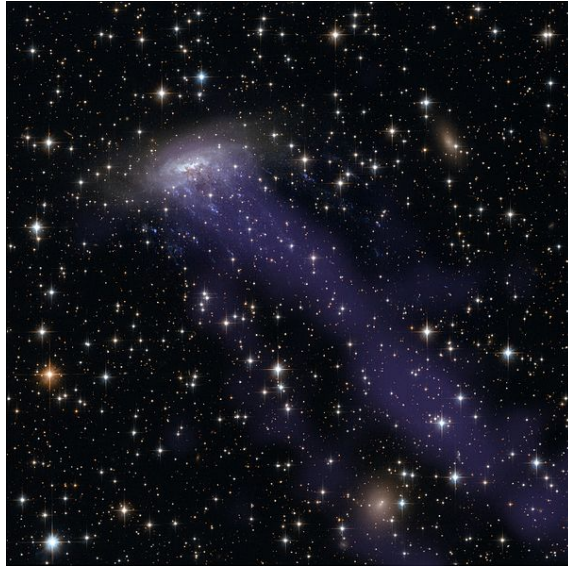
Figure 1.4: Observation of a jellyfish galaxy undergoing violent ram-pressure stripping in the Norma Cluster. Figure from NASA, ESA, CXC.

2009; von der Linden et al., 2010; Wetzel et al., 2012). An overview of the regions in which the different mechanisms are presumed to be effective is given in Figure 1.5. The diagram allows a crude a priori evaluation of radial relevance of varying mechanisms on the basis of a sole cluster studied in Treu et al. (2003).

In an attempt to understand quenching mechanisms, it is useful to differentiate between gravitational, hydrodynamic and hybrid processes. Tidal interactions, harassment and mergers fall into the former category. On the other hand, any kind of stripping or evaporation mechanisms, i.e. interactions between the Interstellar Medium (ISM) and the hot Intracluster Medium (ICM), are considered hydrodynamic quenching mechanisms. Lastly, combinations of the two, such as strangulation, fall into the latter category, namely hybrid processes (Mercurio et al., 2014).

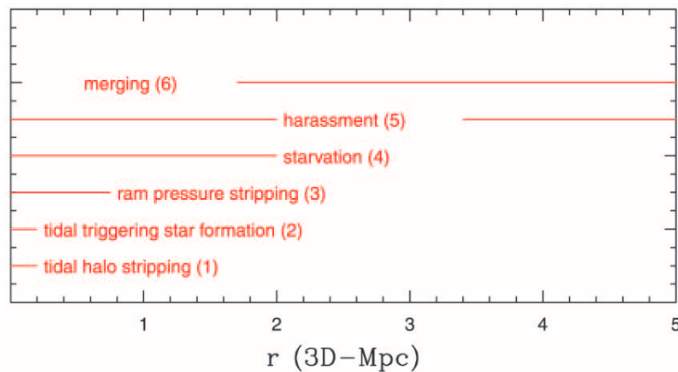**Figure 1.5:** Summary of the regions where key physical quenching mechanisms are likely to operate. For reference, the virial radius is $r_{vir} = 1.7\,\mathrm{Mpc}$ and the cluster studied is located at $z \approx 0.4$. Figure from Treu et al. (2003).

Computational research by Zinger et al. (2016a) suggests that star formation is quenched $2-3\,\mathrm{Gyr}$ prior to entry to the inner cluster halo. This implies that galaxies

are quenched through starvation in the outskirts $r \sim (2-3)\,\mathrm{R_{vir}}$ of the cluster by crossing the accretion shock. The accretion shock is an X-ray emitting region that has been shock heated to $10^7 - 10^8 K$ and is in near hydrostatic equilibrium within the potential well of the cluster (Sarazin, 1988). Once the infalling galaxies enter the inner region $r \lesssim 0.5\mathrm{R_{vir}}$ the removal of star-forming disc gas becomes efficient too (Zinger et al., 2016a).

Essentially, this means that hot halo gas is removed prior to the gas within the galaxy being affected (Larson et al., 1980; McCarthy et al., 2008; Bekki, 2009; Bahé et al., 2013). This suggests that the primary quenching mechanism at radii $r \gtrsim 0.5\,\mathrm{R_{vir}}$ is strangulation, meaning that the cold gas is not necessarily expelled or significantly heated but rather the supply in the halo is affected and thus star formation dwindles due to lack of fresh halo gas (Kawata & Mulchaey, 2008). This assumption would imply a gradual decrease in star formation until the galaxies move into the inner region, followed by rapid shutdown once ram-pressure stripping becomes effective.

How efficient, in what region and due to what mechanisms star formation is quenched in a cluster environment is a topic of continuous debate. One of the goals of this thesis is to trace the infalling galaxies and link their orbits to their star formation with an unprecedented resolution provided by the Magneticum Pathfinder simulation.

1.3 Velocity Anisotropy

One of the fundamental quantities under consideration during this thesis is the velocity anisotropy, β. The goal of parametrising and comparing objects through the use of the velocity anisotropy is to gain an understanding of the relative importance of different degrees of freedom. At its core this means linking a certain preference for a degree of freedom with another quantity and understanding the physical implication. Thus, the velocity anisotropy gains its physical significance by comparing and contrasting different subsets of a given population.

Less abstract, the velocity anisotropy is a measure of directional dependence in a given axis. In the spherical coordinate system the directional dependence translates into three degrees of freedom, two of which can be classified together. The tangential component is made of both the θ and ϕ component and, as the name suggests, describes the tangential orbital motion of a given object. The third component of the spherical coordinate system is the radial component parametrising radial orbital movement.

In order to contrast the tangential and radial orbital component, the respective velocity dispersions are considered. Dispersion is a measure of the degree of energy within a given component. If a population is dominated by tangential or radial movement the dispersion in the respective degree of freedom will be larger.

As such, quantifying the energy within a degree of freedom through the velocity dispersion σ is a natural choice, as it relates to the kinetic energy T through (see section 1.2.3):

$$T \propto \frac{3}{2}\sigma^2$$

In accordance with the explanation above, the formal definition of the velocity dispersion is:

$$\beta \equiv 1 - \frac{\sigma_t^2}{\sigma_r^2},$$

$$\text{with } \sigma_t^2 = \frac{\sigma_\theta^2 + \sigma_\phi^2}{2}.$$

where σ_r, σ_t, σ_θ and σ_ϕ parametrise the velocity dispersions in the radial, tangential, θ and ϕ direction respectively.

The velocity anisotropy ranges from $-\infty$ to 1. The three different extreme cases are listed below:

$$\beta \approx -\infty \text{ purely circular}$$

$$\beta \approx 0 \text{ isotropy}$$

$$\beta \approx 1 \text{ purely radial}.$$

The first case, namely the purely circular case, occurs when there is no dispersion within the radial component, provided there being a tangential dispersion. The second state implies that the two degrees of freedom, tangential and radial, are equally favoured. More specifically, isotropy denotes the case in which all directions have the same properties. The last, purely radial, case is the consequence of a lack of tangential dispersion. The orbits would then be maximally radial, merely oscillating within the potential.

With regard to the limitations of the anisotropy, the consideration of the velocity anisotropy is only of use when an object is moving on a bound orbit. Otherwise, the concept of a circular or radial orbit extinguishes.

1.3.1   Jeans Equation

Commonly, the Jeans equation describes the movement of a population of stars within a gravitational field. These continuity equations are the analogon of the Euler equations in the case of fluid flow. The first derivation from the collisionless Boltzmann equation is ascribed to James Clerk Maxwell. However, James Jeans first applied the equations to the stellar case.

Consider a stellar density $n(x, t)$ as a function of space x and time t, then the first Jeans equation can be expressed as:

$$\frac{\partial n}{\partial t} + \sum_i \frac{\partial (n \langle v_i \rangle)}{\partial x_i} = 0$$

We observe that the stellar density can be expressed in terms of the velocity v. When additionally considering the gravitational potential $\Phi(x, t)$, we can state the second Jeans Equation:

$$\frac{\partial(n\langle v_j\rangle)}{\partial t} + n\frac{\partial \Phi}{\partial x_j} + \sum_i \frac{\partial(n\langle v_i v_j\rangle)}{\partial x_i} = 0, \qquad (j = 1, 2, 3).$$

An advantage of the Jeans equation is that it can be inverted to yield velocity anisotropies from observations (Biviano et al., 2013). This, in turn, allows the comparison between velocity anisotropies attained through observations and those calculated via simulation. In addition, the Jeans equations are not limited in their application to stars, but rather can also be applied to galaxies. The above equations are then adapted to employ galactic instead of stellar densities. This, hence, enables a meaningful comparison between simulated and observed anisotropies.

1.3.2 Anisotropy Profile

Combining the velocity anisotropy with the NFW profile and the Jeans equation yields an analytic description of the mass dependent anisotropy profile. To understand this fundamental relationship, we consider the pseudo phase space density ρ from Taylor & Navarro (2001):

$$\frac{\rho}{\sigma_r^{\,3}} = \frac{\rho_s}{\sigma_{r,s}^{\,3}} x^{-\alpha}$$

The pseudo phase space density is described here by a power law with negative gradient α, radial velocity dispersion σ_r, dimensionless radius $x = r/r_s$, scale density ρ_s and the corresponding value at the scale radius r_s (Ludlow et al., 2011). This equation hence allows the determination of the radial velocity dispersion. With this relationship and the Jeans equation, the anisotropy parameter can be calculated as (Binney & Tremaine, 2008):

$$\beta(x) = \frac{5}{6}\gamma(x) - \frac{\alpha}{3} - \frac{GM(x)}{2xr_s\sigma_r^{\,2}(x)}$$

This results in a relationship linking the anisotropy parameter with both the mass profile and the radial velocity dispersion via $\gamma \equiv -d\,log(\rho)/d\,log(x)$. This means that if observers assume a mass distribution and subsequently invert the Jeans equations they are able to calculate the velocity anisotropy. As such this expression establishes an essential relationship between significant quanitites with a minimum amount of assumptions.

1.4 Overview of Cosmology

1.4.1 Geometry

Observations lead us to believe that from our point of view the universe is isotropic. Combining this observation with the assumption of the Copernican Principle, that we are not at an exceedingly unique place in the universe, we arrive at the Cosmological Principle. It states that the universe must appear isotropic from every point of observation. It is to be noted that this has not been rigorously demonstrated however, we will, for now, assume this to be true (Clarkson, 2012). The assumption

is justified by the strong support of uniformity that the Cosmic Microwave Background (CMB) provides, as illustrated by Figure 1.6. The CMB is a remanent from the early epoch of the universe, i.e. from around $380,000$ years after the Big Bang and, hence, originates from the period of time when inflation ended (Bennett et al., 2003).

The importance of the assumption of the Cosmological Principle becomes evident when considering general relativity. The assumption allows the derivation of the Friedmann equations (Friedmann, 1922). These field equations govern the expansion of space; specifically, their time evolution is intrinsically intertwined with the curvature of the universe. The geometric properties of the universe, namely isotropy and homogeneity, dictate the general form of the exact solution, i.e. a given metric (Robertson, 1935). A universe which abides by the Cosmological Principle reduces the possible space-time metrics to the Friedmann-Lemaître-Robertson-Walker metric (Walker, 1935):

$$ds^2 = (cdt)^2 - dl^2 = (cdt)^2 - a(t)^2 \left[\frac{dr^2}{1 - Kr^2} + r^2(d\theta^2 + \sin^2(\theta d\phi^2)) \right]$$

with comoving spherical coordinates r, θ and ϕ, cosmic time t, cosmic scale factor $a(t)$ and curvature parameter K. Einstein's field equations are not needed for the form of the metric, but are solely required for the derivation of the scale factor $a(t)$. The metric introduces the necessity of the concept of curvature with regard to space-time:

$$K = 0, \texttt{ flat universe}$$
$$K > 0, \texttt{ spherical (closed) universe}$$
$$K < 0, \texttt{ hyperbolic (open) universe}$$

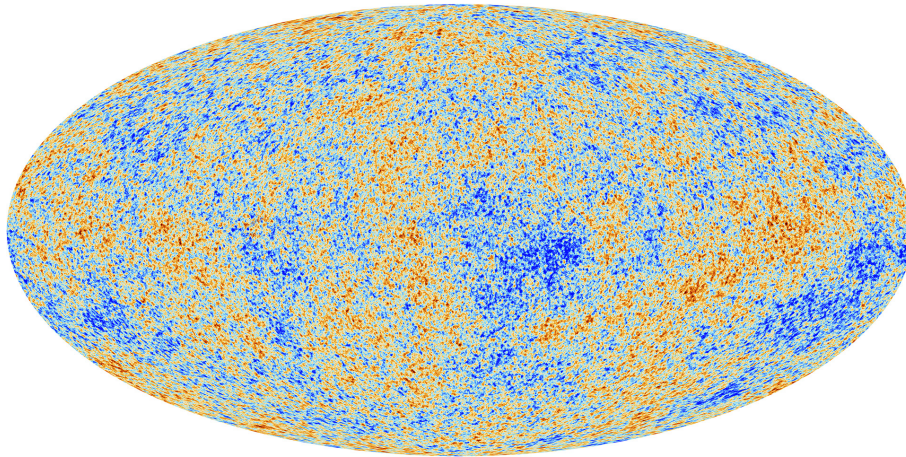**Figure 1.6:** Cosmic microwave background (CMB) as seen by Planck. The CMB has a thermal black body spectrum at a temperature of $2.72548 \pm 0.00057\,\mathrm{K}$ (Fixsen, 2009). Figure from ESA and the Planck Collaboration.

The curvature parameter K can assume three distinct sets of values. These three different cases place limitations on the the topology of the universe. The first case

$K = 0$ demands a flat local geometry. Globally, the flat universe can be compared to the structure of Euclidean space. Irrespective of the presence of dark energy, a flat universe continues expansion forever. Dark energy merely influences the rate of the expansion. With dark energy, the rate of expansion accelerates continuously, whereas without dark matter the rate of expansion slows down.

The positive curvature case characterizes a closed, spherical universe. As the name suggests, the spherical universe implies a four dimensional space-time hypersphere. In this case the scale factor increases to a maximum value and then decreases back to zero. The final, negative curvature case is best illustrated by a four dimensional, infinitely extended saddle. In contrast to the closed case, this hyperbolic, open universe expands at an accelerating rate.

The Planck observations have found the observable universe to be flat within the standard 6 parameter ΛCDM cosmology, the dominant model describing the evolution of the universe (Planck Collaboration et al., 2016). However, the universe could easily extend beyond observations, signifying that only the local universe is flat. This is analogous to an individual perceiving the earth as flat, whereas from a more distant point of observation this misconception is exposed.

1.4.2   Dynamics

The observation that the universe is expanding at an accelerated rate directly implies that at previous times the universe was smaller. This is the underlying reasoning behind Hubble's law and thus the Big Bang Theory. Hubble's Law states that the relationship between distance D and recession velocity v is linear and that it scales with the Hubble constant H_0 (Hubble, 1936).

$$v = H_0 D$$

Despite its name, the law, based on general relativity, was first proposed by Lemaître (1927). Furthermore, Hubble's work is based, in large parts, on measurements provided by Slipher (1917). Nonetheless, it became known as the Hubble constant. However, the term *constant* is misleading since the Hubble constant has a time dependence and thus is rather a parameter. This is characterized by the difference between the Hubble constant at redshift zero H_0 and the formally more correct description of the Hubble parameter $H(t)$:

$$H(t) = \frac{\dot{a}(t)}{a(t)},$$

with scale factor $a(t)$ and its temporal derivative $\dot{a}(t)$. The Hubble parameter is a function of the scale factor. The scale factor (and naturally its derivative) is, in turn, a function of cosmological redshift:

$$z \equiv \frac{\lambda_0 - \lambda_t}{\lambda_t},$$

with λ_t being the wavelength of the radiation emitted at time t and the wavelength observed in the present given by λ_0. This makes cosmological redshift a non-linear

time scale ranging from now $z = 0$ to arbitrary high values asymptotically approaching the beginning of time, i.e. the Big Bang. It is the direct result of a non-static, i.e. expanding, universe.

1.4.3 Structure

As discussed in section 1.4.1, we regard the universe to be isotropic. However, an important distinction must be made; we only consider the universe to be isotropic in every point on large scales, typically $\gtrsim 100\,\text{Mpc}$. On smaller scales the universe appears to have order and the apparent randomness is replaced by filaments of higher density and voids of lower density. In contrast to the observed clustering of matter in the present universe, the CMB suggests that the early universe was nearly homogeneous.

When considering observations and simulations at different cosmological times, the evolution of large structure becomes apparent. Around $300,000$ years after the Big Bang the universe was virtually homogeneous. As time progressed, matter began to cluster, clump and collapse into the structures we observe today. Slight initial over-densities began to attract more matter through gravity. The first galaxies formed and began to group together. Subsequently, the first groups began to cluster. Ultimately, this resulted in the large filamentary structure between voids we observe and successfully simulate today, depicted in Figure 1.7.

1.5 Magneticum Pathfinder

Magneticum Pathfinder is a large scale smoothed-particle hydrodynamic (SPH) simulation that employs a mesh-free Lagrangian method aimed at following structure formation on cosmological scales. It simulates more than 10^{10} particles and the largest box has a volume of $\sim 1\,\text{Gpc}^3$. The simulation includes physical processes ranging from thermal conduction to active galactic nuclei feedback. The astrophysical processes modelled include, but are not limited to:

- Cooling, star formation and winds (Springel & Hernquist, 2003)

- Metals, stellar population and chemical enrichment from AGB (Tornatore et al., 2003, 2006)

- Black holes and AGN feedback (Hirschmann et al., 2014)

- Thermal conduction (Dolag et al., 2004)

- Low viscosity scheme to track turbulence (Dolag et al., 2005; Beck et al., 2016)

- Higher order SPH kernels (Dehnen & Aly, 2012)

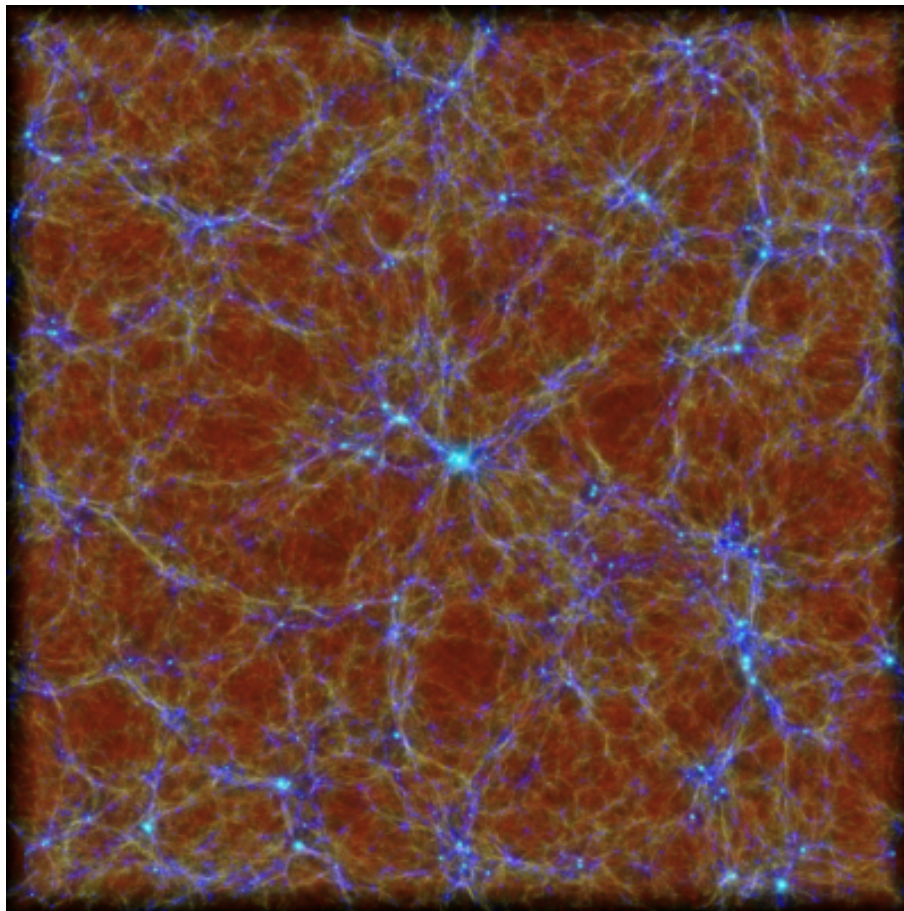- Magnetic fields (passive) (Dolag & Stasyszyn, 2009)

Figure 1.7: A 500 Mpc wide and 70 Mpc thick slice through the baryonic mass distribution of Box2/hr at $z = 0$ in the Magneticum simulation visualized by Sanders et al. (2008). The large filamentary structure is commonly referred to as the cosmic web. Clusters are represented by the blue overdensities, the most massive of which is located at the centre of the figure. Figure from Hirschmann et al. (2014).

For a more in-depth appreciation of the precise physical processes refer to Dolag et al. (2009).

In order to provide an adequate picture of Magneticum Pathfinder, a short overview of simulations in general is required. Simulations are based on cosmological initial conditions like the cosmic microwave background (CMB) provided by observations such as WMAP and Planck as shown in Figure 1.6. They are then limited by final conditions that are provided by observations at low redshift, i.e. of galaxies or, as is the case with Magneticum, of clusters in our local universe. To limit simulations further, there are also integral constraints consisting of cosmological quantities such as star formation rate densities (SFRD) or stellar mass densities (SMD) dependent on redshift referred to as the Madau and Dickinson plot, respectively. (Madau et al., 1996, 1998; Lilly et al., 1996; Dickinson et al., 2003)) In addition, simulations are often further restricted through the extensive study of galaxy evolution at low redshift through surveys like SDSS, COMBO-17 or COSMOS (York et al., 2000). Lastly, simulations are confined by the observations of a multitude of galaxies or clusters at redshift $z \approx 2-3$.

Through the continual adjustment to observations and the adaptation of the underlying code the simulations become more successful in describing the universe. The consistent growth in complexity opens new frontiers and allows insights into ever more complicated and intrinsically intertwined phenomena. Magneticum Pathfinder simulations are in fine agreement with a variety of observations, including AGN population properties (Hirschmann et al., 2014; Steinborn et al., 2015) and dynamical properties of galaxies (Teklu et al., 2015; Remus et al., 2013, 2015, 2017). Especially relevant for the scope of this thesis are the agreements with Planck Collaboration et al. (2013); McDonald et al. (2014) on the pressure profiles of the intracluster medium.
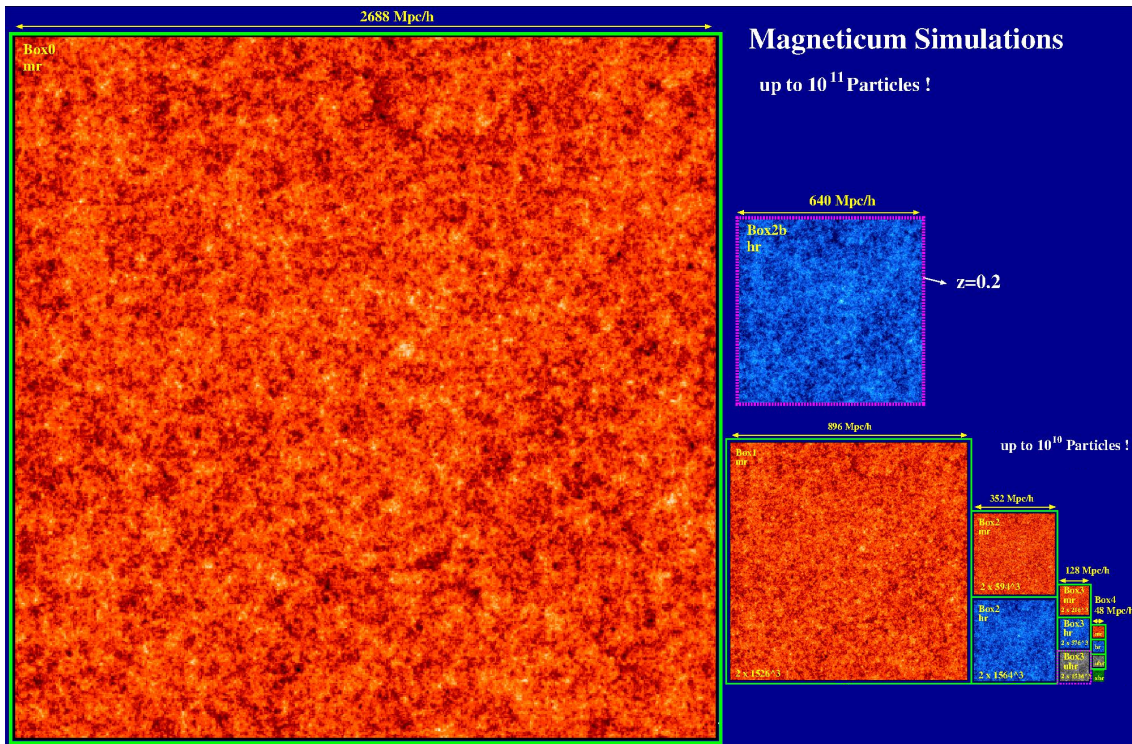
Figure 1.8: Overview of different boxes in Magneticum Pathfinder, scaled to their respective size. The box used throughout this thesis is Box2/hr, located in the bottom right of the figure and indicated by a medium sized blue box. Courtesy of K. Dolag.

The initial conditions of Magneticum Pathfinder are determined by the seven year results of the Wilkinson Microwave Anisotropy Probe (WMAP) and are thus in accordance with the standard ΛCDM cosmology model (Komatsu et al., 2011). Specifically, the Hubble parameter and the matter, dark energy and baryon density parameters respectively are as follows:

$$h = 0.704$$

$$\Omega_M = 0.272$$

$$\Omega_\Lambda = 0.728$$

$$\Omega_b = 0.0451$$

A fluctuation amplitude normalization at $8\,\mathrm{Mpc}$ of $\sigma_8 = 0.809$ is used. In addition, baryonic acoustic oscillations and their effects are included (Teklu et al., 2015).

Figure 1.8 depicts the different boxes simulated in the Magneticum Pathfinder simulation, scaled to their respective sizes. During this thesis Box2/hr was used, which, among other Magneticum boxes, is depicted in Figure 1.8. In Box2/hr each dark matter particle has a mass of $6.9 \cdot 10^8\,\mathrm{M_\odot}/\mathrm{h}$. Gas and stellar particles begin with an initial mass of $1.4 \cdot 10^8\,\mathrm{M_\odot}/\mathrm{h}$ and $\sim 3.5 \cdot 10^7\,\mathrm{M_\odot}/\mathrm{h}$, respectively. The gas and stellar particle mass is not fixed during the simulation. Feedback, e.g. from stars, is able to increase the mass of surrounding gas particles. Subsequently, the stellar particle mass depends on the original gas particle. Each gas particle is able to form four stellar particles, which each depend on the individual gas particle history. In total there are $2 \cdot 1584^3$ particles in the Box2/hr run. Box2/hr was used since the box is still big enough to allow for a sufficiently large statistical sample of galaxy clusters, while also having a high resolution and thus being able to simulate meaningful physics on galactic scales.

Chapter 2

Independent Observations and Models

In order to be able to evaluate Magneticum and its results with regard to clusters within a broader context, comparisons are required. The n-body simulation Millennium and the *C*luster *L*ensing *A*nd *S*upernova survey with *H*ubble (CLASH) offer an opportunity to contrast both to previous simulations and current observations.

These two comparisons are chosen primarily because the velocity anisotropy profiles have been calculated in both cases. Iannuzzi (2012) has computed the velocity anisotropy of a stacked cluster in the Millennium simulation. Currently, only one of the 25 CLASH clusters has been investigated with regard to its velocity anisotropy. This was conducted by Biviano et al. (2013) and the cluster in question is depicted in Figure 2.1.

2.1   State of the Art Observations

CLASH observes 25 massive galaxy clusters with the Hubble Space Telescope's panchromatic imaging equipment (Wide-field Camera 3, WFC3, and the Advanced Camera for Surveys, ACS) (Mercurio et al., 2014). One of four primary science goals of CLASH is the study of internal structure and galaxy evolution within and behind the clusters. This is the reason why the survey is the ideal candidate for comparisons with the simulated cluster results obtained via Magneticum.

The CLASH cluster under consideration (MACS J1206.2-0847) is located at a redshift of $z = 0.44$. The cluster hosts ~ 600 members and has a mass of $M_{200} = (1.4 \pm 0.2) \cdot 10^{15}\,\mathrm{M_\odot}$ with a concentration of $c_{200} = 6 \pm 1$ (Biviano et al., 2013). The data was obtained by the VLT/VIMOS large program, which aims at constraining the cluster mass profile over the radial range of 0-2.5 virial radii.

The cluster MACS J1206.2-0847 is strikingly important for the considerations of this thesis, since it is to date the sole CLASH cluster for which the velocity anisotropy was calculated for both passive and star forming galaxies. In contrast to Magneticum, the velocity anisotropy from observations is not calculated by simply considering dispersions, but rather through the inversion of the Jeans equation. This is done since velocities and thus dispersions can only be observed along the line of sight with the required accuracy for velocity anisotropy calculations.

Although the exact calculations differ, the existence of these observations allow a direct comparison between state of the art simulations and observations. Through the detailed examination of the kinematics, the understanding of the underlying dynamics is rendered possible. Fundamentally, the velocity anisotropy profiles provide insights into the dynamical history of both clusters and their member galaxies. Hence, the comparison between observations and simulations is vital to review and truly appreciate the similarities and differences.

Figure 2.1: Image depicting the galaxy cluster MACS J1206. This composite colour image also nicely illustrates the effect of gravitational lensing the cluster has on more distant objects. Figure from NASA, ESA, M. Postman (STScI) and the CLASH Team.

2.2   Millennium Comparison

The Millennium simulation initially traced 2160^3, i.e. slightly more than 10 billion, particles. Each of these dark matter particles represents a mass of $\sim 10^9 \, \mathrm{M_\odot}$ (Springel et al., 2005). The galaxy catalogue at the basis of the comparison to Iannuzzi (2012) is obtained from (Guo et al., 2011) and subsequently run on the

Millennium simulation, as described in Springel et al. (2005). All relevant information, including the underlying cosmology, can be viewed in Springel et al. (2005).

In contrast to the previously discussed Magneticum simulation, the Millennium simulation is a n-body simulation (Springel et al., 2005). In order to also consider galaxies, an independent semi-analytic model is used together with the Millennium simulation (Guo et al., 2011). The description 'semi-analytic' refers on one hand to merger trees which provide an analytic basis and on the other to the modelling of astrophysical processes, encompassed in the 'semi' prefix. The astrophysical processes include a wide variety of phenomena: cooling, star formation, supernova and AGN feedback, hot gas stripping and metal enrichment (Guo et al., 2011).

The Millennium simulation does not utilise hydrodynamics because it is a dark matter only simulation, i.e. the direct simulation of baryons is excluded. Nonetheless, deductions of baryonic phenomena are possible via the application of abundance matching (Iannuzzi, 2012). Effectively, dark matter halos are matched with corresponding galaxies extracted from a galaxy catalogue, according to their mass distribution. The abundance matching allows the introduction of baryonic characteristics, such as the previously mentioned astrophysical processes, to the dark matter particles. Similar to other simulations, this high redshift abundance matching is calibrated to achieve desired low redshift attributes. Through this method, baryonic galaxy attributes can be simulated, although the simulation is technically dark matter only.

In contrast to Millennium, Magneticum considers gas as a hydrodynamic fluid, in addition to computing dark matter and stars as a n-body problem. As such, Magneticum offers a more realistic approach to the physics governing the cosmos. Due to the different approach in computing physical phenomena, Millennium allows a valuable comparison to the Magneticum simulation with regard to the calculation of the velocity anisotropy.

Chapter 3

Data Reduction

3.1 Data Sample

Throughout this thesis a wide variety of clusters are used. Depending on the redshift in question, the considered clusters vary. In Table 3.1, the 20 redshift zero clusters are listed. Table 3.2 lists a different sample of clusters at $z = 0.44$. Tables 3.1 and 3.2 depict different samples of clusters because for each redshift the first 20 clusters, according to their halo ID, were chosen. This was done rather than evaluating the same clusters at different redshifts because the high mass end clusters provide a larger statistical sample due to a typically larger number of subhalos. Within the context of simulations, subhalos refer to gravitationally bound objects located within a greater potential well. Hence, they provide the simulated counterpart to observed galaxies.

A sample of 20 clusters exhibits a diverse spread in accretion histories. High mass end clusters need not necessarily continue their mass accretion at the same high rate they have historically displayed. Thus, one needs to decide whether it is desirable to track clusters through time or if separate high mass end samples provide a larger statistical sample. Both the phase space and anisotropy profile evaluations in sections 4 and 6 do not require the tracking of the same clusters. For these considerations it is more important to evaluate the general behaviour of a high mass and hence large statistical sample, rather than to track the same clusters from high to low redshift.

The tracking of clusters through time becomes important when evaluating specific orbital dynamics of subhalos. The individual rather than statistical orbital behaviour of subhalos is governed by the evolution of its host cluster. To truly understand when and where quenching occurs, the same subhalos in the same clusters need to be tracked through time. Hence, the Blueness evolution in section 5 tracks a sample of clusters from $z = 0.54$ to $z = 0.03$. As in Tables 3.1 and 3.2, the 20 first halo IDs were tracked.

Clusters are listed according to their halo ID, which references the internal listing as outputted by the algorithm *SUBFIND*. A relatively tight correlation between halo ID and the virial mass exists. This is due to *SUBFIND* computing the outputs from the Friends of Friends (*FoF*) algorithm (Springel et al., 2001). *SUBFIND* considers gravitationally bound objects rather than evaluating spatial proximity as

Halo ID	Mass [M$_\odot$/h]	Radius [kpc/h]	Velocity [km/s]	# Subhalos
000	1.76e+15	2531	1729	1008
001	1.18e+15	2213	1511	658
002	1.17e+15	2211	1510	726
003	6.17e+14	1786	1220	397
004	1.03e+15	2117	1446	609
005	1.01e+15	2105	1438	647
006	5.81e+14	1750	1195	423
007	9.73e+14	2078	1419	589
008	9.27e+14	2045	1397	608
009	8.15e+14	1959	1338	496
010	6.78e+14	1842	1258	425
011	7.46e+14	1902	1299	420
012	6.80e+14	1844	1259	478
013	7.70e+14	1922	1313	514
014	7.47e+14	1902	1300	511
015	6.68e+14	1833	1252	484
016	7.38e+14	1895	1294	468
017	6.54e+14	1820	1243	417
018	7.53e+14	1908	1303	555
019	7.22e+14	1881	1285	501

Table 3.1: Table of the 20 considered and stacked clusters at $z = 0.03$. The mass, radius and velocity all refer to the respective virial quantities. The # Subhalos refers to the number of subhalos within $1\,\mathrm{R_{vir}}$.

the *FoF* algorithm does (Guo et al., 2011). However, since *FoF* provides the basis on which *SUBFIND* operates, the internal identifications need not necessarily correlate perfectly.

It is important to note that columns two, three and four refer to the the virial mass, the virial radius and the virial velocity respectively. The last column of Table 3.1 lists the amount of subhalos within the virial radius of each cluster. All clusters at redshift $z = 0.03$ have at least a mass of $5.81 \cdot 10^{14}\,\mathrm{M_\odot}$/h. At $z = 0.44$ all clusters have a mass above $2.37 \cdot 10^{14}\,\mathrm{M_\odot}$/h. Although the two tables do not necessarily depict the same clusters, the increase in mass, radius, velocity and number of subhalos is clearly visible.

3.2   From Particles to Subhalos

Magneticum Pathfinder simulates particles and their physics through time. At every time step the particles are then organised according to the *SUBFIND* algorithm

Halo ID	Mass [M$_\odot$/h]	Radius [kpc/h]	Velocity [km/s]	# Subhalos
000	1.50e+15	2681	1551	878
001	7.97e+14	2172	1256	486
002	8.12e+14	2185	1264	563
003	3.46e+14	1644	951	252
004	6.19e+14	1996	1155	371
005	5.17e+14	1880	1088	355
006	4.71e+14	1823	1054	282
007	5.28e+14	1893	1095	385
008	4.70e+14	1821	1054	292
009	4.72e+14	1823	1055	342
010	4.43e+14	1785	1033	252
011	4.16e+14	1749	1012	272
012	3.36e+14	1629	942	232
013	2.37e+14	1449	838	156
014	4.31e+14	1770	1024	318
015	3.90e+14	1712	990	210
016	4.00e+14	1726	999	290
017	3.96e+14	1720	995	259
018	4.10e+14	1740	1006	275
019	2.50e+14	1475	853	174

Table 3.2: Table of the 20 considered and stacked clusters at $z = 0.44$. The mass, radius and velocity all refer to the respective virial quantities. The # Subhalos refers to the number of subhalos within $1\,\mathrm{R_{vir}}$.

and grouped into subhalos (Dolag et al., 2009). These, in turn, are grouped into halos. The data concerning the particles is only saved every four time steps due to its immense size. In contrast, the subhalo information, i.e. the already computationally partially reduced data is saved at every time step. Hence, the subhalo data constitutes the foundation of all the scientific deductions made during this thesis.

The distinction between subhalos and particles in Magneticum Pathfinder and, consequently, in this thesis is an important one. Particles, i.e. gas, dark and stellar matter in the simulation, do not carry as much meaningful information as their local potential, namely the individual subhalos. When considering the orbital dynamics of galaxies, particles are less interesting than the attributes of the local potential and its relation to the global potential of the cluster. Nevertheless, inspecting particles allows a more natural, qualitative view of the intimate dynamics ongoing within a subhalo and by extension the cluster environment. Hence, we begin by considering particles.

To gain an understanding of the spatial distribution of simulated galaxies within a cluster, Figures 3.1 and 3.2 are introduced. Figure 3.1 depicts one of the most massive ($1.2 \cdot 10^{15} \, \mathrm{M_\odot}$) clusters at redshift zero with a virial radius of $2.2 \, \mathrm{Mpc/h}$. The black and blue particles indicate dark and stellar matter respectively. In order to better identify individual subhalos, each subhalo has been encircled by a green or red ring depicting the half-mass radius. Green rings represent stellar subhalos, whereas red rings display dark matter only subhalos. In this sense, a subhalo is nothing more than a local, gravitationally bound overdensity.

To illustrate this point further, orange rings were drawn over each subhalo with the radius linearly scaled to its mass. On average, stellar subhalos have a larger orange ring due to their larger mass. In contrast, the majority of the orange rings of the dark matter only subhalos are so small (~ 1 pixel), that they are effectively invisible. The orange rings were plotted into Figures 3.1 and 3.2 to check the mass rather than the spatial extent of the subhalos.

A relatively large red ring, for example, does not indicate a similar mass as a similar sized green ring. It merely indicates that half of the bound mass lies within a similar radius. In contrast, the orange rings are a measure of the actual mass contained by the subhalo, independent of the spatial distribution. Hence, the orange rings offer the opportunity for a self consistency check, by verifying that dark matter halos typically have far less mass than their stellar counter parts.

The galaxy cluster in Figure 3.2 is undergoing a merger. Not only is it less massive with a mass of $5.8 \cdot 10^{14} \, \mathrm{M_\odot/h}$ than the cluster in Figure 3.1, but it is also less concentrated. Figures 3.1 and 3.2 allow for an appreciation of the level of detail available to the Magneticum Pathfinder simulation. Furthermore, they offer a visual introduction to the following, more abstract, work.

3.3   Investigating the Cumulative Mass Function

The cumulative mass function is introduced as a means of evaluating the quality of the simulation with respect to the clusters considered. Figure 3.3 depicts the cumulative mass function of both the total and stellar population of the subhalos within 20 massive clusters in Box2/hr. The cumulative mass function is calculated
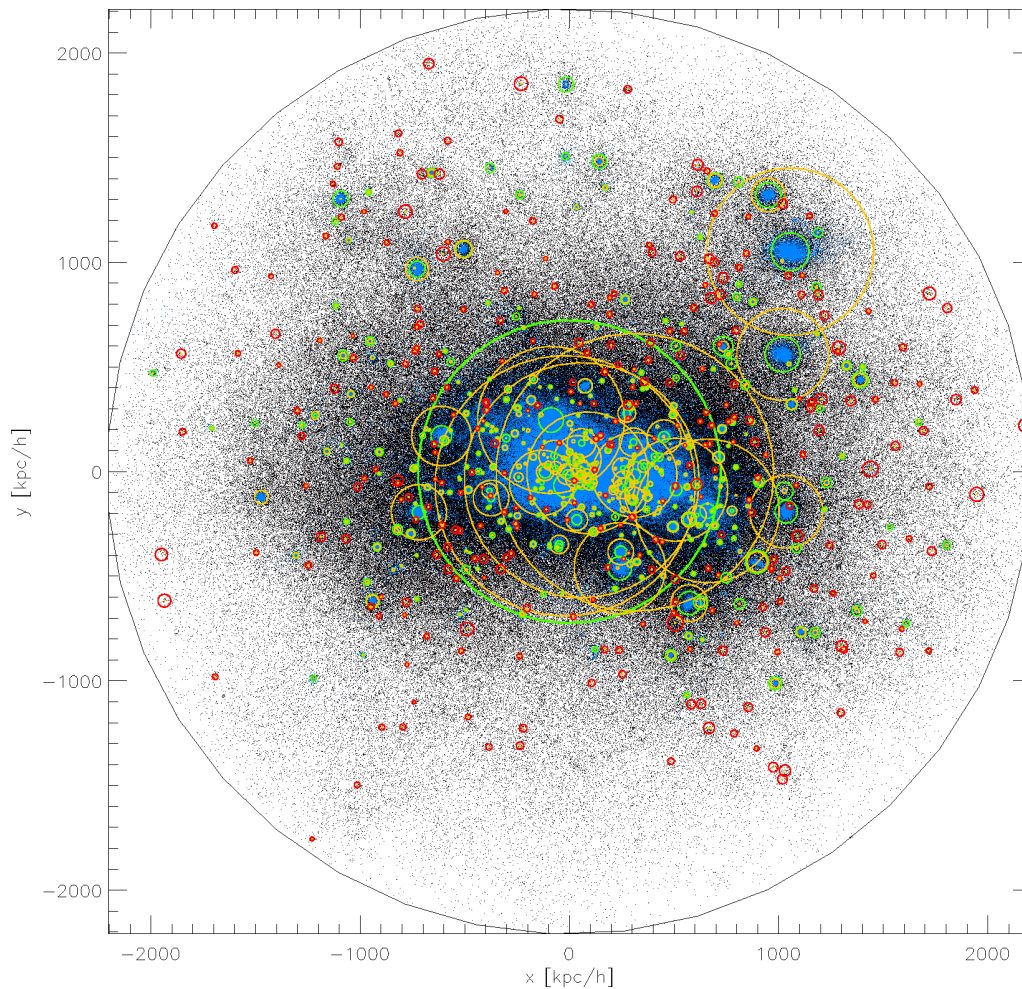
Figure 3.1: Spatial depiction of a $1.2 \cdot 10^{15}\,\mathrm{M_\odot}/h$ galaxy cluster at $z = 0.03$ with 726 subhalos inside the virial radius of $2.2\,\mathrm{Mpc}/h$.

by dividing the total mass of each subhalo by the virial mass of the respective galaxy cluster. This results in a logarithmic frequency plot depicting the relative mass distribution of subhalos within a cluster. Each coloured line in Figure 3.3 represents a different cluster and its distribution.

By contrasting the top and bottom part of the plot, it becomes apparent that the high mass subhalos all are stellar subhalos. Physically, this is obvious because massive subhalos accrete gas which, in turn, triggers star formation and, consequently, yields a stellar subhalo. On the contrary, the low mass end is dominated by dark matter only subhalos. This is also in line with expectations since low mass subhalos do not offer a sufficiently deep potential well to accrete enough gas to allow for star formation to begin.

Both the top and bottom of Figure 3.3 are fitted well by a power law, as indicated by the black line. The cumulative mass function, i.e. a verification of the quality of the simulation, is in fine agreement with observations and other simulations (Dolag et al., 2009). The predicted and observed power law is important since it validates the premises and execution of the simulation. More specifically, it displays that the mass distribution within a complex system, such as a cluster, is in accordance with
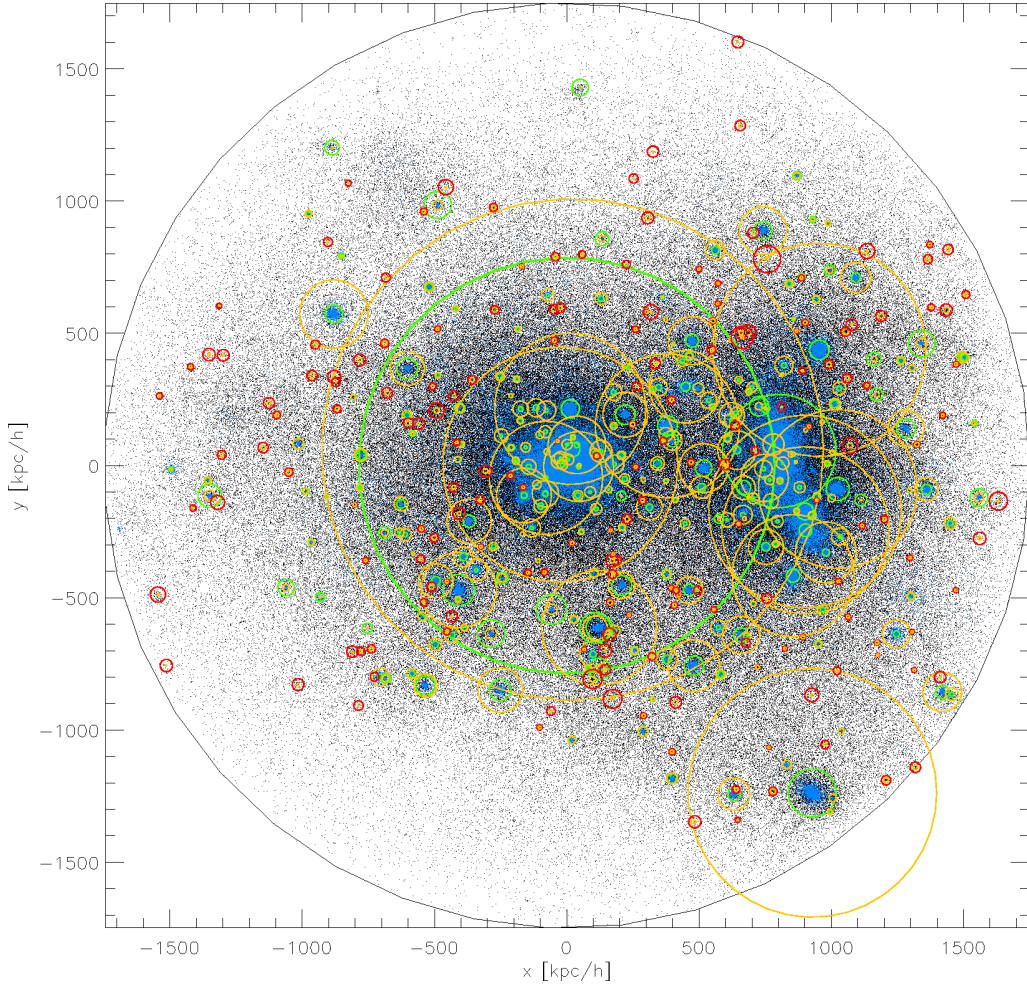
Figure 3.2: Spatial depiction of a $5.8 \cdot 10^{14} \, \mathrm{M_\odot/h}$ galaxy cluster undergoing a merger at $z = 0.03$ with 423 subhalos inside the virial radius of $1.75 \, \mathrm{Mpc/h}$.

observations.

Figure 3.3 also allows insights into the ongoing processes and the history of the individual clusters, represented by the varying coloured lines. Considering the black line, an apparent absence of massive subhalos, compared to other clusters at the higher mass end, can be observed. When inspecting the low mass end of the cluster represented by the black line, a surplus in both panels is evident. This behaviour suggests that the cluster accreted the majority of its mass early on in its formation history. Due to this strong, early accretion it is now located in a depleted environment at redshift zero, where the cumulative mass function is calculated.

This result highlights that subhalos do not accrete significant mass within clusters. The distribution of mass in Figure 3.3 is the consequence of an ex situ subhalo mass growth accreted onto the cluster. The lack of subhalo mass growth after accretion is due to the high velocity dispersion within the cluster, as discussed in section 1.2.5. The only subhalo, which experiences significant growth is the central BCG. Thus, the inspection of the cumulative subhalo mass function enables insights into the formation history and, subsequently, the environment of the cluster.

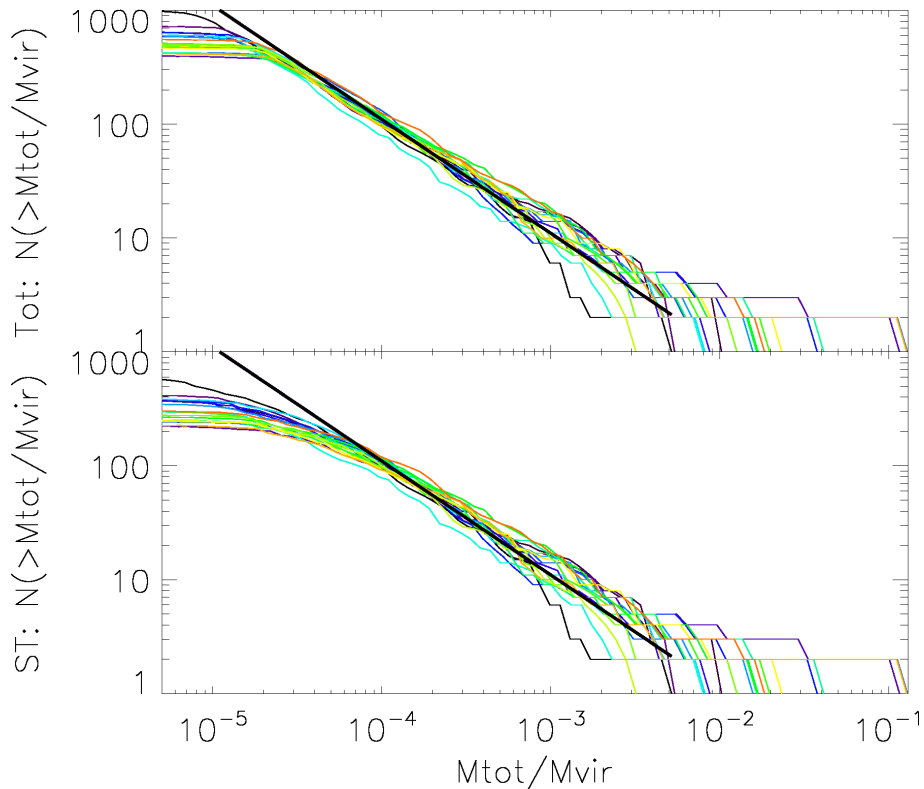Due to the lack of high mass end growth of the cluster, represented by the black

Figure 3.3: Cumulative mass function of both the total subhalo population (top) and
the stellar subhalos (bottom) at redshift zero. Each different colour represents a different
halo. The black line is a power law and is added to show deviations from the expected
distribution.

line, one would expect that its recent history has been one of isolation. To investigate
this, consider Figure 3.4. Similarly to the previous figures, the same colour coding
was used. In comparison to the clusters in Figures 3.1 and 3.2, the cluster in Figure
3.4 is more massive. In fact, it is the most massive cluster in Box2/hr at redshift
zero. In accordance with expectations, it is also far closer to virialisation than its
fellow clusters due to isolation. Hence, Figure 3.4 offers a representation of a well
mixed, isotropic cluster.

   When considering varying clusters in Figure 3.3, one can observe which clusters
experienced fairly consistent mass growth through time. Consistent mass growth
is characterised by a close alignment to the power law. On the other hand, high
mass end frequencies describe more recent accretion onto the cluster, whereas high
frequencies in the low mass end imply early accretion onto the cluster.
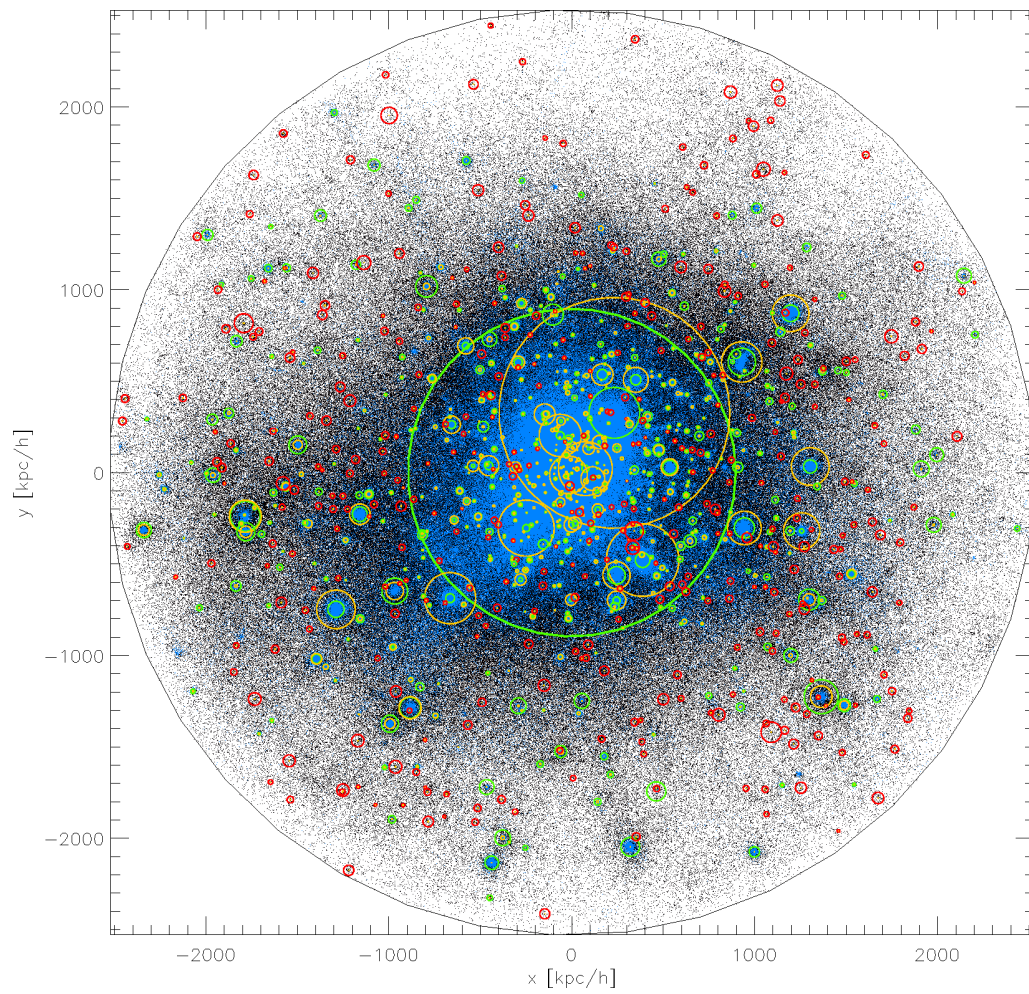
Figure 3.4: Spatial depiction of a $1.76 \cdot 10^{15}\,\mathrm{M_\odot}/h$ relaxed galaxy cluster at $z = 0.03$ with 1008 subhalos inside the virial radius of $2.53\,\mathrm{Mpc}/h$.

Chapter 4

Phase Space

The static considerations of galaxy clusters at redshift zero offer a wide variety of opportunities for the study of clusters. However, to gain meaningful insights into the dynamics of galaxies within their clusters, a more temporal perspective is in order. The aim of this temporal consideration is to uncover the underlying mechanisms governing the evolution of galaxies in clusters. This investigation only becomes possible through the raw potential provided by the Magneticum simulation.

In order to disentangle the effects of varying orbits, the stellar subhalos are subdivided into star forming and non star forming populations. This division is created so as to study the effect of orbits on the star formation of galaxies. Specifically, the two populations are considered in phase space with the goal of determining different characteristics of the subpopulations.

The criterion for star formation is $sSFR \cdot t_H$, i.e. specific star formation rate multiplied by the Hubble time (Franx et al., 2008). As Franx et al. (2008) states, galaxies with a value above 0.3 are considered star forming, while galaxies with $sSFR \cdot t_H < 0.3$ are quiescent. It is now important to emphasise that all non star forming subhalos are quiescent, while not all quiescent subhalos are non star forming, but rather have a low star formation rate.

This 'blueness criterion' ($sSFR \cdot t_H > 0.3$) is important to differentiate between star forming and quiescent galaxies through time. The definition of 'star forming' is now time dependent, rather than merely being applicable to low redshifts. Hence, this definition encompasses the changing star formation history on a cosmological scale and is well suited for a temporal comparison.

4.1   Varying Redshifts

The phase space diagram evolution of twenty stacked clusters from $z = 1.7$ to the present, i.e. $z = 0.03$ is examined. Stacking the clusters allows deductions to be made from a statistically meaningful sample. Before stacking, the clusters are normalised spatially to their virial radius. Thereafter, they are normalised to their virial velocity via their individual virial mass and radius, through the fundamental relation $v_{vir} = \sqrt{\frac{GM_{vir}}{R_{vir}}}$. This process yields a stacked and normalised synthetic cluster comprised of twenty individual clusters. For an extended consideration,
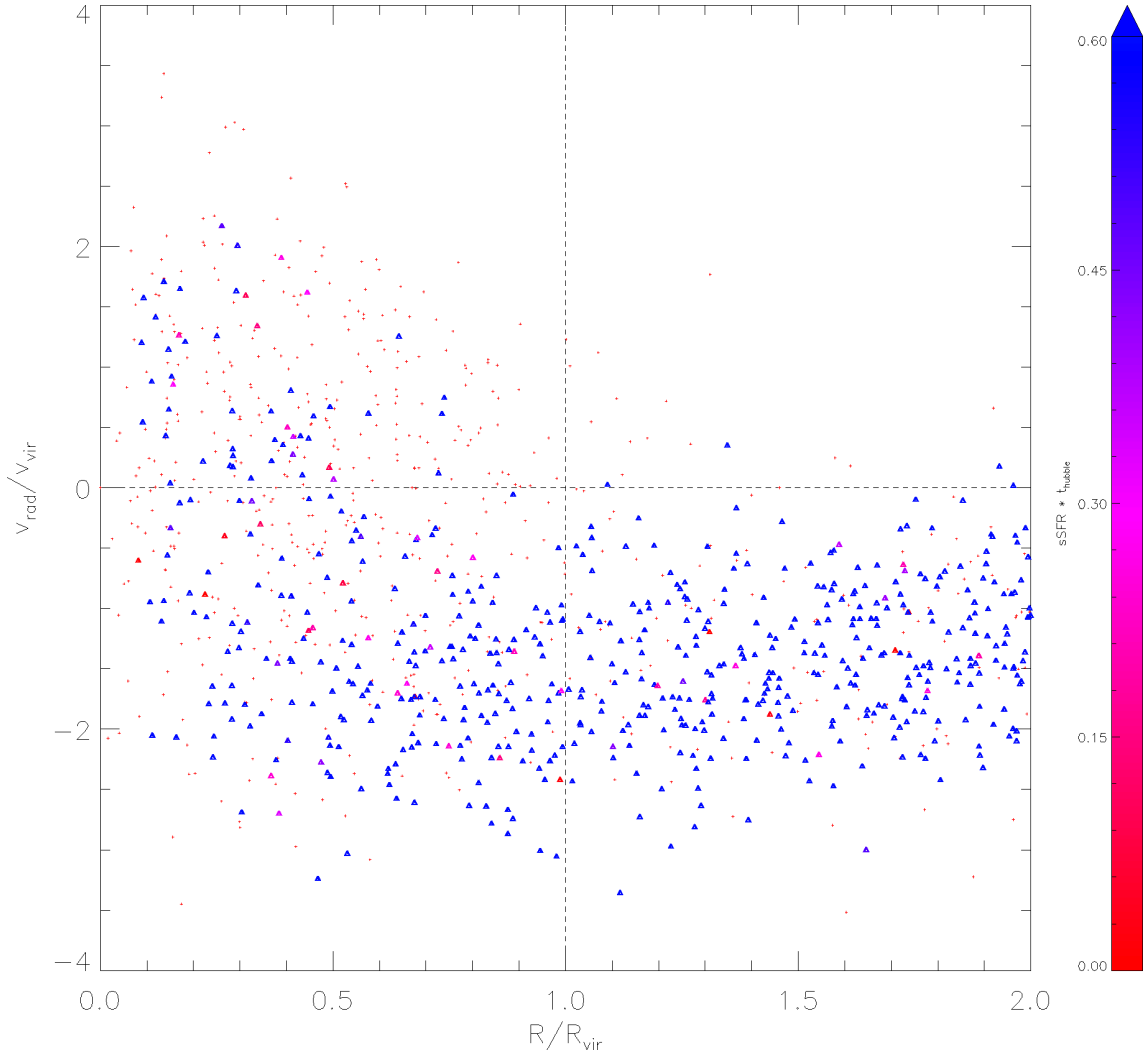
Figure 4.1: Phase space of 20 stacked clusters at $z = 1.7$. The figure shows the normalised velocity, i.e. the radial velocity divided by the virial velocity (v_{rad}/v_{vir}), in dependence of the radius in units of the virial radius, R_{vir}. Any subhalos with a non-zero star formation rate are indicated by triangles, the remaining subhalos are indicated by red crosses. The colour of the triangles represents the degree of blueness, i.e. $sSFR \cdot t_H$.

three representative snapshots are depicted in Figures 4.1, 4.2 and 4.3.

The phase diagram of the stacked cluster at $z = 1.7$ is depicted in Figure 4.1. The zero star forming population is represented by the red crosses, whereas non zero star forming subhalos are indicated by triangles. The degree of star formation is then encoded in the colour of the triangles, according to the introduced criterion. Any purple or blue triangle thus represents a star forming subhalo in the sense of the criterion, with $sSFR \cdot t_H > 0.3$.

A number of interesting observations can be made about Figure 4.1. Firstly, it is evident that a large part of the population, independent of the star formation, is infalling. This can be deduced since the majority of the complete population has a negative radial velocity. Secondly, it can further be seen that the star forming subpopulation is overwhelmingly characterised by a negative virial velocity. Thus,

the star forming population is dominated more by infall than the non star forming subpopulation. Thirdly, the majority of the non star forming population, i.e. the red crosses, appears to be virialised. This is supported by the relative symmetric, even distribution of quiescent subhalos below $1\,R_{vir}$. This suggests that the older population is comprised of quiescent, i.e. red and dead, subhalos, whereas the star forming subhalos are, in cosmological terms, new additions to the cluster.

Lastly, half of the 1140 subhalos located in a $2\,R_{vir}$ radius of the synthetic cluster, i.e. 51%, are made up of quiescent subhalos. The other half, i.e. 49%, are made up of star forming subhalos, as defined by the introduced blueness criterion. It is important to note that not all subhalos within the $2\,R_{vir}$ radius of the gravitational centre of the cluster are bound to the cluster or are destined to collapse onto the structure. The relative abundances of subpopulations gain significance when comparing Figure 4.1 at $z = 1.7$ to other redshifts.
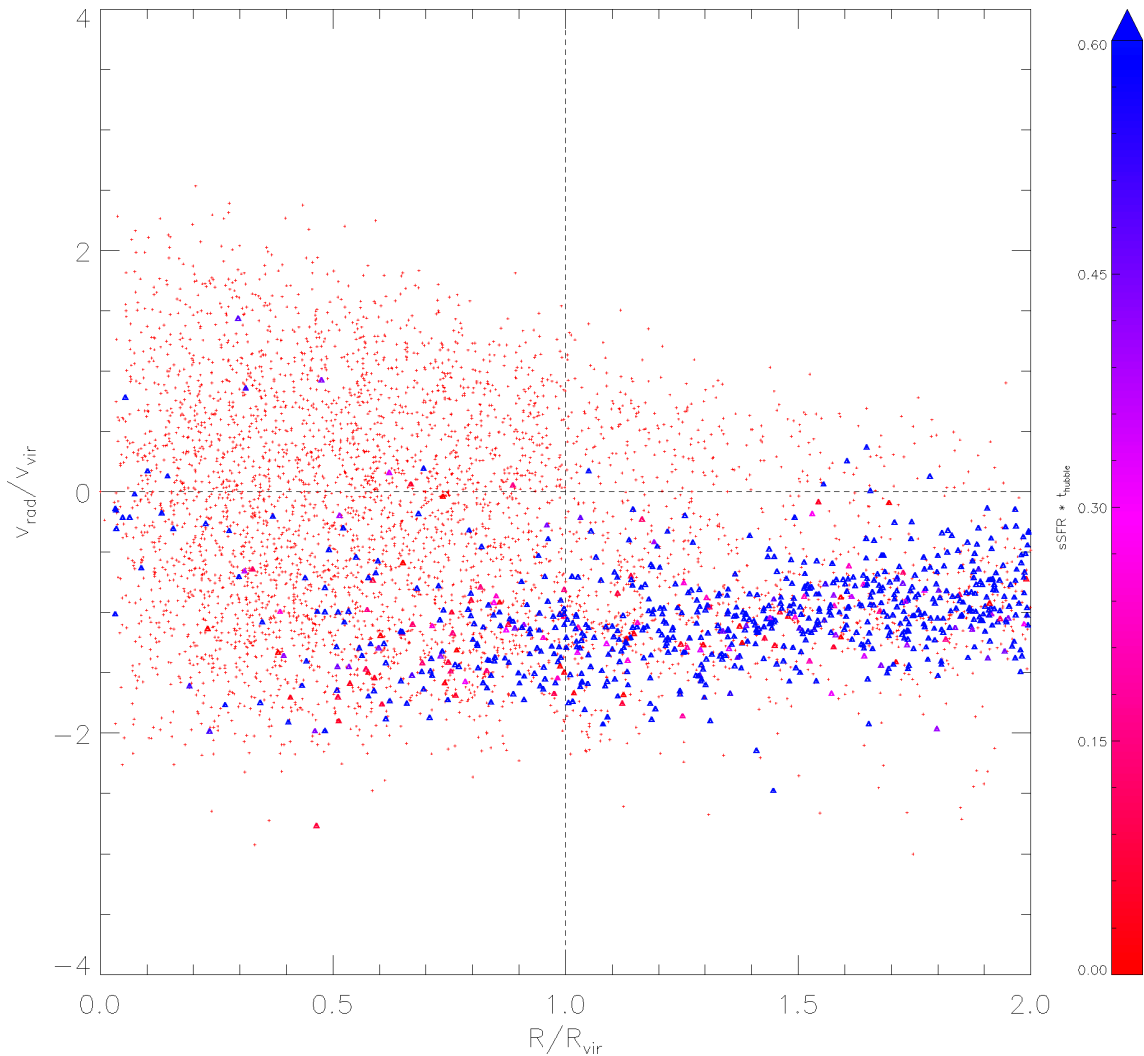

Figure 4.2: Phase space of 20 stacked clusters at $z = 0.44$. The figure shows the normalised velocity, i.e. the radial velocity divided by the virial velocity (v_{rad}/v_{vir}), in dependence of the radius in units of the virial radius, R_{vir}. Any subhalos with a non-zero star formation rate are indicated by triangles, the remaining subhalos are indicated by red crosses. The colour of the triangles represents the degree of blueness, i.e. $sSFR \cdot t_H$.

Figure 4.2 at $z = 0.44$ merely has a star forming population of 13% and hence a quiescent subpopulation of 87% of a total of 5387 subhalos. This strong contrast to Figure 4.1 indicates that the star forming population is strongly quenched and thus adds to the existing quiescent subpopulation. The fact that Figure 4.2 exhibits a star forming subpopulation dominated by infall suggests that the majority of star forming subhalos are quenched during their first passage. This conclusion becomes evident when considering that only 0.3% of all star formers have a positive radial velocity in Figure 4.2.

The star forming subpopulation in Figure 4.2 inhabits a distinct region in phase space which is far more defined than in Figure 4.1. Indeed, subhalos preferentially populate a region between $0.6\text{-}2.0\,\mathrm{R_{vir}}$ and $-0.5\text{-}-1.5\,\mathrm{V_{rad}}$ in phase space. This local overdensity of star formers is the result of an infall dominated population. As theory predicts, the star forming subpopulation increases its normalised velocity with decreasing radius, resulting in the slight positive gradient within the subpopulation.

Theory dictates, that under the assumption of constant cluster mass and constant infall rate of star forming subhalos, the density in a given phase space element decreases towards smaller radii. This is driven by the accelerated radial motion of infalling subhalos. Hence, the subhalo velocity increases with decreasing radius according to $v = \sqrt{\frac{GM_{vir}}{r}}$. Keplerian dynamics predicts that the closer an orbiting object is to its perihelion the faster it is moving. As such, we expect that the density within a constant radial interval decreases towards lower radii. This dynamic is perfectly described by the behaviour exhibited by the star forming subpopulation in Figure 4.2.

The fact that the star forming subhalo density drastically drops at $0.7\,\mathrm{R_{vir}}$ is not predicted by Keplerian dynamics. Rather, it is the result of a strong and fast quenching mechanism transforming star forming into quiescent subhalos. The most realistic candidate for short term violent quenching within clusters is ram-pressure stripping. As discussed in section 1.2.5, ram-pressure stripping removes the cold gas component of galaxies and thus inhibits further star formation.

When comparing Figure 4.1 with 4.2, one can further observe that the average normalised radial velocity decreases towards lower redshifts. Specifically, the subhalos inhabit a smaller area in phase space in Figure 4.2, which is driven by a decreased vertical spread. This is the result of the high redshift sample at $z = 1.7$ having a smaller virial velocity and thus resulting in a wider spread in normalised radial velocities. This, in turn, is driven by a large portion of the mass at $z = 1.7$ not being part of the individual clusters, but rather being in the process of collapsing onto the structure. However, the virial radius density within Magneticum is calculated via a density cutoff and hence the virial radius is likely to be overestimated with regard to collapsing structures. Ultimately, this means that clusters in their early formation process have lower mass at a given virial radius, resulting in a larger normalised radial velocity.

The trends established in previous figures are continued in Figure 4.3 at $z = 0.03$. The star forming subpopulation still inhabits a similar region in phase space. Figure 4.3 depicts 8541 subhalos, 7% of which are star forming and 93% are quiescent. Similarly to Figure 4.2, a tiny percentage, i.e only 0.1%, of star forming subhalos
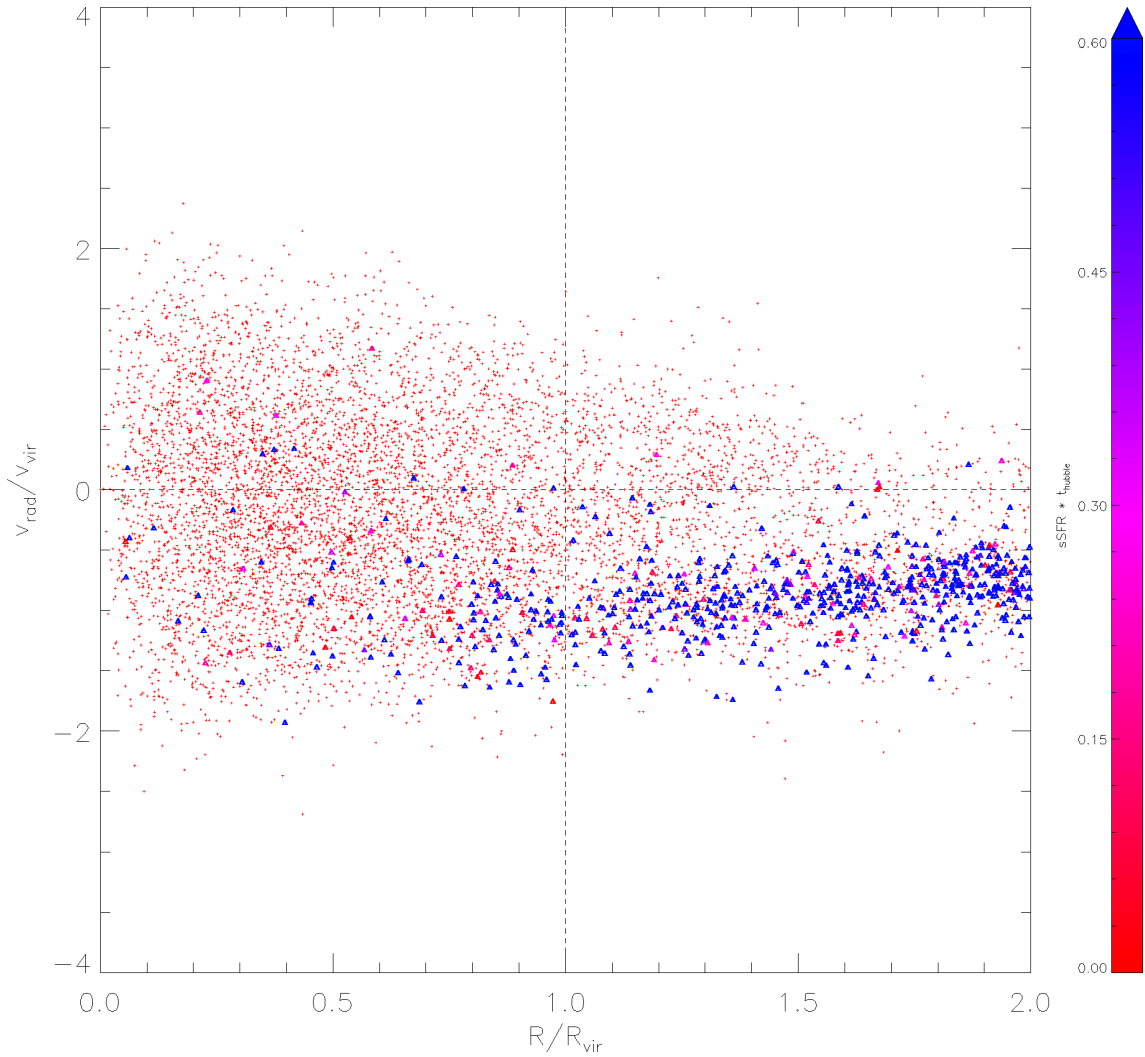
Figure 4.3: Phase space of 20 stacked clusters at $z = 0.03$. The figure shows the normalised velocity, i.e. the radial velocity divided by the virial velocity (v_{rad}/v_{vir}), in dependence of the radius in units of the virial radius, R_{vir}. Any subhalos with a non-zero star formation rate are indicated by triangles, the remaining subhalos are indicated by red crosses. The colour of the triangles represents the degree of blueness, i.e. $sSFR \cdot t_H$.

have a positive radial velocity. In line with previous figures, the majority of subhalos experience quenching at $\sim 0.7\,R_{vir}$, with only a small star forming population at lower radii.

By studying the phase diagrams in dependence of redshift, a number of conclusions present themselves. Globally, through time, clusters grow, beginning with 1140 subhalos at $z = 1.7$ and ending at 8541 subhalos at a redshift of $z = 0.03$ in the synthetic stacked cluster. Hence, as time progresses, more of phase space is populated. Also, despite the clusters' virial mass and radius experiencing significant growth through time, the general shape of the phase diagram remains the same due to the normalisation. The exception to this are high redshift clusters experiencing strong structural collapse. Finally, as redshift decreases, the quenching of star forming subhalos at $\sim 0.7\,R_{vir}$ becomes more efficient.

4.2   Comparison with Observations

To evaluate the validity of the simulations, a comparison with observations is in order. Figure 4.4 depicts a projected phase space diagram with the rest frame velocity plotted against the radial distance in megaparsec at $z = 0.44$ (Biviano et al., 2013). In contrast to the phase space diagrams computed with simulations, Figure 4.4 represents a projection onto the plane perpendicular to the line of sight (los). As such, it is prone to projection errors. The dominant source of error are interlopers, i.e. galaxies erroneously projected into the cluster.

Observers are only able to measure line of sight velocities and are thus limited to one of three spatial degrees of freedom. Consider a star forming galaxy in the outskirts of the cluster $\sim 2\,\mathrm{Mpc}$, which has high perpendicular velocity (to the los) and a low rest frame velocity v_{rf}. As such, it would be located close to $v_{rf} = 0$ in Figure 4.4. Depending on where it lies with regard to the projection, it can be found anywhere below a radial distance $\lesssim 2\,\mathrm{Mpc}$. This issue results in an overestimation of galaxies below a given radial distance. The degree of this overestimation depends on the height of the cylinder in question, i.e. the redshift interval.

The radial velocity in Figure 4.2 is depicted in units of the virial velocity, whereas Figure 4.4 measures the rest frame velocity in km/s. However, this is only of minor concern since a qualitative comparison of phase space behaviour is the goal of this examination. The red line in Figure 4.4 corresponds roughly to the dotted $1\,\mathrm{R_{vir}}$ line in Figure 4.2. To compare the two figures, we focus on the bottom panel in Figure 4.4. With this in mind, a comparison between Figure 4.2 and 4.4 becomes a useful endeavour.

Regarding these points, a number of similarities and differences between Figures 4.2 and 4.4 are apparent. Firstly, the general shape of the phase space diagrams is in agreement. Except for a few outliers in Figure 4.4, likely due to projection effects, as indicated by the selection algorithms (top panel), the overall shape is the same. In contrast to Figure 4.2, the infalling star forming subpopulation in Figure 4.4 is symmetric. This is the result of considering v_{rf} (los) rather than v_{rad}. The rest frame velocity in phase space is expected to be symmetrically distributed since, statistically speaking, clusters are isotropic. This means that infalling subpopulations cannot be distinguished in Figure 4.4.

Secondly, the quenching in the inner regions of the cluster in Figure 4.4 is also visible. A decrease in star forming population around $R \sim 2\,\mathrm{Mpc}$ can be observed, which is in qualitative agreement with Figure 4.2. However, the radius at which quenching decreases the star forming population sharply, is larger in Figure 4.4. This is not surprising since the sole cluster observed in Biviano et al. (2013) is more massive than 19 out of the 20 simulated counterparts at the same redshift (compare section 2.1 with Table 3.2).

A more massive cluster is expected to have more effective quenching at a given radius. In other words, at the same radius in units of the virial radius a more massive cluster is more effective in quenching. This is due to higher mass clusters having higher temperatures at the same radius in units scaled to the virial radius than lower mass clusters at the same radius in units of the virial radius, i.e. at $1\,\mathrm{R_{vir}}$ for each respective cluster. Higher temperatures result in more effective quenching
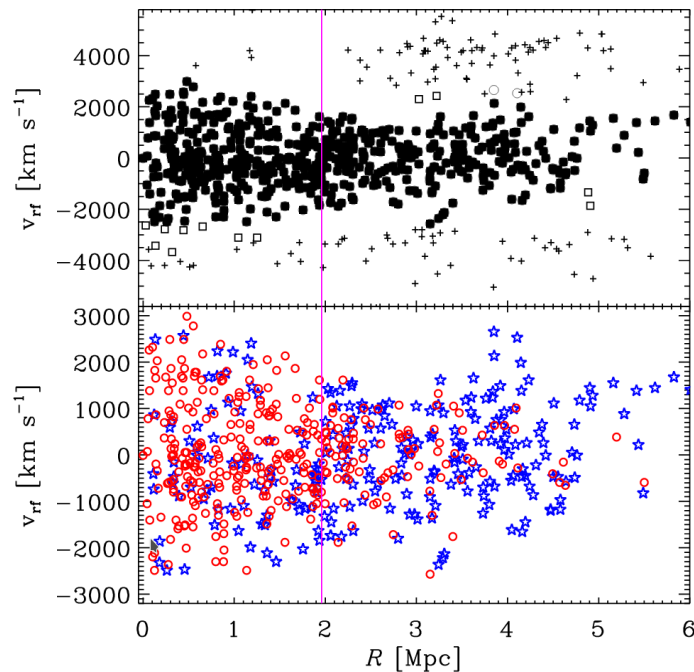
Figure 4.4: *Top panel:* galaxies in the projected phase space diagram, R, v_{rf}. Black dots represent galaxies identified as cluster members by both the P+G and Clean algorithms. Open circles represent galaxies identified as cluster members by P+G algorithm only. Squares represent galaxies identified as cluster members by the Clean algorithm only. Crosses represent non cluster members. *Bottom panel:* cluster members selected with the P+G method in the projected phase-space diagram, R,v_{rf}. Red circles represent passive galaxies, blue stars represent SF galaxies. In both panels the vertical (magenta) line indicates $r_{200,U}$, i.e. the r_{200} value obtained by scaling the r_Δ estimate of Umetsu et al. (2012) at $\Delta = 200$, using their best- fit NFW profile. Figure from Biviano et al. (2013).

by impeding gas cooling and hence star formation.

Thirdly, a relative overabundance of star formers can be observed in the outskirts of the cluster in Figure 4.4. Comparisons can only be made up to $R \sim 4\,\mathrm{Mpc}$, since this is the maximum corresponding radius available in Figure 4.2. When comparing to simulations, a different relative distribution in subpopulations can be seen between a radius of $R \sim 2\,\mathrm{Mpc}$ and $R \sim 4\,\mathrm{Mpc}$. In Figure 4.2, 503 star forming subhalos are located between 1-2 $\mathrm{R_{vir}}$, while 1207 quiescent subhalos occupy the same radial interval. In contrast, in Figure 4.4 the majority of galaxies in the corresponding 2-4 Mpc interval are star formers. Currently, this comparison is between 20 simulated and one observed cluster. As such, the lack of further observations hinders a statistically meaningful conclusion about the origins of this distribution. However, it is likely that many quiescent, in the sense of the blueness criterion, less massive galaxies $\sim 10^{11} \mathrm{M_\odot}$ are simulated while in observations they lie under the detection limit.

Nonetheless, this limited comparison already yields meaningful insights. The observations provide further evidence that the star forming population is dominated by infall. Furthermore, both figures show that the star forming population undergoes a strong, short time span quenching mechanism as it enters the cluster. To evaluate

a wider variety of redshifts refer to Figures 8.1, 8.2, 8.3, 8.4 and 8.5 located in the appendix.

4.3   Convolution of Varying Redshifts

In order to truly decipher the global time independent trends in the phase space diagram the 100 snapshots ranging from $z = 1.7$ to $z = 0.03$ are merged into one image. This process allows the identification of distinct regions and behaviours independent of redshift. The highest redshifts were weighted least, i.e. plotted first, with the most significance given to low redshifts. The result is depicted in Figure 4.5 and follows the same convention as previous plots with regard to the colouring.

It is important to recognise that the non zero star forming subhalos, i.e. the triangles in Figure 4.5 are favoured over the zero star formation subhalos, i.e. the red crosses. The triangles are plotted at a significantly larger size to allow clearer visualisation of the development in star formation rate. The favourable visualisation of triangles allows a depiction of the star formation rate evolution through phase space. Under equal treatment the effects clearly visible in Figure 4.5 become indistinct, impeding valuable deductions due to the overwhelming non star forming population.

The most visible phase space trend is the clear distinct star forming region previously identified in Figure 4.2. Due to the large statistical sample depicted in Figure 4.5, the regions identification is facilitated. In addition, the previously identified trend, namely the over density of star formers in the region encompassed by 0.5 - $2.0 \, R_{vir}$ and -1 - $2 \, V_{rad}$, becomes explicitly clear. The star forming region remains characterised by a sharp cut-off at low radii and a widening with regard to the normalised radial velocity towards higher radii.

Another distinct subpopulation attracts attention when inspecting Figure 4.5 closely. The population is characterised by orbits with $r > 1 \, R_{vir}$ and small radial velocities $\sim 0 \, V_{rad}$. This subpopulation appears to be symmetric and can be differentiated, in the case of slightly negative radial velocities, from the bulk of infalling subhalos. Under further inspection, this population is comprised of both quiescent and star formering subhalos. These subhalos appear to be on relatively circular orbits, allowing a small star forming component to remain active despite being bound to the cluster. This is due to the fact that the comparatively slow and circular orbits do not experience the strongly quenching environment at lower radii.

All these considerations point to the dominant quenching effect to being ram-pressure stripping. The effect is highly correlated to the radial distance, excluding longer lasting, continuous mechanisms like strangulation. In addition, slower, circular populations exhibit a comparatively large star forming subpopulation, indicating that the effect is dependent on orbital type and velocity. The rapid nature of the quenching mechanisms, i.e. the fact that the vast majority of subhalos do not remain star forming during their first passage, excludes mechanisms that solely deprive the subhalos of their outer gas halos. Mechanisms like these, such as strangulation, would present a less radially truncated quenching effect and happen on larger time scales than the observed mechanism.
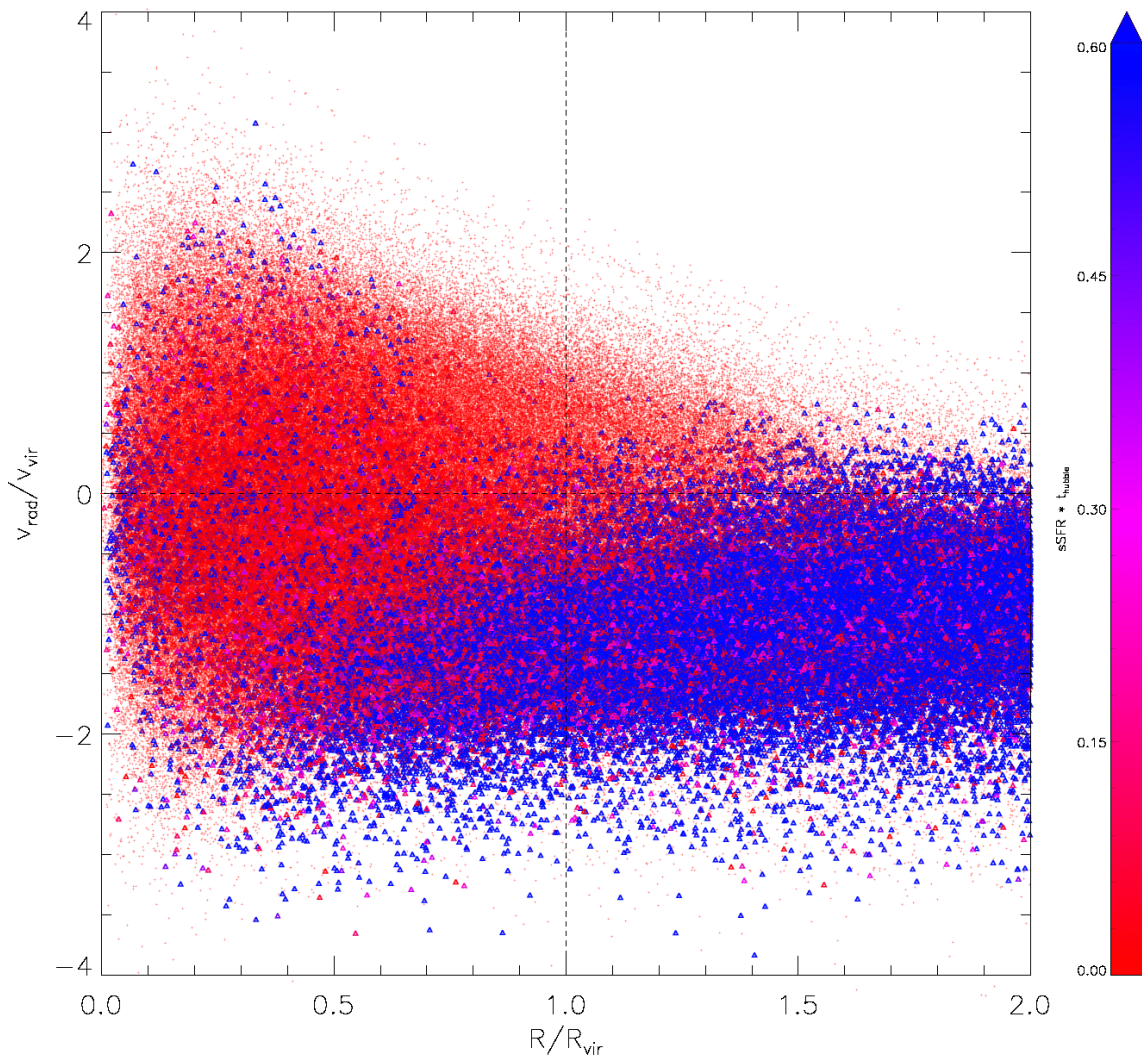
Figure 4.5: Overlay of phase space diagrams of 20 stacked clusters from $z = 1.7$ to $z = 0.03$. The figure shows the normalised velocity, i.e. the radial velocity divided by the virial velocity (v_{rad}/v_{vir}), in dependence of the radius in units of the virial radius, R_{vir}. Any subhalos with a non-zero star formation rate are indicated by triangles, the remaining subhalos are indicated by red crosses. The colour of the triangles represents the degree of blueness, i.e. $sSFR \cdot t_H$.

4.4   Analysing Histograms

An interesting opportunity arises when considering radially binned velocity histograms of the star forming and quiescent subpopulation at high and low redshifts. Figures 4.6 and 4.7 provide insights into the evolution of the subpopulations' tangential and radial components. As with the phase space investigation, the histograms are calculated from the first 20 clusters at a given redshift. Each histogram represents a $0.2\,R_{vir}$ interval, meaning that the histograms range from the centre of the cluster over five intervals to the virial radius $1\,R_{vir}$.

   The figures are normalised so that the integral of each historgram's subpopulation

is equal to one. The star formers are indicated by the blue lines, while quiescent subhalos, according to the introduced blueness criterion, are coloured red. The black line depicts the histogram of the total population, which is often overplotted by the red line when quiescent subhalos dominate the total population. The top panel shows the normalised, with respect to the virial velocity, tangential component, which ranges from 0 to 4 in units of normalised velocity. In contrast, the bottom panel displays histograms of the radial velocity ranging from -4 to 4 in units of normalised velocity, i.e. $v_{tang,rad}/v_{vir}$.

The different ranges are the result of the different component characteristics. The tangential component is calculated from its two components $v_{tang} = \sqrt{(v_\theta)^2 + (v_\phi)^2}$ and hence is always positive. On the contrary, the radial component can assume both positive and negative values, with negative velocities corresponding to infalling motion. Due to the effect of constant bin sizes combined with different velocity ranges of the two components, the resolution in both cases is different.
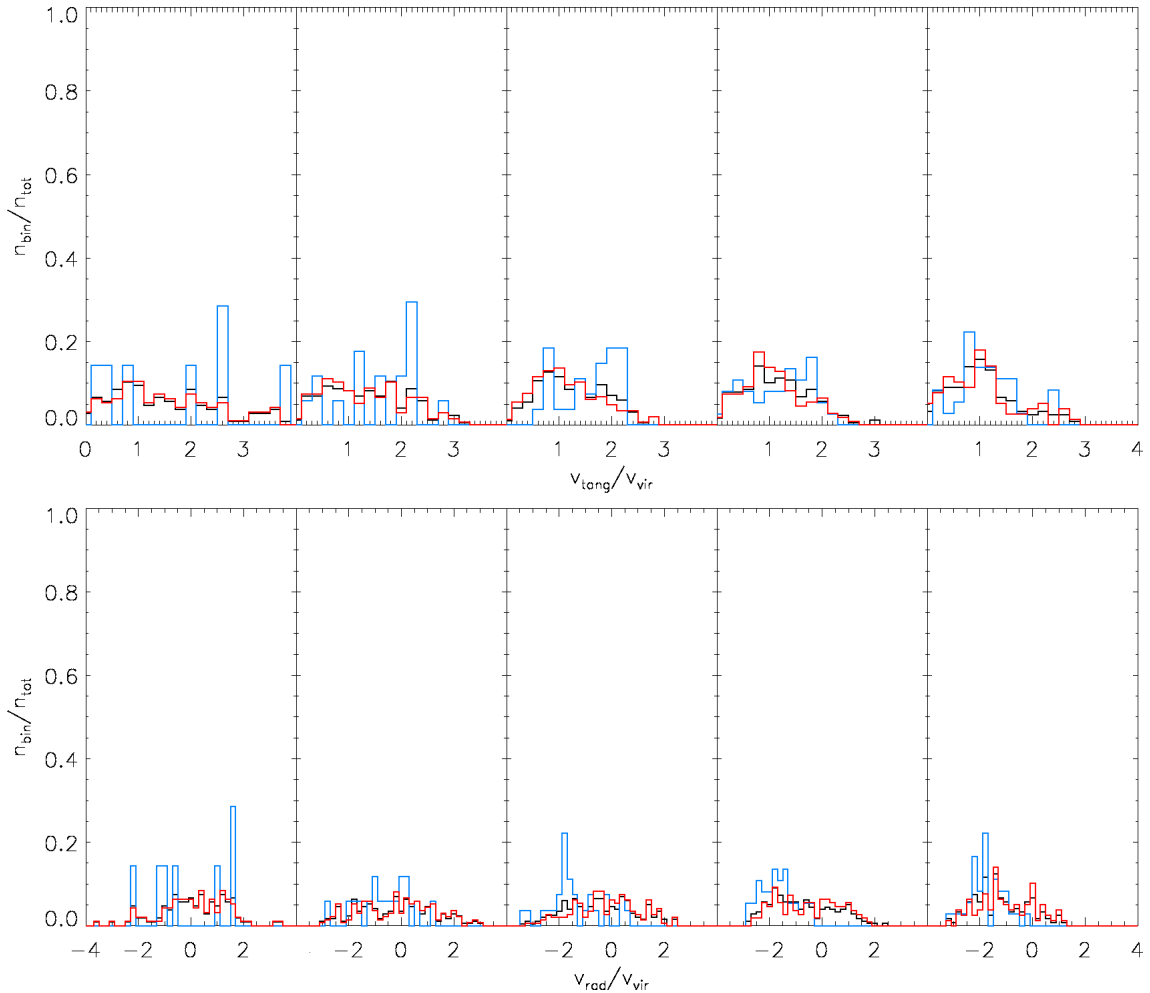

Figure 4.6: Histograms of the velocity distribution of five different radial bins each 0.2 virial radii wide from $0\,R_{vir}$ to $1\,R_{vir}$ at z = 1.7. At the top the tangential component is depicted and at the bottom the radial component is shown. The colours indicate SF (blue), quiescent (red) galaxies and the black line represents the total population

Considering the high redshift case in Figure 4.6, a number of conclusions can be

drawn. Firstly, the sample, compared to lower redshifts, is far smaller and thus the statistics suffer. In comparison to lower redshifts, one can see that star forming and quiescent subhalos behave relatively similarly, broadly speaking. A lack of both a global, i.e. subpopulation independent, and distinct, i.e. subpopulation dependent, radial trend is apparent. This implies that there is not sufficient evidence for an orbital selection effect with regard to the two subhalo populations at high redshift. The only visible distinction is within the radial component, namely that the star forming subhalos are more infall dominated than quiescent subhalos above $\geq 0.4\,\mathrm{R_{vir}}$.

Figure 4.7 depicts a drastically different distribution. In contrast to the high redshift case, Figure 4.7 at $z = 0.03$ exhibits a clear radial dependence in its components. The strongest such trend is visible in the tangential component of the quiescent subpopulation. At larger radii there is effectively less kinetic energy in the tangential degree of freedom. The lower the radii, the larger the high speed tail of the individual distribution becomes, i.e. statistically more subhalos have higher tangential velocities at lower radii. As such, the histograms provide insights into the amount of kinetic energy within different radial shells.

A flattening of the radial component of the quiescent subpopulation is visible in the bottom panel. Specifically, more quiescent subhalos have higher radial velocities (both in- and outwards) at lower radii. Assuming a closed orbit, this is simply the result of Keplerian motion, i.e. the closer to the perihelion, the faster an object moves. In addition to this, subhalos likely transfer some of their radial energy, originating from the initial collapse onto the cluster, to tangential degrees of freedom. This happens through the process of dynamic friction, whereby galaxies interact gravitationally over large distances resulting in orbital alterations, distributing energy through the principle of equipartition to all available degrees of freedom.

In the bottom panel of Figure 4.7, one can observe that, at all radii, the star forming subpopulation is dominated by infall. In accordance with the phase space findings, almost no star forming subhalos at $z = 0.03$ have a positive radial velocity. This implies, similarly to the phase space analysis, that star forming subhalos do not survive their first passage but rather are quenched prior to reaching their perihelion.

By regarding Figures 4.6 and 4.7, the temporal evolution within clusters becomes visible. The nebulous nature of the high redshift histograms illustrates the unrelaxed dynamics at $z = 1.7$. Almost no apparent pattern can be distinguished in Figure 4.6. This is the result of the high redshift clusters under consideration still being in their infancy and, hence, not having had sufficient time to undergo much relaxation. In contrast, clusters in Figure 4.7 have had $\sim 10\,\mathrm{Gyrs}$ more time to assemble and relax. The contrast between $z = 1.7$ and $z = 0.03$ thus highlights the effect temporal evolution has on the ordering of clusters. Effectively, we observe the evolution from chaos to structure, governed by the principles of gravitational dynamics.
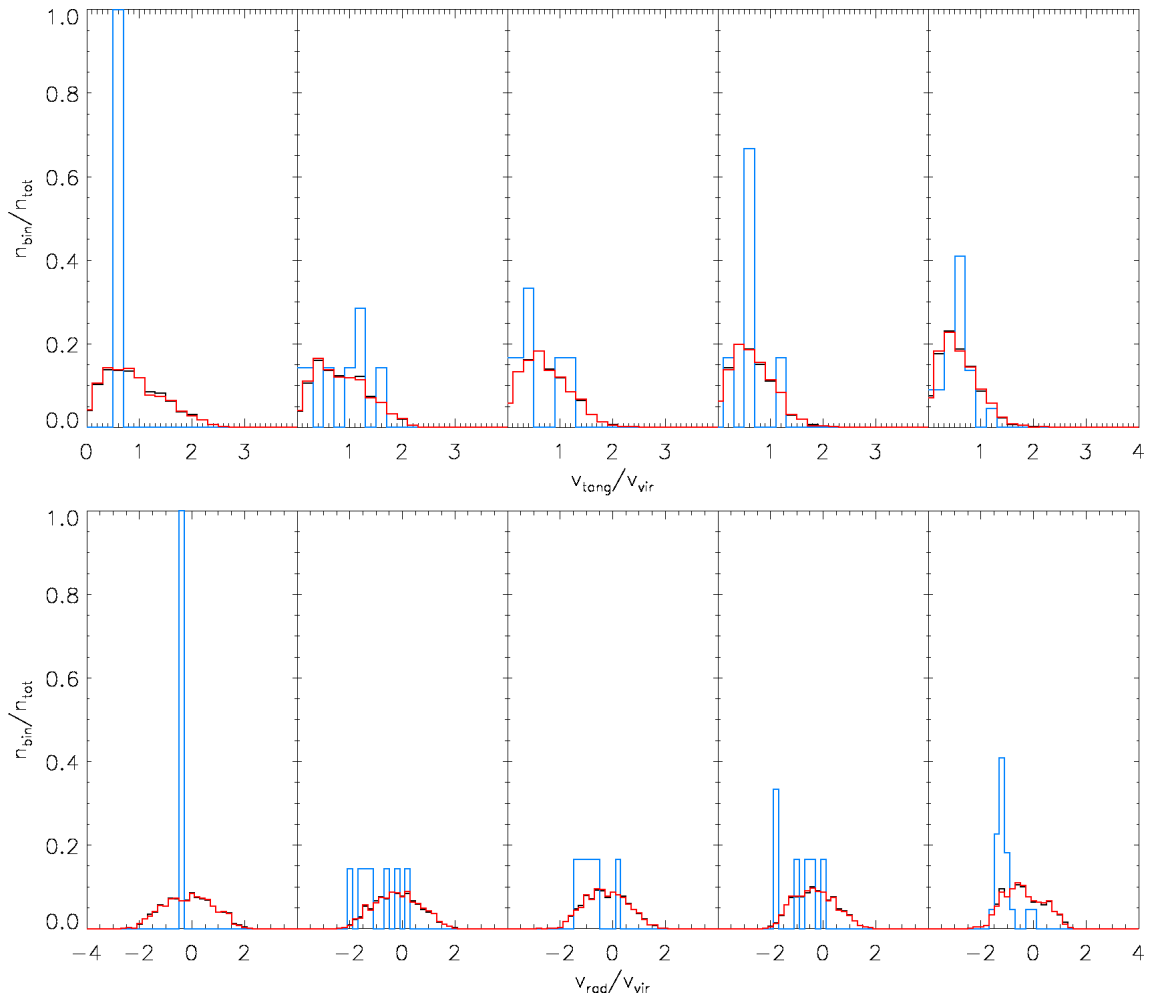
Figure 4.7: Histograms of five different radial bins each 0.2 virial radii wide from $0\,\mathrm{R_{vir}}$ to $1\,\mathrm{R_{vir}}$ at $z = 0.03$. At the top the tangential component is depicted and at the bottom the radial component is shown. The colours indicate SF (blue), quiescent (red) galaxies and the black line represents the total population

Chapter 5

Blueness Evolution

A more detailed and especially individual subhalo study is required in order to truly link orbital characteristics to quantities like the blueness. The blueness, i.e. the specific star formation rate multiplied by the Hubble time, is traced together with the radial distance of subhalos and investigated over time. The goal behind this investigation is to better understand the degree of correlation between blueness and radial distance. In addition, tracking individual orbits allows a more intimate insight into the behaviour of subhalos in clusters. It therefore also offers an inspection and utilisation of the potential of the Magneticum simulation.

5.1 Chasing Subhalos

In Figure 5.1 the temporal evolution of 15 subhalos in a representative cluster (Halo ID = 002 at $z = 0.54$), with regard to their radial distance and their blueness, is shown. The temporal evolution spans $\sim 5\,\mathrm{Gyr}$ in a range from $z = 0.54$ to $z = 0.03$. The subhalos displayed in Figure 5.1 were selected according to their blueness and their radial distance. Specifically, the criterion selected subhalos at $z = 0.54$ in a radial distance range of 1.5-3.5 $\mathrm{R_{vir}}$ and with a blueness of $sSFR \cdot t_H > 0.3$. In other words, distant infalling star forming subhalos were selected to study their evolution as they fall into the cluster. To allow for easier differentiation and identification, only 15 representative subhalos are plotted.

Irrespective of the initial orbit, all subhalos are quenched within the $\sim 5\,\mathrm{Gyr}$ time span. Interestingly, the subhalos also experience strong variations in their blueness, while falling into the cluster. These star bursts are likely triggered through the environment in the outskirts of the cluster. When passing through shock fronts in the outskirts of the cluster $> 1\,\mathrm{R_{vir}}$, gas is compressed and star formation is triggered throughout the subhalo. This is the likely origin of the behaviour visible in the bottom panel of Figure 5.1.

The process triggers short star bursts and gradually depletes the gas supply, effectively strangulating the subhalo. This effect is compounded by passing below the virial radius and the additional exposure to ram-pressure stripping. Understanding the relative impact of strangulation and ram-pressure stripping is the goal of the detailed inspection in section 5.2. Figure 5.1 suggests that shocks trigger star bursts and the environment gradually strangulates the subhalos, resulting in a long term

decrease in star formation. However, the gradual decrease in blueness is truncated by the temporally short scaled and violent ram-pressure stripping, once the subhalos pass below the virial radius.

The majority of subhalos are quenched relatively early, $z > 0.35$. Once quenched, all but one (yellow) of the subhalos remain quenched. However, the yellow subhalo at the time of its last star burst, has not passed below the virial radius of the cluster. Once its radial distance decreases further, it, too, remains quenched. A possible candidate for the underlying mechanism of this star burst is, as previously, a shock front inherent to the cluster environment. Shock fronts are distributed throughout the cluster. According to cosmological simulations by Zinger et al. (2016b) the outer accretion shock extends as far out as (2-3) R_{vir}.

In line with the conservation of angular momentum, none of the subhalos reach the centre of the cluster. Dependent on the individual subhalo, the radius at the first perihelion ranges from 0.2-0.7 R_{vir}. Furthermore, the effects of dynamical friction can be seen in the decrease of the radii of consecutive perihelions.

An initially perplexing anomaly presents itself at $z = 4.95$. All orbits in the top panel in Figure 5.1 experience a shift in their radial distance. This 'bump' is the result of a cluster merger similar to the one displayed in Figure 3.2, albeit at a much higher redshift. The merger results in a shifting of the cluster's centre of mass. This, in turn, results in an offset in the radial distances calculated for the specific time step. Once the merger is complete and the cluster centre is located at the centre of the global potential again, the anomaly vanishes.

5.2   Investigating Quenching

To enable statistically meaningful deductions, the data sample consisting of the discussed 20 clusters is used. Compared to the phase space investigation, the clusters are not stacked, but rather considered independently. In contrast to section 5.1, almost all subhalos within the selection criterion are now used, rather than a small subsample. Despite this leading to crowding within the plot, it also allows the identification of correlations due to a larger statistical sample.

During the investigation of the quenching mechanisms, two important distinctions need to be made with regard to changes in the visualisation. Firstly, the time scale was converted from redshift to gigayears. This was driven by the necessity for a linear time scale, so as to permit equal time interval comparisons. Secondly, to facilitate the visualisation of a correlation between radial distance and blueness, all subhalo orbits were rescaled to the time at which they passed through the virial radius. This means that the time axis is shifted, so that all subhalos pass through the virial radius at the same point on the time axis. This leads to a de facto extension of the time axis past 0 Gyr, leading to negative values.

The result of these two changes are shown for a representative cluster in Figure 5.2. Due to issues with merger trees, discussed in section 7.3, only the least effected cluster is depicted. Hence, Figure 5.2 is the prime example of the 20 different clusters investigated and will be discussed in detail. It contains 121 subhalos that fit the selection criterion, all of which are displayed. Over the time span of ~ 5 Gyr, not
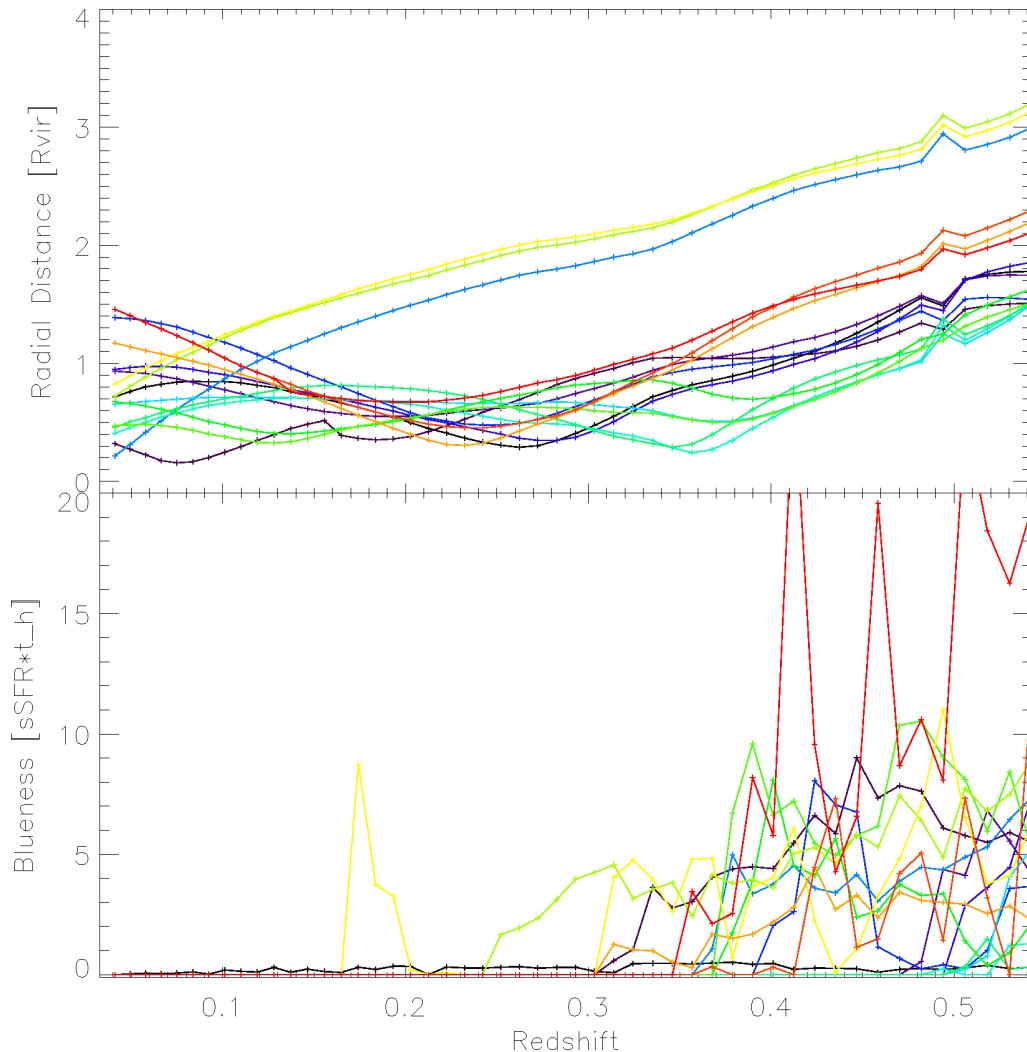
Figure 5.1: Temporal evolution of 15 subhalos with regard to their radial distance and blueness. Each line represents an individual subhalo tracked through redshift. Top panel: radial distance to the centre of the cluster in dependence of redshift. Bottom panel: blueness, i.e. specific star formation rate multiplied by the Hubble time, dependent on redshift.

all subhalos fall below the virial radius. Subhalos that do not pass below the virial radius are not scaled but remain unchanged.

Figure 5.2 is the most compelling argument for ram-pressure stripping being the dominant quenching mechanism in clusters. A strong correlation between ~ 0.5-$1\,R_{\mathrm{vir}}$ and the extreme drop in star formation rate is observed. Shortly after passing below the virial radius, all but three subhalos are completely quenched. In other words, 98% of subhalos are quenched within the first gigayear of passing below the virial radius.

Following further investigation, it becomes clear that one of the three subhalos (orange) has an uncharacteristically shallow orbit. The orange subhalo can be identified in the top panel of Figure 5.2. Its radial distance never drops below $\sim 0.8\,R_{\mathrm{vir}}$. As a result, it likely doesn't experience ram-pressure stripping as violently. As

a direct consequence, its dominant quenching mechanism is strangulation, which manifests itself as a gradual decrease in blueness in the bottom panel.

The other two subhalos that are not quenched are likely to be massive and/or on circular, slowly decaying orbits. However, this is still under investigation. Interestingly, a fourth subhalo (red) at $\sim -2\,\mathrm{Gyr}$ experiences a star burst after being completely quenched. The subhalo is likely undergoing a merger, which triggers star formation. Although some individual subhalos are still under investigation, the vast majority of subhalo behaviour can be explained with violent ram-pressure stripping and gradual strangulation.
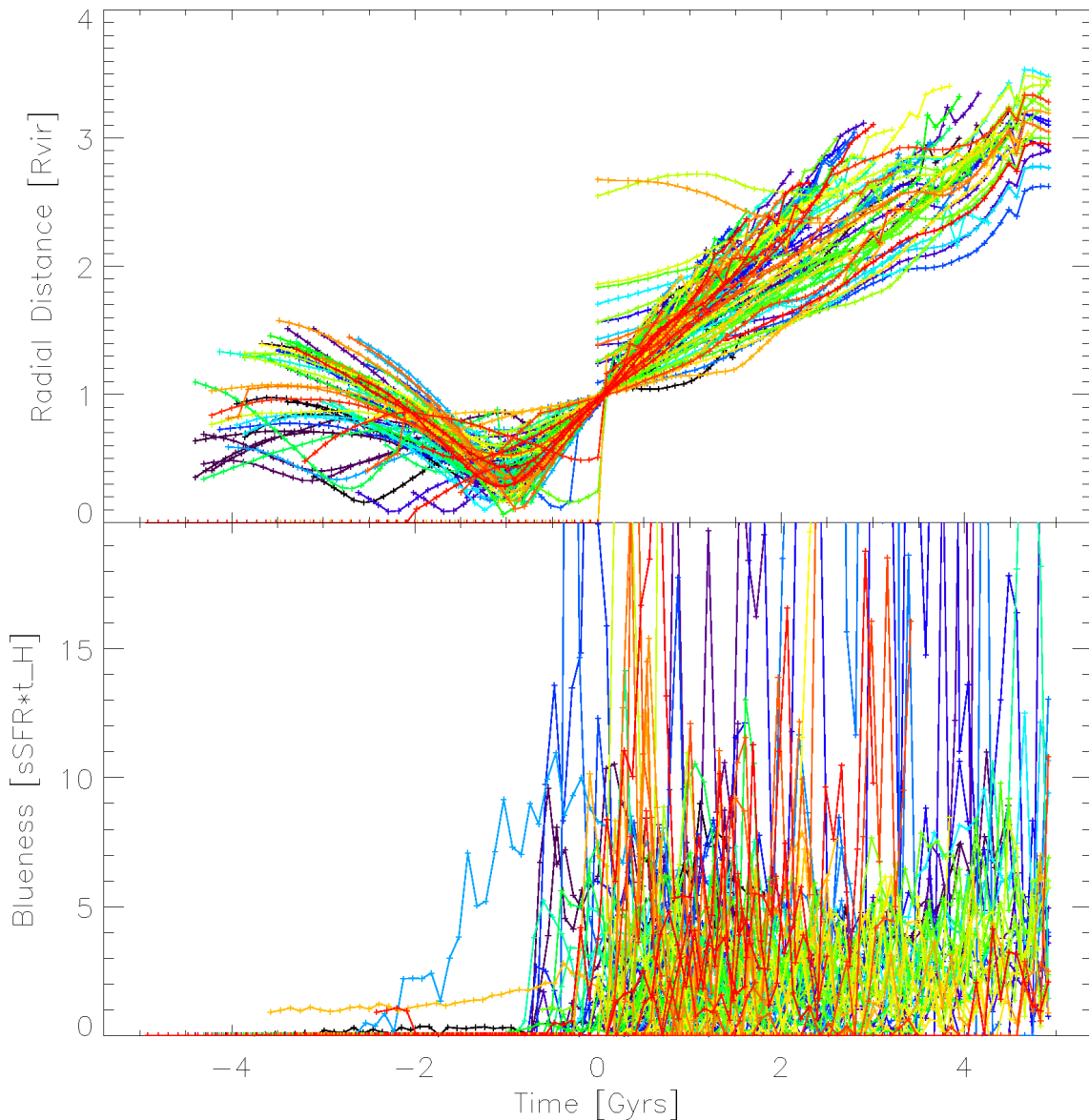

Figure 5.2: Scaled temporal evolution of 121 subhalos with regard to their radial distance and blueness. Each line represents an individual subhalo tracked through time. The trajectories of the subhalos are shifted to the point where they pass below $1\,\mathrm{R_{vir}}$. Top panel: radial distance to the centre of the cluster in dependence of time. Bottom panel: blueness, i.e. specific star formation rate multiplied by the Hubble time, dependent on time.

In contrast to Figure 4.5, it is not possible to observe an actual increase in star formation in Figure 5.2 before being quenched. Although an increase is observed, it is not clear whether this is due to an increase in star formation or rather an increase in subhalos within a scaled time interval. In other words, the observed increase can not definitively be accredited to star formation, but could also be caused by more subhalos due to scaling.

To truly disentangle star bursts from an increase in subhalo population due to scaling, a greater time span is needed. With a longer time span, the areas of inconstant population could be truncated. This would lead to a constant number of subhalos within a given time interval, allowing for an actual comparison. However, currently the merger trees at higher redshifts do not behave as anticipated. This leads to mismatching and hinders tracking. As a result, subhalos are currently only tracked from $z = 0.54$ to $z = 0.03$.

This time span is sufficient to evaluate the short term, radially strongly dependent effect of ram-pressure stripping. However, it does not suffice for a spatially less distinct correlation, like the ones exhibited by star bursts and strangulation, at least not while tracking individual subhalos, as is the case in this section. In contrast, in section 4 redshifts up to $z = 1.7$ are evaluated since individual subhalo tracking is not utilised.

Smaller issues with merger tree mismatching are also visible in Figure 5.2. Jumps in the radial distance can be identified, for example, close to $\sim 1\,R_{\mathrm{vir}}$. These jumps exhibited by four subhalos do not reflect a physical process, but rather are the result of mismatching. Nevertheless, the percentage of the population presenting this behaviour is negligible. Hence, it does not impact the results in meaningful way as long as the tracking is limited to redshifts below $z = 0.54$.

Chapter 6

Anisotropy Parameter

6.1 Stacking Clusters

As discussed in section 1.3, the velocity anisotropy parameter is a quantity used to measure directional dependence. Within the scope of this work it is used to measure the relative importance of tangential and radial degrees of freedom with respect to galaxies in a cluster. The goal of an anisotropy consideration is to understand the mechanisms governing the radial profiles of different subpopulations. Examining the velocity anisotropy allows a more detailed, quantitative approach.

The same stacked synthetic cluster at $z = 0.03$ is used and further reduced by considering dispersions in radial and tangential direction. For this process to be effective the Cartesian coordinate system is transformed into spherical coordinates. This allows the comparison of the radial component with the two tangential components. To calculate a meaningful anisotropy parameter, the radial profile is binned into equal distance cumulative bins.

6.2 Competing Mean Methods

A number of important details also need to highlighted. Firstly, when calculating dispersions σ the corrected sample standard deviation is used:

$$\sigma = \sqrt{\frac{1}{N-1} \sum_{i=1}^{N} (x_i - \overline{x})^2},$$

where N denotes the size of the sample, x_i represents the observed values of the sample and $\overline{x}$ is the mean value of the observations. When calculating the anisotropy parameter the mean is set to zero, $\overline{x} = 0$. This is done because an isotropic distribution of subhalos is assumed. Furthermore, to be able to compare different subpopulations and their respective anisotropy parameter β, the mean needs to be the same, independent of the subpopulation.

An example of the impact of the two different mean calculation methods at $z = 0$ is shown in Figure 6.1. Due to the infalling star forming subhalo population being on radially dominated orbits, the mean is also radially dominated. Translated to the
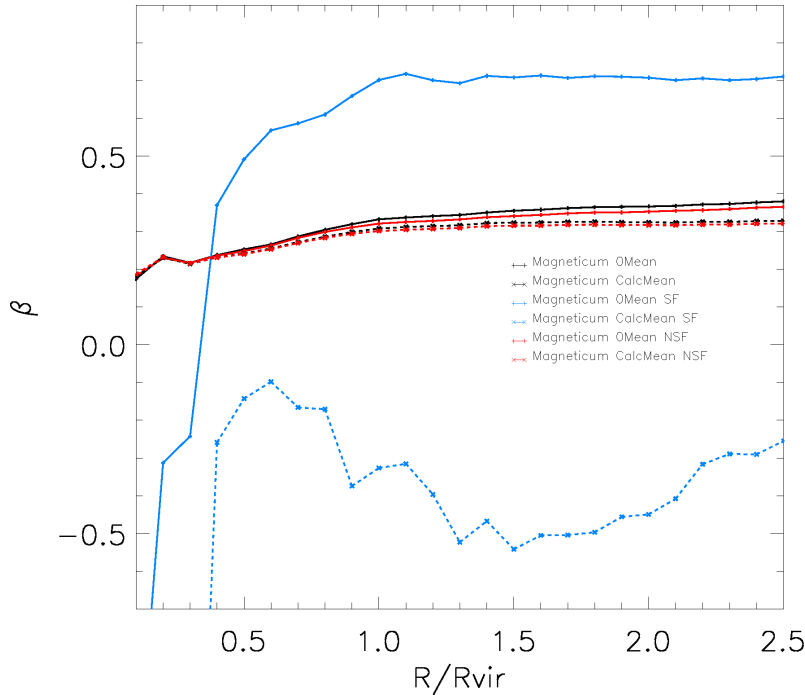
Figure 6.1: Competing mean methods in Magneticum at $z = 0.03$. The zero mean (isotropic) case ($\overline{x} = 0$) is indicated by a solid line, while the sample calculated mean case is represented by the dashed line. The colours correspond to star forming (blue), quiescent (red) and total (black) populations.

anisotropy parameter, this means that the dispersion is far larger when a zero mean is enforced, resulting in radial orbits, i.e. higher beta values in Figure 6.1 (solid blue line).

In contrast, when the mean is calculated from the sample, the dispersion is smaller, resulting in circularly dominated orbits (dashed blue line). The importance of these different mean calculations cannot be underestimated. The quiescent (red) and total (black) subhalo populations experience relatively little impact from different mean calculations due to a isotropically dominated distribution close to $\overline{x} = 0$. The impact on the star forming population, which is dominated by infall, i.e. radial orbits however, is extreme.

For all velocity anisotropy calculations the zero mean method is used since it is the only physically meaningful method. This is underscored further by the fact that it is the calculation which yields meaningful relative positions. Specifically, the total population in the zero mean method is located between the two subpopulations. This does not hold true for the sample calculated mean and suggests an inherent problem in this consideration. When referring to velocity anisotropy in the following the zero mean anisotropy is implied.

6.3   Bootstrapping

An error estimate is required in order to be able to quantify the error associated with the anisotropy parameter. Specifically, an error is calculated through bootstrapping

the various binned samples. This process leads to large errors when handling small samples, i.e. at small radii. The larger the sample becomes, the better the sample describes the underlying distribution. Practically, this means that the error estimation converges towards the standard deviation, in the case of a symmetric distribution.

A representative histogram of a typical bootstrapping result is shown in Figure 6.2. The figure depicts the total subhalo population in the first bin at $z = 1.7$ and was sampled 1000 times, resulting in a well approximated distribution. The first bin at $z = 1.7$ contains 49 subhalos, the anisotropy was calculated to be $\beta = -0.39$.

In order to be able to identify the 1σ confidence zone, i.e. the region with 68.2% of the population, the bottom and top percentile are included in Figure 6.2. The bottom percentile is located at 15.9%, as indicated by the left line, the middle line is located at 50%, i.e. the median, and the top percentile 84.1% is represented by the right line. The bootstrapping allows the calculation of error bars needed in upcoming comparisons with other simulations and observation.
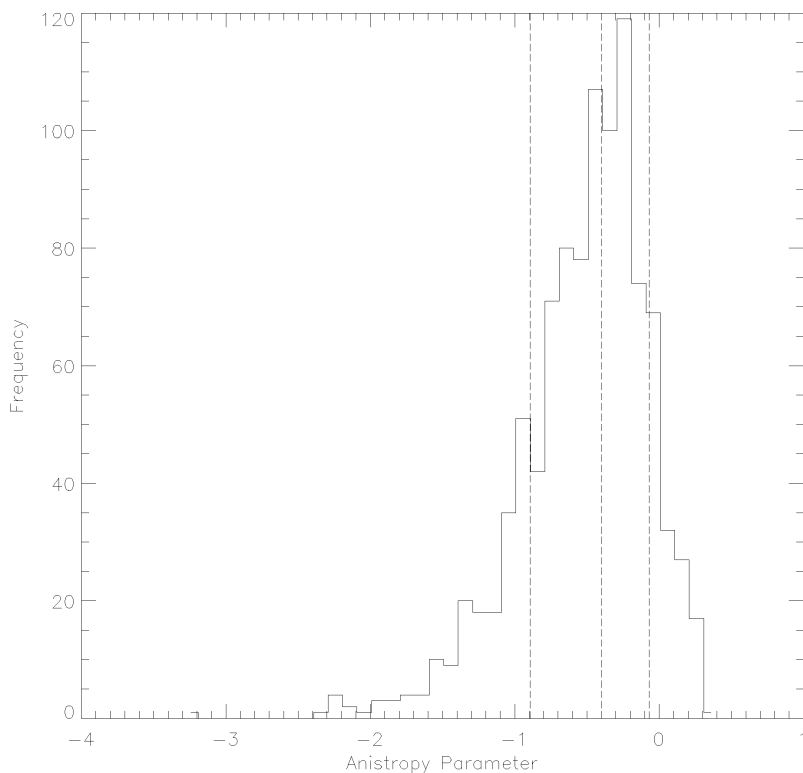

Figure 6.2: Representative frequency histogram of a selected sample used while bootstrapping. Left line bottom percentile (15.9%), middle line median (50%), right line top percentile (84.1%). Bottom and top percentiles are used to calculate the error of the given population after sampling it 1000 times.

6.4   Millennium Comparison

When analysing anisotropy profiles, or any data for that matter, the scientific value only arises when compared and contrasted to other results attained by independent

methods. That is why the Magneticum Pathfinder anisotropy profiles are presented here juxtaposed with Millennium results from Iannuzzi (2012), both of which are at redshift $z = 0$.

Figure 6.3 shows the anisotropy profiles of the total population (black) in the top panel and the star forming (blue) and quiescent (red) subpopulations in the bottom panel. At first glance, it is clear that the Magneticum and Millennium results are not consistent with each other. Both the shape and position of the profiles do not agree. In addition, the qualitative trends of the bottom panel are incompatible with each other. The Magneticum results depict the star forming subpopulation as generally being on a more radial orbit, whereas the Millennium results display the opposite behaviour; namely, the quiescent population is more radial than the star forming one.

The exact underlying calculations conducted in the Millennium case are not discussed. Nevertheless, a possible cause for the contradicting qualitative trends are differing mean calculation methods. Depending on the specific mean calculation, as discussed in section 6.2, it is possible for the relative subpopulation behaviour to change drastically.

In Figure 6.3, the ordering of the different populations is in compliance with statistical population expectations. Specifically, this means that the total population (top panel) is located between the two subpopulations (bottom panel). In contrast, this is not the case in Figure 6.1 for the non zero mean calculation (dashed line). The dashed black line in Figure 6.1 is not located between the two subpopulations, offering a quick tool to expose flawed mean calculation methods.

Both the Magneticum and Millennium profiles for all subhalos, independent of star formation, lie above isotropy, i.e. the horizontal dashed line in Figure 6.3. This is in line with expectations. Typically, clusters continuously accrete smaller structures such as groups and galaxies. This accretion process leads to radially dominated orbits. One would expect that subpopulations, which are dominated by infall, exhibit this behaviour more strongly.

Furthermore, one would expect the cluster to be closer to isotropy at lower radii since this region is likely to be the oldest. Hence, it has had more time to mix and redistribute the radial energy to tangential degrees of freedom. This, in turn, results in lower radii trending more strongly towards isotropy, unlike the outskirts, which, in the Magneticum case, have a far larger infalling subpopulation and are hence clearly radially dominated.

Interestingly, the Magneticum star forming subpopulation in Figure 6.3 (solid blue line) increases until it reaches $\sim 1\,R_{vir}$. Upon reaching this point, it remains constant. This suggests that the infalling star forming subpopulation $> 1\,R_{vir}$ has a common distribution of energy in tangential and radial direction. However, the proximity of the cluster leads to a preferentially radial orbital motion, resulting in a plateau. In other words, orbits only become a meaningful concept when a local over density causes gravitationally bound motions. At large distances from the cluster, this motion will always be dominated radially.

At radii $< 1\,R_{vir}$ the infalling Magneticum star forming subhalos become less radial and move towards isotropy. This suggests that mixing, i.e. the equipartition of energy, only becomes effective within the cluster. At very low radii $< 0.3\,R_{vir}$
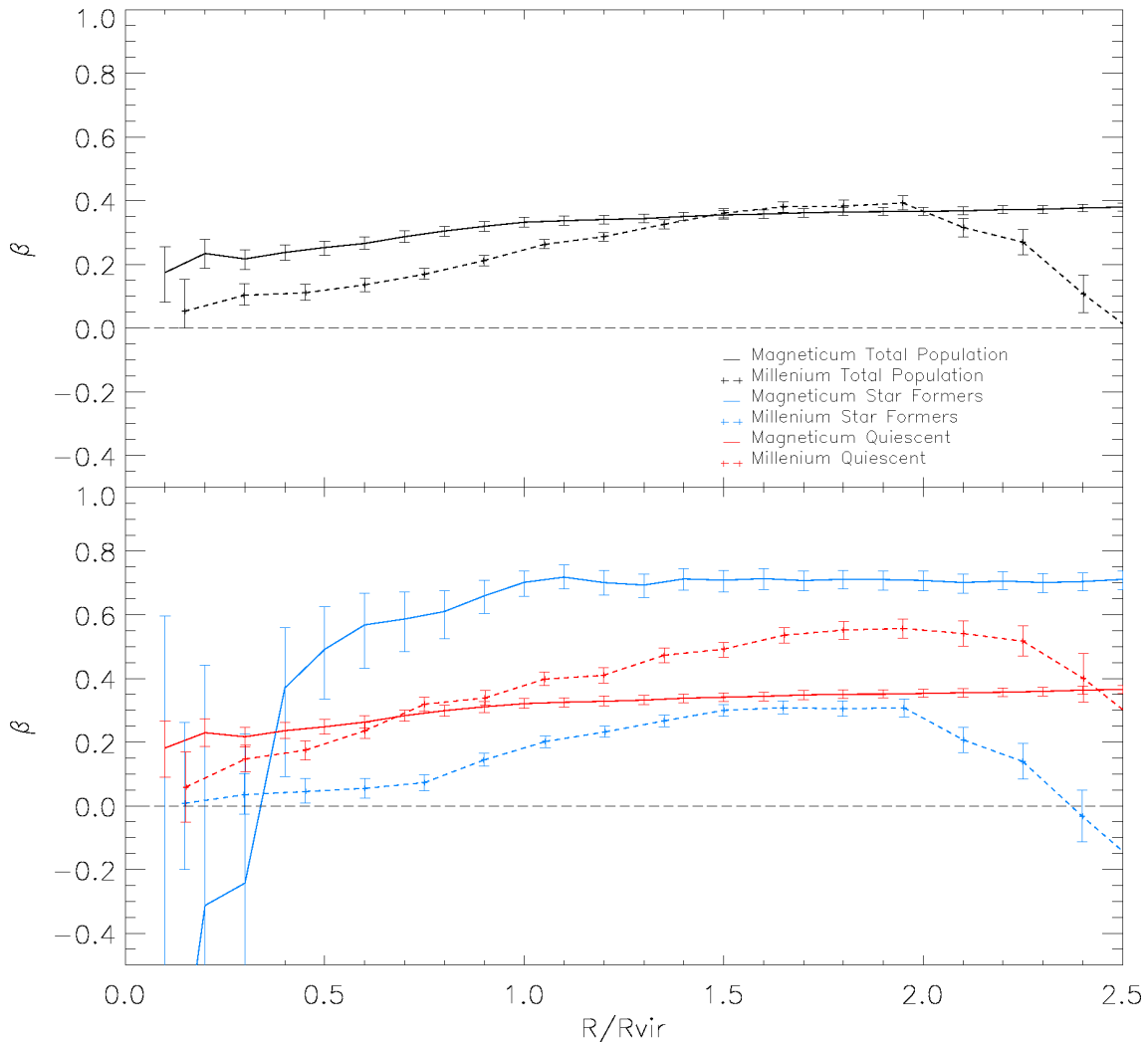
Figure 6.3: Cumulative radial profiles of anisotropy parameter at $z = 0.03$. Solid lines describe the Magneticum simulation, while the dashed lines describe the Millennium simulation (Iannuzzi, 2012). Top panel: total subhalo population profile. Bottom panel: star forming (blue) and quiescent (red) subpopulation profiles. Horizontal dashed line indicates an isotropic velocity distribution. Values larger than $\beta = 0$ correspond to more radial orbits, while negative values represent tangentially dominated orbits.

the number of star forming subhalos is small. This results in a large sample scatter, reducing the confidence and preventing trustworthy deductions.

The absence of meaningful statistics at low radii in the case of star formers in Magneticum has two main reasons. Firstly, very few star formers reach the inner regions of the cluster due to violent ram-pressure stripping, especially at $z = 0$. Secondly, the surviving subhalos spend little time in the inner regions. This is due to Keplerian dynamics. Subhalos have a lower likelihood to be located near the perihelion due to higher orbital velocities. On the other hand, subhalos have a higher likelihood to be closer to the aphelion since they move slower, the further they are from the focal point.

The Millennium results (dashed lines) in Figure 6.3 exhibit behaviour that is neither in agreement with Magneticum (solid lines) nor expected. For example, the

overall shape of the dashed red and blue lines in the bottom panel is extremely similar. However, the two subpopulations have drastically different characteristics, both with regard to their orbital motion and their sample size. One subpopulation is dominated by infall and is significantly smaller at low redshifts. The quiescent subpopulation, on the other hand, is typically older, more mixed and dominates the total population.

6.5   Comparison to Observations

To conclusively determine the extent of the validity of the Magneticum results, a comparison to observations is inevitable. As discussed in section 2.1, the results from Biviano et al. (2013) offer an unprecedented data set from which the velocity anisotropy at $z = 0.44$ is calculated. This comparison with observations is used to determine the success of Magneticum in simulating galaxy clusters and their underlying physics.

The observations from the CLASH cluster are plotted together with the corresponding Magneticum redshift results at $z = 0.44$ in Figure 6.4. As in Figure 6.3, the top panel depicts the total population both from Magneticum (solid line) and Biviano et al. (2013) (dashed line). The bottom panel displays the two subpopulations with the shaded region representing the 1σ confidence zone of the observations. Here, the star forming subpopulation obtained through observations is represented by a blue dashed line encompassed by the blue confidence region. Similarly, the quiescent subpopulation is depicted by the red dashed line enclosed by the red 1σ confidence zone. In line with previous plots, the Magneticum results are portrayed by the solid lines, adhering to the same colours as is the case for observations.

Observations by Biviano et al. (2013) and Magneticum are in fine agreement. The overwhelming majority of points lie within each other's 1σ error regions and bars respectively. All but six data points out of all populations have overlapping error zones. The general shape of the Magneticum profiles concur with observations.

The overall behaviour is similar to the one exhibited by Figure 6.3 at $z = 0$. Specifically, mixing of the infalling subpopulation only begins $< 1\,\mathrm{R_{vir}}$. In addition, lower radial bins are closer to isotropy due to their on average longer timespan within the cluster. This, in turn, allows the transfer to tangential degrees of freedom through dynamical friction. Similarly, the error scatter towards lower radii increases due to smaller sample sizes.

In contrast to Magneticum, Biviano et al. (2013) finds that the mixing or trend towards isotropy begins at larger radii, $\lesssim 1.6\,\mathrm{R_{vir}}$. Provided the observations accurately portray reality, this implies that the equipartition of energy is already efficient in the outskirts of the cluster. In other words, dynamical friction is causing a redistribution of energy at significantly higher radii than anticipated by Magneticum.

Despite this intriguing possibility, it is important to recall that the observations are based on a single cluster with ~ 600 members. On the contrary, Magneticum utilises 20 clusters to derive its statistics, totalling 6356 stellar subhalos within a $2.5\,\mathrm{R_{vir}}$ radius at $z = 0.44$. As a result, the stacked synthetic Magneticum cluster has ~ 10 times more subhalos than the observed CLASH cluster at this redshift.
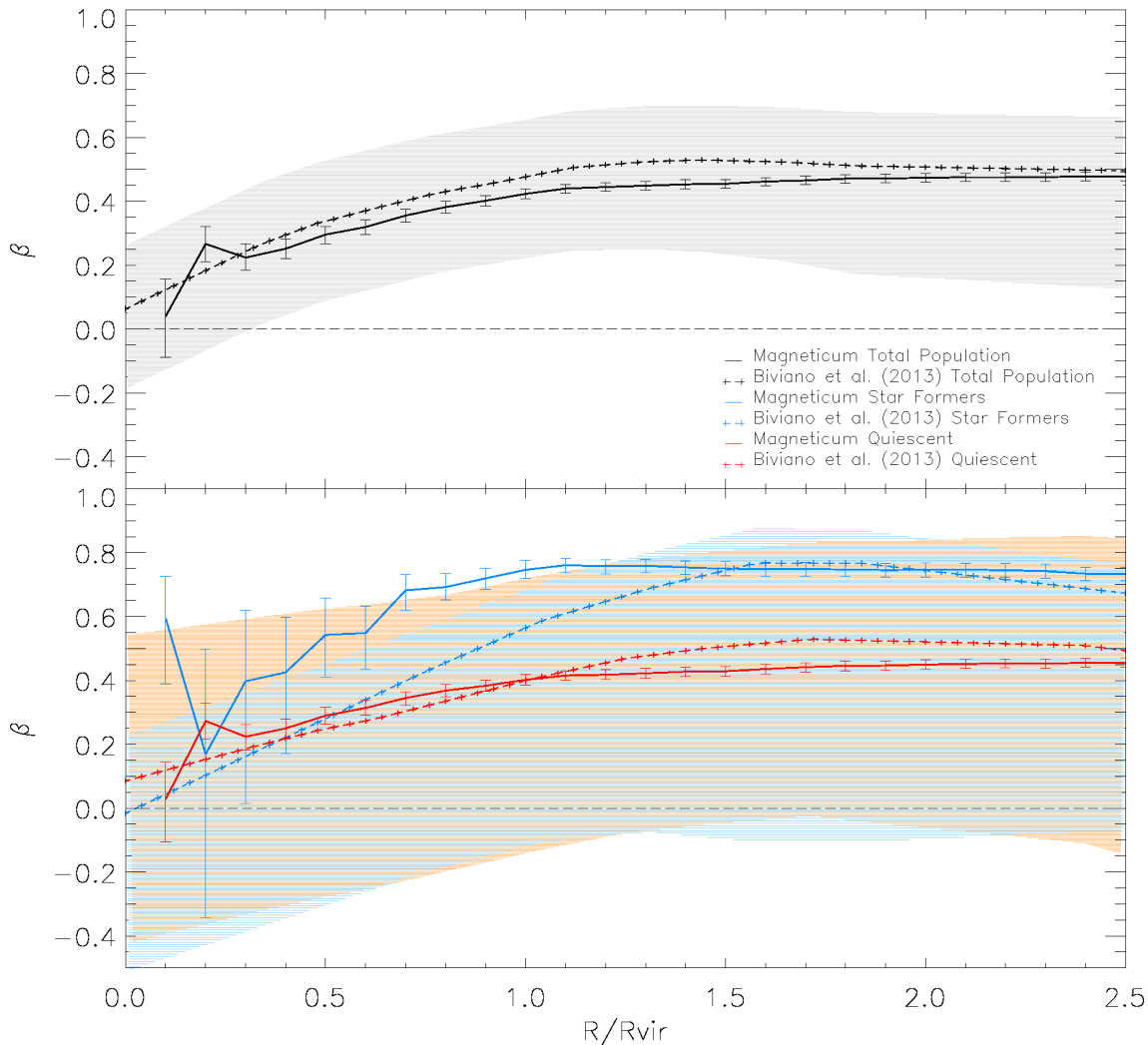
Figure 6.4: Cumulative radial profiles of anisotropy parameter at $z = 0.44$. Solid lines describe the Magneticum simulation, while the dashed lines describe the CLASH observations (Biviano et al., 2013). Top panel: total subhalo population profile. Bottom panel: star forming (blue) and quiescent (red) subpopulation profiles. Shaded regions correspond to the 1σ confidence zone of the respective observations. Horizontal dashed line indicates an isotropic velocity distribution. Values larger than $\beta = 0$ correspond to more radial orbits, while negative values represent tangentially dominated orbits.

The slightly different curvature of the profiles might be the result of different cluster sizes and types. Out of the 20 Magneticum clusters only one has more mass $(1.52 \cdot 10^{15}\,\mathrm{M_\odot})$ than the CLASH cluster $((1.4 \pm 0.2) \cdot 10^{15}\,\mathrm{M_\odot})$. This massive Magneticum cluster is also the sole cluster at $z = 0.44$ with more subhalos (730) than the observed cluster (~ 600) (Biviano et al., 2013).

Projection effects are a likely cause of the differing profiles. While calculating the Magneticum profiles, an exact sphere is constructed and each shell is evaluated. Observations, on the other hand, likely overestimate the number of galaxies due to the circular projection of a cylinder along the line of sight. At larger radii, this effect is small due to large populations and few interlopers. In contrast, at low radii interlopers strongly impact the star forming subpopulation. The star forming

subpopulation at lower radii is small and hence few interlopers, typically not on radial orbits, have a greater impact.

Independent of these considerations, the $1\,\sigma$ confidence zones from the observations are quite large, possibly shrouding the true velocity anisotropy. The anisotropy observations were obtained by inverting the Jeans equation and smoothing the background-subtracted binned number density profiles. This process yields less fluctuating profiles as depicted in Figure 6.4.

Furthermore, it is important to differentiate between true mixing and perceived mixing due to selective removal of certain galaxies within a subpopulation. For example, galaxies on a radially dominated orbit are more likely to have a higher infall speed. These higher speeds result in more efficient ram-pressure stripping. Consequently, they are removed from the star forming subpopulation. Radial galaxies are preferentially quenched first and thus the star forming subpopulation in both Magneticum and Biviano et al. (2013) in Figure 6.4 show a tendency towards isotropy.

6.6   Radial Profiles

The analysis of radial profiles provides a facilitated examination of objects that are assumed to have a spatially isotropic distribution. Even if this assumption is not true for every cluster, when clusters are stacked, the radial profile analysis provides insights into global distributions. The results are the smooth cumulative profiles depicted in Figure 6.5. The figure shows the radial profiles of the normalised velocity, number density and the number of subhalos within a radial spherical volume shell. As such, Figure 6.5 helps to illustrate the different properties of the star forming and quiescent population. For a comparison to $z = 0.44$ and $z = 1.70$ refer to the appendix, i.e Figures 8.7 and 8.8.

In every panel the total population (black) is extremely similar to the quiescent population (red). This is due to the total population being dominated by quiescent subhalos at $z = 0.03$. As a result, star forming subhalos (blue) have little or no impact on the behaviour of the total population. Interestingly, star formers exhibit a fundamentally different behaviour in their radial profile in comparison to their quiescent counterparts.

The top panel in Figure 6.5 depicts the normalised root mean square velocity. One can observe that star formers have a much lower velocity at low radii $\leq 1\,\mathrm{R_{vir}}$ compared to quiescent star formers. This is likely due to the faster star forming subhalos being quenched more efficiently and, thus, leaving only slow star forming subhalos at low radii. The selection effect of fast star formers being removed preferentially becomes stronger at smaller radii. This is plausible because ram-pressure stripping becomes more efficient at lower radii and thus only slow subhalos can retain their star formation.

Outside the virial radius $\geq 1\,\mathrm{R_{vir}}$, a difference is no longer visible between star forming and quiescent subhalos. This is due to the lack of a ram-pressure stripping driven selection effect at larger radii. The red and blue lines begin to diverge at the radii at which quenching begins to have an impact on star forming subhalos. Hence, Figure 6.5 nicely illustrates the orbital selection mechanism which preferentially depletes the fast star forming population.
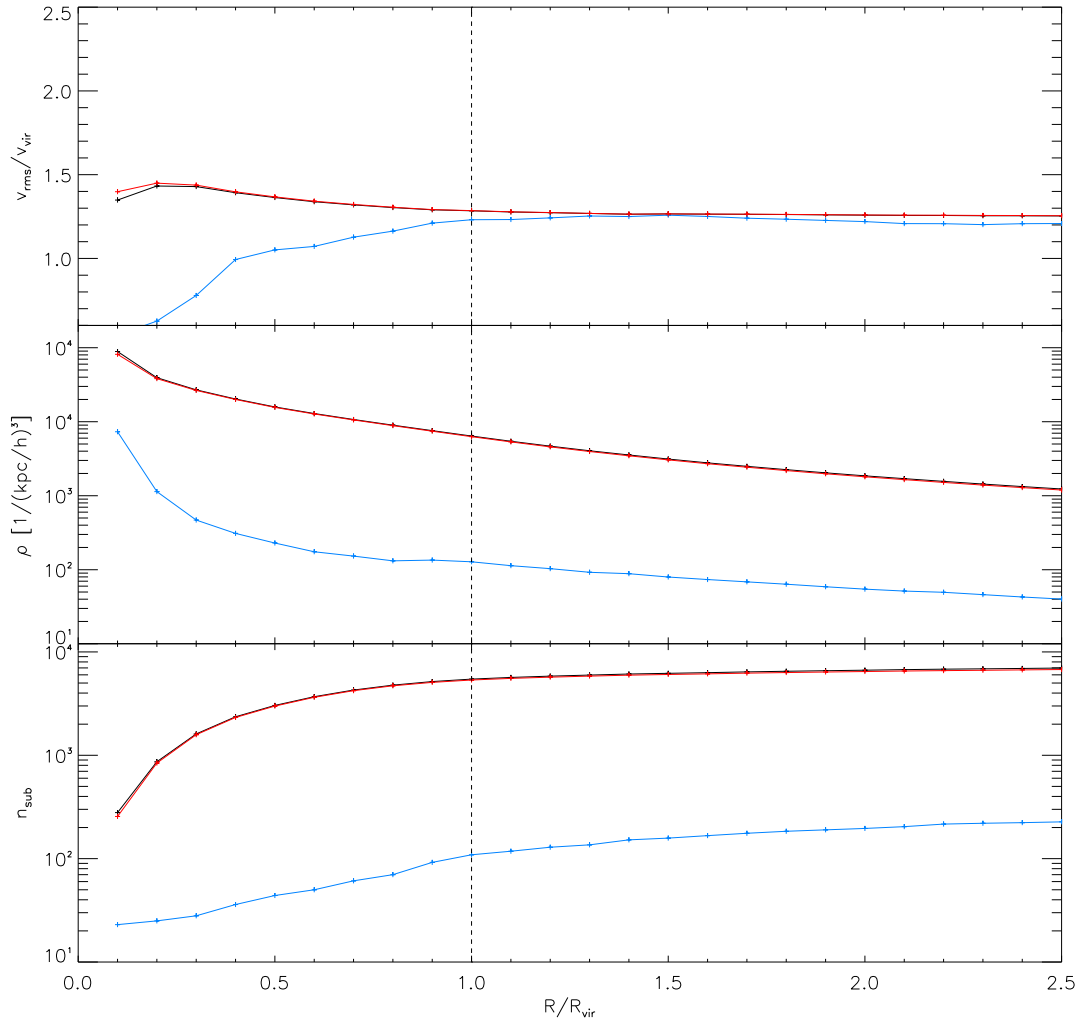
Figure 6.5: Cumulative radial profiles of 20 stacked Magneticum clusters at $z = 0.03$ for total population (black), star formers (blue) and quiescent (red) subhalos. Top panel: root mean square (rms) velocity normalised to the virial velocity v_{rms}/v_{vir}. Middle panel: radial number density profile in units of $[1/(kpc/h)^3]$. Bottom panel: number of subhalos in a given radial shell. The vertical dashed line corresponds to the virial radius.

The middle panel in Figure 6.5 shows the number density of subhalos within a spherical shell. Although the number of subhalos decreases with lower radii (bottom panel), the number density increases (middle panel). This is the result of the volume $V = \frac{4}{3}\pi(R^3 - r^3)$ decreasing as a function of the difference of outer shell radius cubed R^3 and inner shell radius cubed r^3. With small volume shells at low radii, the number density thus increases despite the decrease in the number of subhalos.

The logarithmic axis of the bottom two panels emphasises that the overwhelming majority of subhalos are quiescent at low redshifts. Furthermore, the bottom panel illustrates that the number of star forming subhalos decreases faster at lower radii $\leq 1\,\mathrm{R_{vir}}$. This decrease, which is not evident in the same manner in the quiescent

subpopulation, further highlights the depleting impact the quenching within the virial radius has on the star forming population. At low radii $\sim 0.3\,R_{\mathrm{vir}}$, only 28 star formers remain in the stacked cluster, while almost 1581 quiescent galaxies inhabit the same volume.

Chapter 7

Discussion

Using the unprecedented accuracy of Magneticum Pathfinder, 20 clusters at varying redshifts were studied. These considerations yielded a broad, yet detailed, picture of the mechanisms that govern galaxy evolution. Through phase space diagrams, orbital tracking and velocity anisotropy profiles, the underlying physics of the simulated clusters was revealed. The goal of these various methods is to increase the understanding of quenching mechanisms in galaxy clusters.

7.1   Data Reduction

Rather than considering the individual particles of the simulation, the results from `SUBFIND` were used, i.e. subhalos. Within these subhalos all the relevant information is conglomerated. As such, they form the basis of all deductions acquired through the simulation. All the values depicted throughout this thesis are, hence, derived from `SUBFIND`.

As a result, in addition to the performed data reduction, the limitations of `SUBFIND` also apply. `SUBFIND`, in turn, is based on the Friends of Friends (`FoF`) algorithm. However, both in this work and others, results of the `SUBFIND` algorithm are in fine agreement with observations. In addition, the algorithm is among the best postprocessing algorithms currently available and reflects the state of the art standard implemented in Magneticum Pathfinder.

Aside from the high standard with which the data reduction was conducted, a number of improvements or future projects are available. In order to reduce the degree of entanglement of different underlying mechanisms, the data reduction in section 3 could further be specified by more extensive considerations. Different subsamples of the galaxy clusters listed in Table 3.1 could be considered. Specifically, an inquiry into the effect of different cluster masses on the quenching mechanisms is of interest.

Opportunities for future projects include the investigation into individual clusters, i.e. creating detailed density, pressure and temperature maps. These considerations would yield meaningful insights into the dynamics of the cluster and its ICM. With this investigation into, amongst other things, the dynamics of the ICM, interactions between the ICM and galaxies could be studied more closely. In addition, properties of clusters could be ascertained, i.e. whether or not the cluster is

considered a cool core or not. This could then be set into perspective by factoring in the accretion history.

7.2   Phase Space

The comparison between one observed cluster depicted in Figure 4.4 and 20 simulated clusters in Figure 4.2 was conducted to gain an understanding of the statistical behaviour on the simulation side and to compare this to observations. In contrast to observations, the phase space diagrams attained through simulations do not suffer from projection effects. This means that a comparison between observations and simulations is only possible when the phase space is either deprojected or projected to reflect the respective other method. This, however, is not a trivial task.

While simulations can easily account for different radial shells and hence construct a sphere, observations need to exclude interlopers. To compare the phase space diagrams in section 4 with observations, one needs to consider a projected cylinder, as is the case in observations, rather than a sphere. However, the choice of orientation of this cylinder and the resulting line of projection impact the distribution of the rendered phase space diagram, which is especially the case for unrelaxed clusters. Nonetheless, a projection of various figures, where comparable observations exist, is in preparation. Until then, comparison between the projected phase space diagram in Figure 4.4 and the three dimensional phase space in Figure 4.5 will need to suffice.

The difference in relative radii at which quenching becomes effective in Figures 4.2 and 4.4 suggests different quenching mechanisms. However, this is only the case provided the different scale radii in Magneticum r_{vir} and the observations r_{200} correspond to similar physical radii in both systems. Although different clusters can exhibit different strengths of quenching mechanisms depending on their properties, one would naturally assume that with similar properties similar quenching would occur. Despite differences between the simulated clusters and the one observed, broadly speaking they are alike. The synthetic Magneticum cluster at $z = 0.44$ is mostly quenched above $\gtrsim 0.7\,\mathrm{R_{vir}}$, whereas the observed cluster at $z = 0.44$ exhibits strong quenching around $\sim 1\,\mathrm{R_{vir}}$, as indicated by the magenta line in Figure 4.4. Due to the lack of a larger statistical sample with regard to observations, the differences exhibited by Figures 4.2 and 4.4 cannot be conclusively identified.

Possible reasons for the different abundances of subpopulations at different radii, especially in the outskirts, include shocks, resolution effects and statistical fluctuations. Violent shocks trigger star bursts, after which almost no further stars are formed. Galaxies which have recently experienced shocks thus look blue in colour observations, although technically they have a star formation rate close to zero. As such, they are classified to be star formers in Biviano et al. (2013), but are considered quiescent in simulations which consider the specific star formation rate. On small time scales this leads to an underestimation in Magneticum and an overestimation of star formers in observations with regard to each other.

Due to resolution limitations in simulations, not all star formation is resolved. This effect impacts smaller galaxies more than massive ones. The likelihood of an individual gas particle being converted into a stellar particle with a portion of the

original mass is small. The conversion is dependent on the local environment and the implemented physics. Generally, the less particles, i.e. the smaller the subhalo, the less likely a conversion becomes. As a result, star formation, especially in low mass galaxies, is underestimated in Box2/hr of the simulation. Box2/hr is a compromise of size and resolution and, as such, it has limitations at the low mass end of subhalos.

7.3 Blueness Evolution

Tracing individual subhalos and correlating their radial distance from the centre of clusters with a measure for their star formation rate is one of the key benefits of the inspection of this simulation. The dynamics which are uncovered during this investigation yield insights otherwise difficult to attain. Due to the nature of these insights, a comparison to static observations is somewhat complicated.

A comparison of the considerations in section 5 to observations is further hindered by the fact that the simulation yields qualitative rather than quantitative results. Consequently, section 5 has eluded comparisons to observations. Hence, the blueness evolution is only discussed with regard to improvements within the scope of the existing investigation.

The most significant obstacle impeding clear deductions is the lack of merger trees. The phase space investigation considered cluster evolution from $z = 1.7$ to the present. In contrast, section 5 only covers a redshift range from $z = 0.54$ to $z = 0.03$. This is due to a high merger tree failure rate above this redshift. To ensure the integrity of the merger trees, only this limited redshift span was used.

Nonetheless, a small percentage of subhalos experience difficulty within this range and were excluded from Figure 5.2. The effects of a large number of corrupted merger trees is visible in the appendix in Figure 8.6. Although the few subhalos experiencing issues in Figure 5.2 were not plotted, slight corruptions are visible close to $1\,\mathrm{R_{vir}}$. These issues are characterised by sharp almost vertical lines (top panel), indicating non physical orbital jumps.

These effects are negligible compared to the effect a corrupted cluster halo merger tree has on the tracking. Namely, all radial distances are rendered useless if the cluster halo temporal tracking experiences difficulties. However, this phenomenon typically occurs at higher redshifts than the interval utilised in section 5.

The relatively small redshift range, compared to the potentially possible range permitted by Magneticum, limits the feasibly attainable quantitative deductions. The primary goal of implementing a higher redshift range is to have the opportunity to investigate the effect of quenching through strangulation more closely. Specifically, a larger time span of constant subhalo population would become available. This means that the general behaviour of grouped subhalo blueness could be evaluated.

Currently, this is challenging because, due to the shifting of the time axis, the population in a given time span fluctuates. The fluctuations impact the deductions and need to be excluded to definitively ascertain the quantitative degree of correlation between radial distance and blueness. With the current $\sim 5\,\mathrm{Gyr}$ time span, a far too small interval of constant population exists to truly examine the correlation in a quantitatively meaningful way.

In contrast, a larger time interval would permit the cropping of the interval to the point of constant population, while leaving a cropped interval large enough for meaningful deductions. Once this cropping has been executed, the remaining interval can be statistically evaluated. In other words, the infalling star forming population can be averaged. Similarly, the blueness can be statistically reduced to yield a blueness gradient. Plotted together in an single diagram, the degree of correlation can be determined.

This process would also allow a closer investigation into the relative effectiveness of different quenching mechanisms. The infalling population could easily be split into a fast, normal and slow component according to the respective infall velocity. Naturally, one would expect different quenching mechanisms to be dependent on subhalo velocities. For example a slow subhalo might experience a larger portion of its quenching to be the result of strangulation. A slow subhalo spends more time in the outskirts of the cluster and is thus more prone to longtime scaled quenching, such as strangulation. In comparison, a fast subhalo does not experience as much strangulation, but rather it experiences stronger ram-pressure stripping. Not only does ram-pressure stripping scale with velocity, but the fast subhalo spends less time in the outskirts. As a result, it cannot be effectively quenched by long timescaled quenching mechanisms.

As discussed in section 7.2, Magneticum underestimates the degree of star formation in subhalos due to resolution limitations. This is especially true for subhalos with low star formation rates and small mass. The number of gas particles within a subhalo is limited and if densities cannot reach the star formation threshold, no star formation occurs. Specifically, if star formation is not in the order of a stellar particle $\sim 3.5 \cdot 10^7 M_\odot/h$, no gas will be converted to stars.

As a result, ram-pressure stripping, which typically operates below $\lesssim 0.5\,R_{\mathrm{vir}}$, is more effective at a given radius in the Magneticum simulation (Treu et al., 2003). Low degree of ram-pressure stripping, i.e. limited effectiveness, will have a sufficiently large influence, provided the resolution is limited. As such, Figure 5.2, depicts slightly higher radii at which ram-pressure stripping is effective than what we would expect from observations.

7.4   Anisotropy Profiles

Despite the valuable insights offered by the study of anisotropy profiles, an important concern remains. The velocity anisotropy is only a useful expression when the objects considered are bound, i.e. the galaxies have a closed orbit. This is the largest caveat when regarding the anisotropy profiles, especially at high radii. Hence, profiles were only studied to a maximum radius of $2.5\,R_{\mathrm{vir}}$.

The fundamental differences portrayed by the two simulations in Figure 6.3 are likely the result of a different implementation of the underlying physics. While Magneticum simulates the hydrodynamics of the gas required for star formation, Millennium only employs a semi-analytic approach. The more comprehensive Magneticum simulation likely describes the physical phenomena more accurately. Not only is the implementation of the astrophysical processes more extensive, but Magneticum is also in good agreement with observations regarding the pressure profiles of

the intracluster medium (Planck Collaboration et al., 2013; McDonald et al., 2014). These agreements are important because they provide the physical foundation for the successful simulation of phenomena such as ram-pressure stripping.

When comparing Millennium to Magneticum, a strong disagreement is apparent. Not only do the results not have the same shape or curvature, but they qualitatively disagree. Specifically, the star forming population appears to be on more tangential orbits than the quiescent population when considering the Millennium results. The reverse is true when studying the results obtained through the Magneticum simulation. The Millennium simulation is a dark matter only simulation and, as such, the galactic velocity dispersion within the cluster is derived from the dispersion within the dark matter. Without truly modelling stars and gas, the effects of ram-pressure stripping cannot be conclusively evaluated.

The Millennium simulation is hence less able to successfully simulate the fundamental subgrid physics, elementary to understanding the quenching mechanisms. As a result, the orbital selection effects visible in Magneticum with regard to the phase space inquiry and the anisotropy profiles cannot be resolved in a meaningful way. This becomes visible when considering the similar shape of the quiescent and star forming subpopulation profile in Figure 6.3.

Naively one would expect the profiles of fundamentally different galaxy subgroups to exhibit a different behaviour, especially if their classification is strongly influenced by the cluster environment. However, the profiles of the star forming and quiescent Millennium subpopulations in Figure 6.3 do not display a significantly different nature. It merely seems that they experience a vertical offset to one another. Considering these points, the confidence in the capability of the Millennium simulation to successfully simulate galactic orbital behaviour in clusters erodes.

As with any theoretical model, the profiles depicted in section 6 are only meaningful when compared to empirical results. The comparison to observations by Biviano et al. (2013) yielded a close agreement with the results obtained through the Magneticum Pathfinder simulation. Nonetheless, it is important to accentuate the different methods with which the anisotropy profiles were calculated.

The observed velocity anisotropy is the result of an extended data reduction. Firstly, a fiducial mass profile was determined. The fiducial mass profile employed by Biviano et al. (2013) corresponds to the NFW best-fit of the lensing mass profile obtained by Umetsu et al. (2012). Subsequently, the fiducial mass profile was used during the inversion of the Jeans equation. This problem was first solved by Binney & Mamon (1982). However, the analysis in Biviano et al. (2013) solves the equations according to Solanes & Salvador-Solé (1990). As such, the procedure is almost fully non parametric, provided the mass profile is specified (Biviano et al., 2013).

The number density profiles are not fitted, but rather the LOWESS technique is used to smooth the background-subtracted binned number density profiles (Gebhardt et al., 1994). Through the use of Abel's equation, as described in Binney & Tremaine (1987), the smoothed profiles are inverted numerically. This yields the number density profiles in three dimensions. For a more extended discussion refer to Biviano et al. (2013).

The leading source of error of this method are the uncertainties associated with the line of sight dispersion. The observational confidence zone depicted in Figure 6.4

is calculated through modifications of the beta profile. These modifications are then inverted to yield a wide grid of predicted line of sight velocity dispersion profiles (van der Marel, 1994). This reversed method is employed because error propagation through the Jeans inversion is infeasible (Biviano et al., 2013).

Although this method is state of the art, issues remain. For one, the entire calculation of the velocity anisotropy profiles hinges on the fiducial mass profile. The NFW profile, which was assumed and fitted, can be the source of large errors. Depending on the true nature of the mass profile, the NFW fit by Umetsu et al. (2012) does not necessarily fit well along the entire profile. This is especially significant at high and small radii, where the deviations from the NFW profile are likely to be largest. The error on quantities like the concentration $c_{200} = 6 \pm 1$ of the observed cluster are large and, hence, the fitted NFW profile could easily not accurately describe the actual profile.

As discussed in 7.2, a fundamental limitation of observations are projection effects. Interlopers have a potentially major impact on the calculated anisotropy profile. Given solely the line of sight velocity, it is virtually impossible to conclusively attribute a galaxy to an individual radial bin of a cluster. Subsequently, the calculation of the observed anisotropy profile will always be subject to inaccuracies. To truly compare the observations with the simulation, one would have to project the simulation into 2D and then calculate the anisotropy through the inversion of the Jeans equation.

In addition, ambiguity in the definition of the star formation criterion gives rise to different categorisations of galaxies. The observers utilise colour-colour diagrams to identify star forming and quiescent galaxies (Mercurio et al., 2014). In contrast, the criterion applied in the data reduction of the simulation considers the specific star formation rate in dependence of redshift. This means that galaxies can be considered quiescent in one criterion and star forming in the other. The simulation criterion has a much higher temporal resolution. Once not enough stars are being formed, the galaxy is considered quiescent. This, however, does not account for recently formed stars, which impact the classification on the colour-colour diagram. As such, Magneticum typically underestimates the amount of star formers compared to observations.

To investigate the effect of the Magneticum star formation criterion $sSFR \cdot t_{Hubble} > 0.3$, an adaptation is in preparation. Specifically, the value above which a subhalo is considered star forming will be modified. Since Magneticum is expected to underestimate the amount of star formers, the value of 0.3 will be reduced and the subsequent effect will be studied. However, this will likely require both a higher spatial and temporal resolution. If this investigation does not yield meaningful results, a typical time scale, $t_s b$, after a star burst will be introduced. As long as the subhalo is below this time scale, it will continue to be considered a star forming subhalo even if star formation has ceased. This investigation might facilitate the exposure of the underlying mechanism responsible for the different curvatures in Figure 6.4.

Chapter 8

Conclusion

A number of distinct insights become apparent when considering the results obtained with the Magneticum Pathfinder simulation. Most importantly, the results, when compared, coincide with observations. With regard to the investigation into the effect of galactic orbits on internal evolution, we find that ram-pressure stripping is the dominant quenching mechanism in clusters at low redshifts. The vast majority of star forming subhalos are violently quenched within their first passage through the cluster.

The phase space inspection shows that the star forming subpopulation is dominated by infall, especially at lower redshifts $z < 0.5$. This is supported by the fact that, independent of redshift, the majority of the star forming population has a negative radial velocity, i.e. is infalling. The effect is smaller at high redshift $z \sim 1.7$ and becomes increasingly strong towards low redshifts. At $z = 0.03$, 99.9% of the star forming subpopulation has a negative radial velocity. This also implies that star formers do not survive their first passage, but rather are quenched and, hence, become part of the growing quiescent subpopulation.

The degree of subhalo quenching in clusters is related to the orbital initial conditions. Although the vast majority of star forming subhalos are quenched around 0.5-1 R_{vir}, a tiny population with radii greater than $\sim 1\,R_{vir}$ is able to remain star forming. The overlay of all redshifts considered in Figure 4.5 shows that, if star forming subhalos have a strong tangential orbit and are able to remain outside the virial radius, they survive the first passage. This is supported by the existence of a distinct, almost symmetric population with a small radial velocity component in Figure 4.5.

This conclusion is of paramount importance. Although the exact degree of ram-pressure stripping and the success of simulating it is a matter of debate, the existence of the mechanism is not. More precisely, the simulation fine-tuning does not likely capture the exact radius at which ram-pressure stripping is dominant however, it beautifully illustrates the orbital selection effect which is a direct consequence of said stripping. As such, Magneticum is able to simulate orbital selection mechanisms and produce a realistic representation of galaxy clusters.

In Figure 5.2 we see that once the star forming subhalos pass below $1\,R_{vir}$, the overwhelming majority are quenched within 1 Gyr. One of the few subhalos (orange) that does not experience rapid but rather slow quenching is a subhalo which has an

extremely shallow orbit. In other words, if a subhalo is able to maintain a relatively large radial distance $\gtrsim 1\,\mathrm{R_{vir}}$ by having a strongly tangentially supported orbit, it will be quenched on a longer time scale, i.e. it will be strangled rather than stripped.

The majority of subhalos are quenched in a short time span $\sim 1\,\mathrm{Gyr}$, compared to typical orbital periods $\sim 3\,\mathrm{Gyr}$, observed in Figure 5.2. This consideration, in combination with the phase space evaluation, strongly suggest that ram-pressure stripping is the dominant quenching mechanism in clusters. This conclusion is supported by the fact that the observed quenching mechanism has a short time scale and is strongly correlated to radial distance. In addition, ram-pressure stripping removes the cold gas component and thus disables future star formation, as indicated by Figure 5.2.

The velocity anisotropy profiles of the Magneticum simulation do not agree with the Millennium simulation profiles calculated by Iannuzzi (2012). Due to the fundamental differences of the two simulations, discussed in section 7.4, this does not come as a surprise. The behaviour of the quenching mechanisms and their effect on subhalo selection are still a matter of debate and, as such, discrepancies are not uncommon. However, the contrast further accentuates the necessity for extensive comparisons with observations.

Magneticum is in good agreement with observations from Biviano et al. (2013), as illustrated by Figure 6.4. Not only is the overall shape of the profiles similar, but the majority lie within each other's 1σ confidence zones. As such, the stacked sample of clusters considered in the Magneticum simulation aptly describes the behaviour of a physical CLASH cluster at $z = 0.44$. The observations are the first to separately consider star forming and quiescent subpopulation profiles. They provide further evidence that the star forming subpopulation is characterised by radial orbits and is, hence, likely dominated by infall.

In addition, the observations support the claim that subhalos at lower radii $< 1\,\mathrm{R_{vir}}$ begin to be selectively, quenched dependent on their relative orbits. More radial star forming subhalos are quenched more effectively by ram-pressure stripping. This is due to the fact that more radially orbiting subhalos are typically faster at a given radius than tangentially orbiting subhalos. This is highlighted by the decrease in root mean square velocity of the star forming subhalos in Figure 6.5. These combined considerations show that radially dominated star forming subhalos are quenched more effectively and thus more quickly than the subhalos with a more tangential orbit. This selection effect leads to the visible decrease in the star forming subhalo profiles in Figure 6.4 at lower radii.

In summary, the results suggest three fundamental conclusions. Firstly, the dominant quenching mechanism in galaxy clusters is ram-pressure stripping. Secondly, ram-pressure stripping is sufficiently effective to quench the overwhelming majority of star formers in $\sim 1\,\mathrm{Gyr}$ during their first passage for redshifts $z < 0.5$. Thirdly, ram-pressure stripping preferentially quenches radial star forming subhalos.

Acknowledgements

First and foremost, I would like to thank Dr. Klaus Dolag, Prof. Andreas Burkert and Dr. Rhea-Silvia Remus for providing me with opportunities, suggestions and support throughout my thesis. Klaus, I want to thank you for supervising me throughout this thesis and always taking time out of your busy schedule to answer all my questions. I would like to thank Andi and Klaus for inviting me into a group, which encourages questions, critical analysis and scientific debate. Thank you Andi for providing valuable insights and widening the scope of my research, so as to be able to compare my findings with those of others. Thank you Rhea for the countless interesting discussions, for never failing to teach me new perspectives and for always taking the time to answer my questions.

Furthermore, I would like to thank the entire CAST group, especially (in aphabetical order) Adelheid (not only is your positivity and refreshing outlook on life contagious but you have also taught me a great deal about galaxies), Adrian, Alex (you have always managed to convey exceedingly complicated numeric techniques in a simple manner), Felix (you have mentored me and you have answered and entertained countless questions, while never failing to be uplifting in the process), Geray, Lennart (although our discussions sometimes strayed they always continued to be interesting), Stefan, Tadziu (I remain in awe with regard to what is possible when one is fluent in every programming language) and Uli. All of you and more always took time and energy to answer questions and debate research.

I want to thank my parents for always encouraging me and for nourishing my curiosity thoughout my childhood. You have given me the tools and support that have allowed me to begin and, ultimitely, conclude my studies.

Lastly, I would like to thank all other colleagues and friends for inputs, discussions and ecouragement.

Appendix

For the sake of completeness the following plots are included. Figures 8.1, 8.2, 8.3, 8.4 and 8.5 show the temporal evolution of the stacked phase space of the first 20 clusters at varying redshifts. The redshift is indicated on every plot and ranges from $z = 1.7$ to $z = 0.04$. Figure 8.6 depicts the impact of failed merger trees on the tracking of subhalos in the cluster with Halo ID $= 004$ at $z = 0.54$. Lastly, Figures 8.7 and 8.8 display the cumulative radial profiles of the 20 stacked clusters at $z = 0.44$ and $z = 1.7$ respectively.
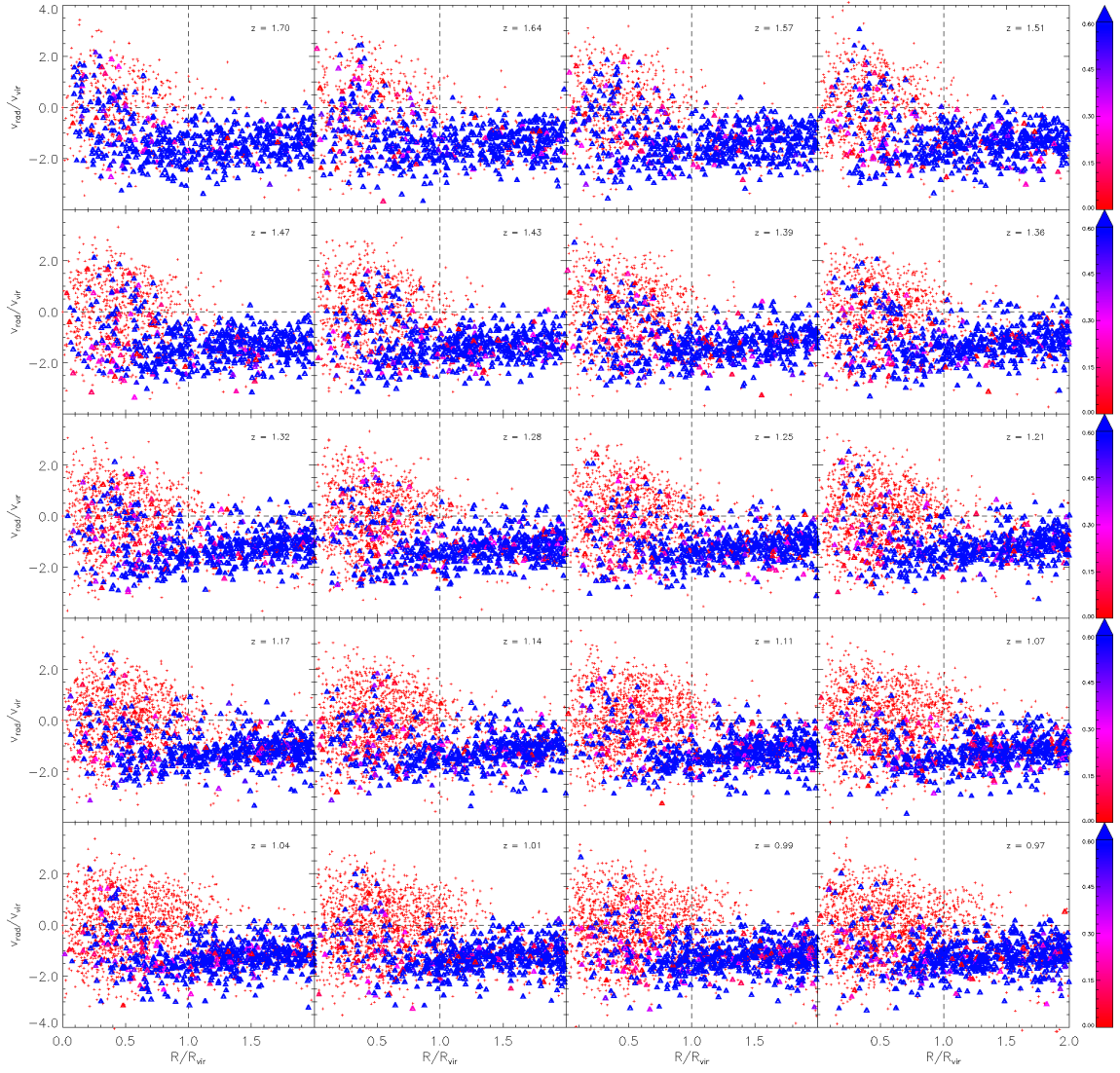
Figure 8.1: Multiplot of phase space of 20 stacked clusters at redshifts $z = 1.7$-0.97. The figure shows the normalised velocity $[-4, 4]$, i.e. the radial velocity divided by the virial velocity (v_{rad}/v_{vir}), in dependence of the virial radius $[0, 2]$, R_{vir}. Any subhalos with a non-zero star formation rate are indicated by triangles, the remaining subhalos are indicated by red crosses. The colour of the triangles represents the degree of blueness, i.e. $sSFR \cdot t_H$. The same scales and axis are used as in section 4.
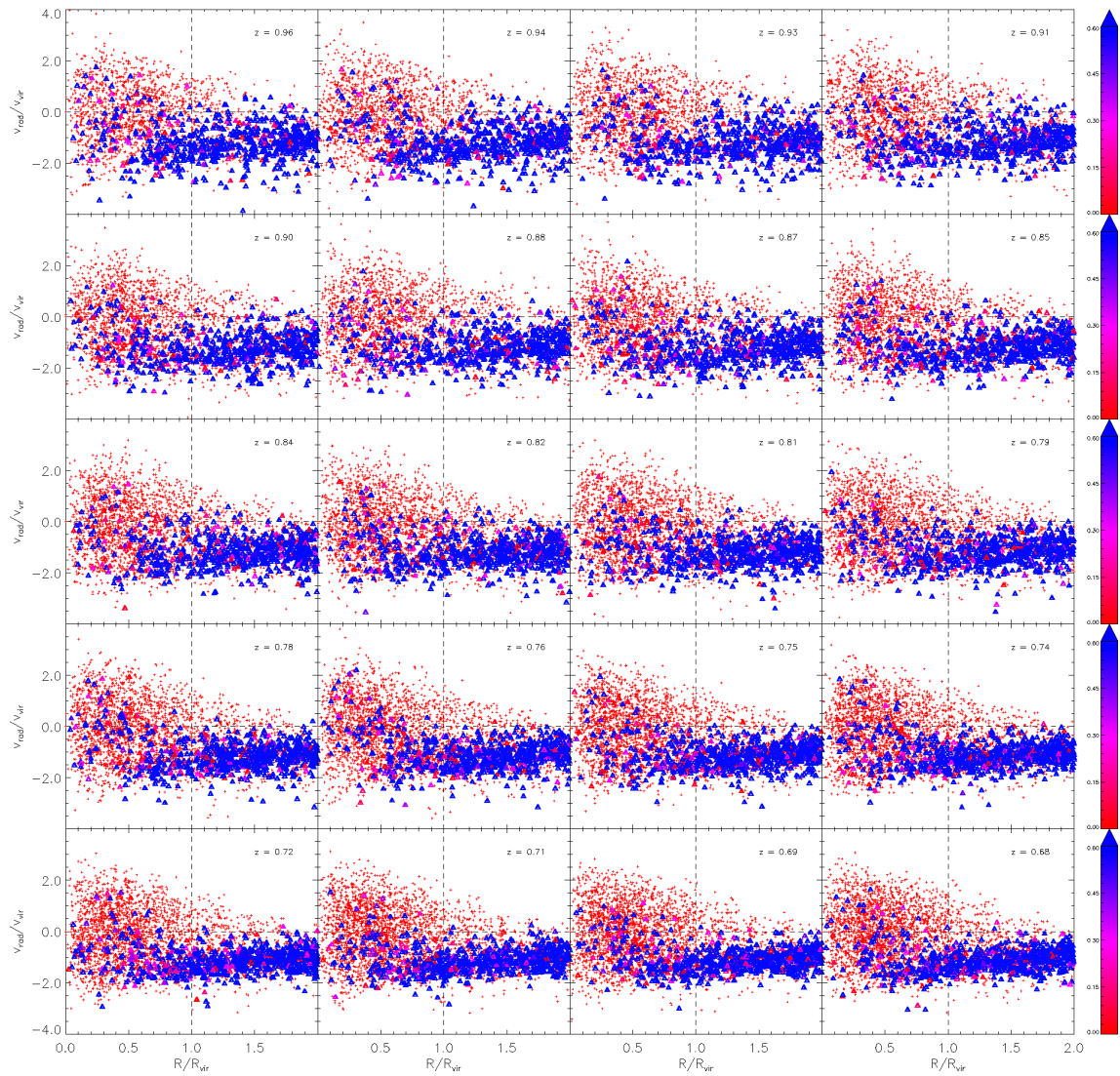
Figure 8.2: Same as Figure 8.1 but for $z = 0.96$-0.68.
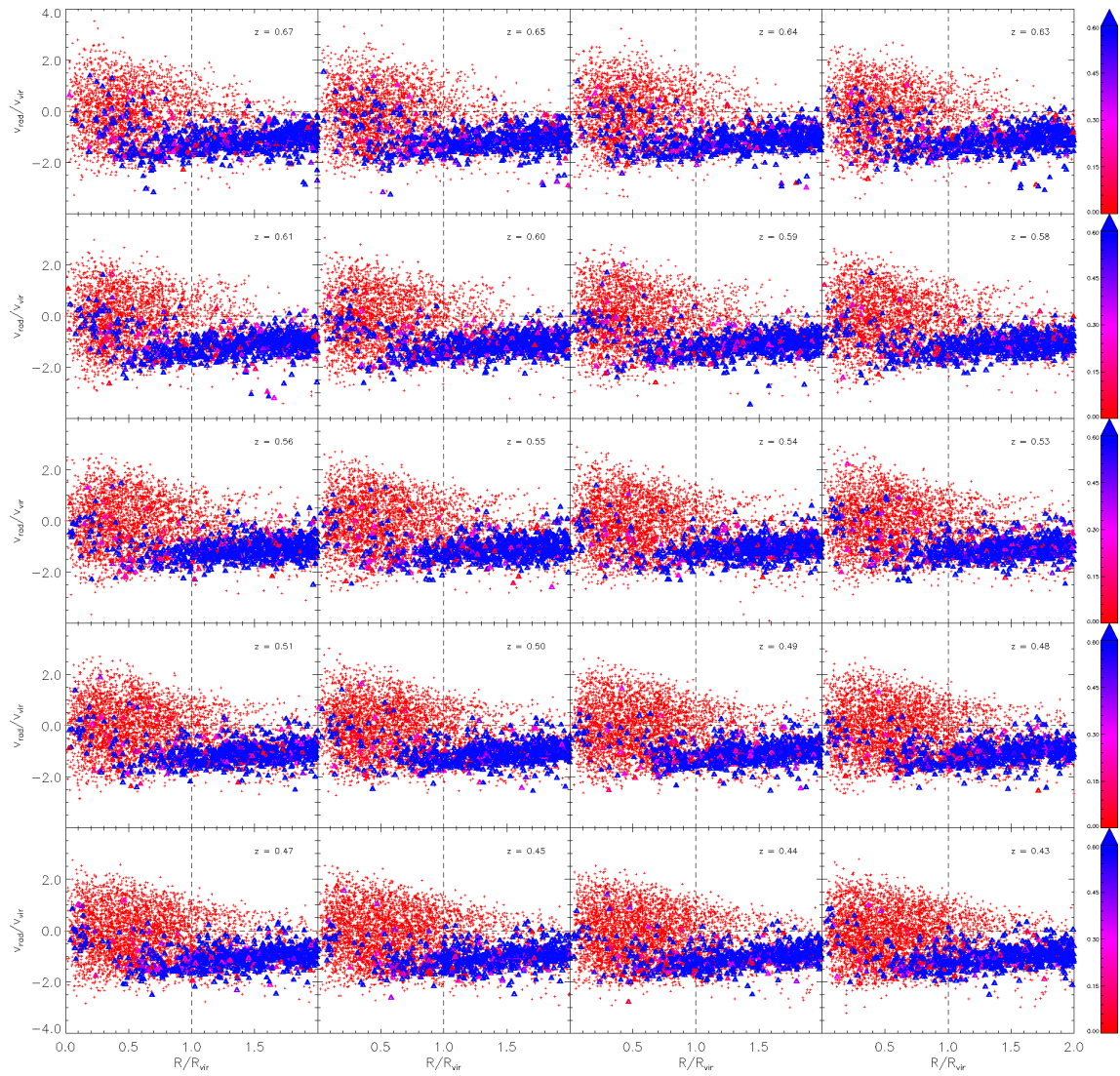
Figure 8.3: Same as Figure 8.1 but for $z = 0.67$-0.43.
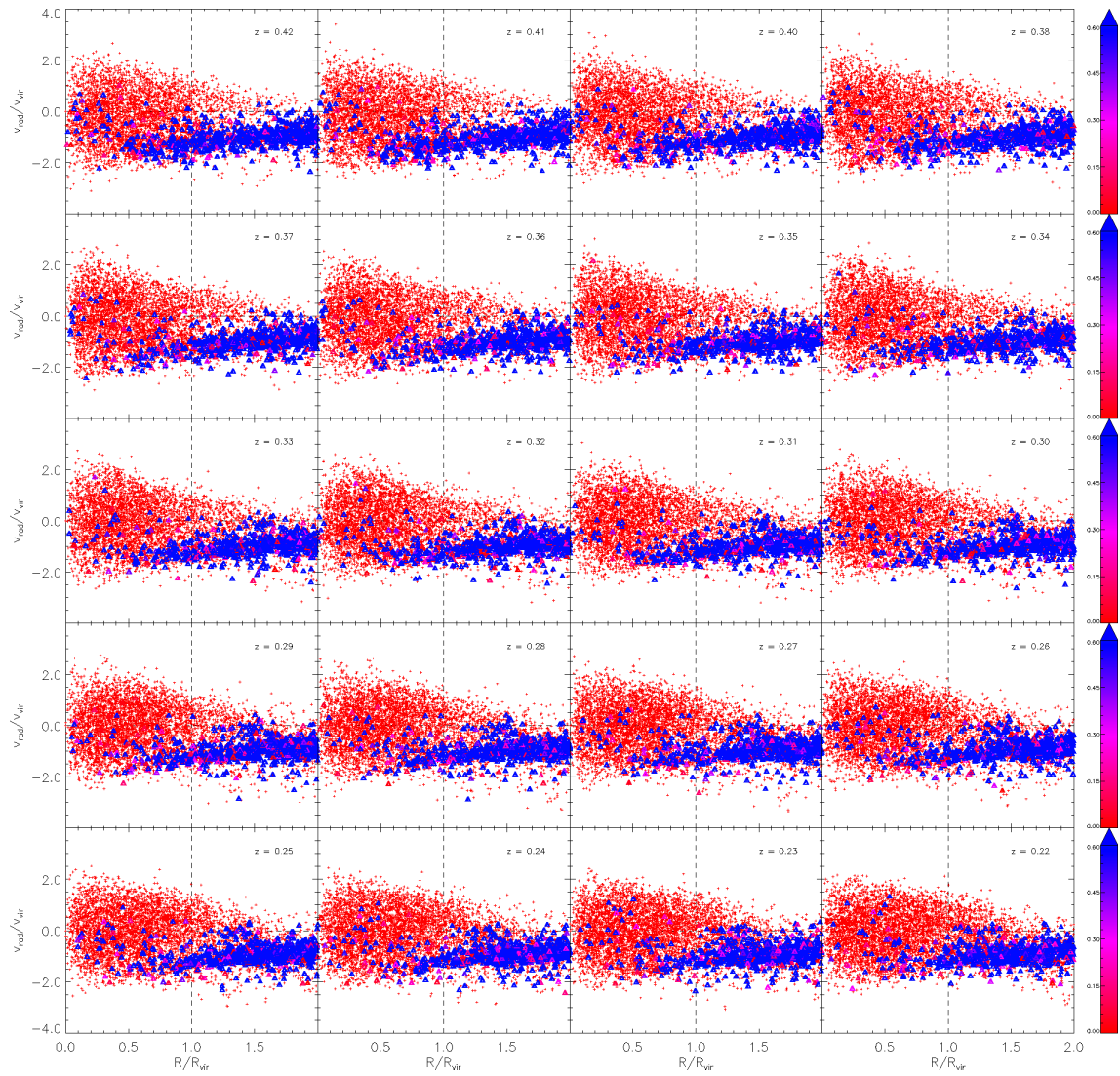
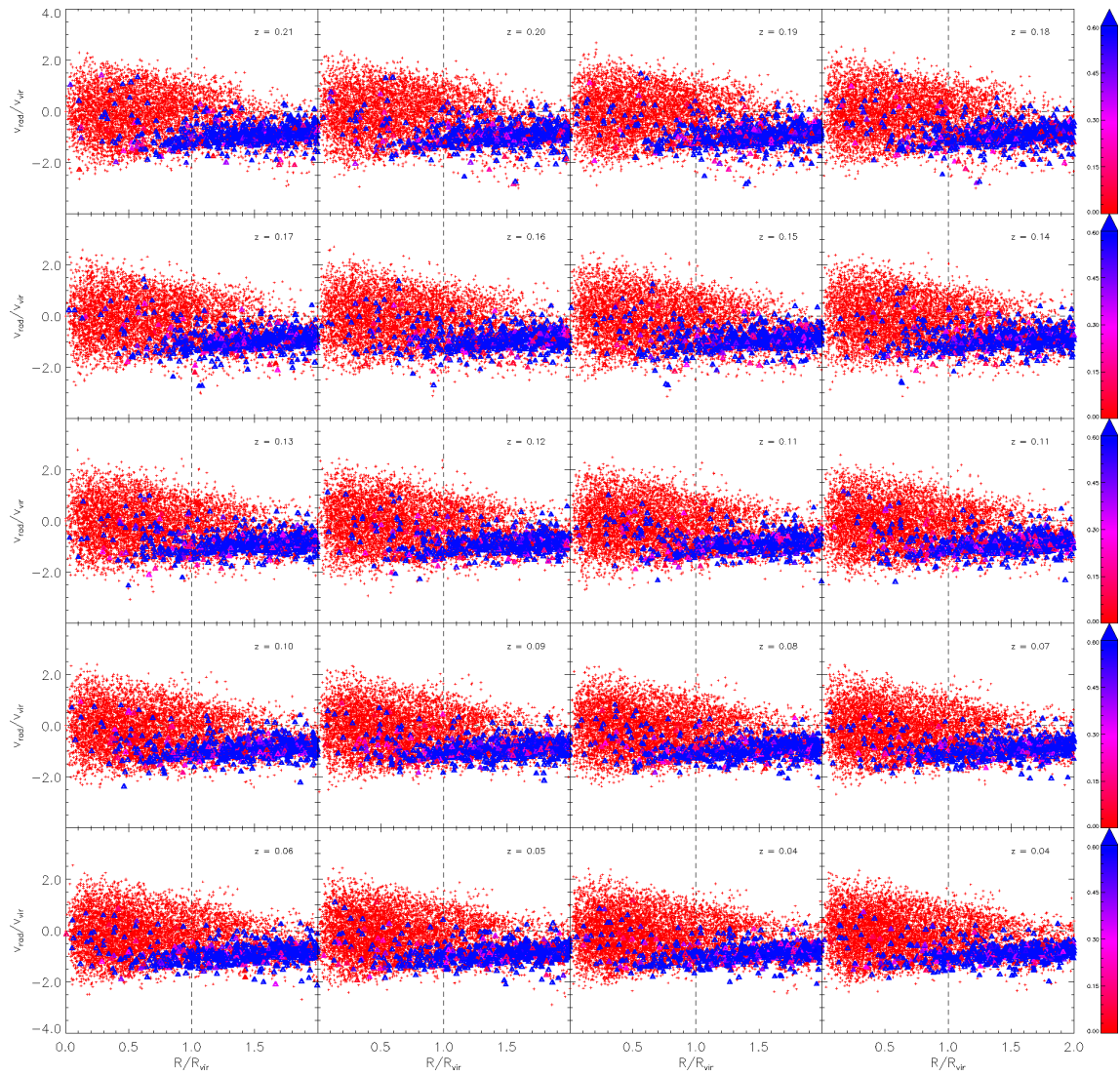**Figure 8.4:** Same as Figure 8.1 but for $z = 0.42$-0.22.

Figure 8.5: Same as Figure 8.1 but for $z = 0.21\text{-}0.04$.
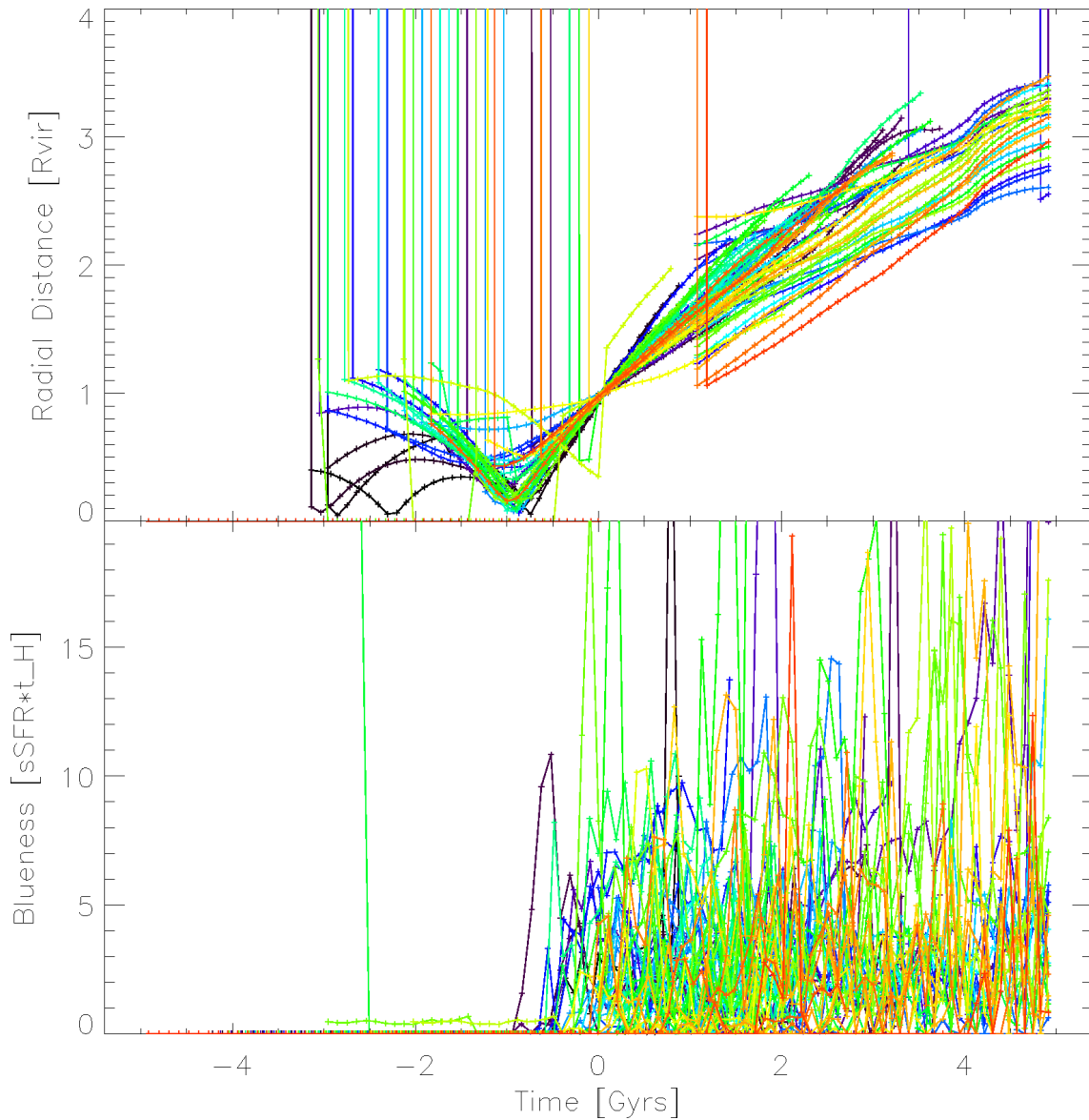
Figure 8.6: Failed shifted temporal evolution of subhalos with regard to their radial distance and blueness of the cluster with Halo ID = 004 at $z = 0.54$. Each line represents an individual subhalo tracked through time. The trajectories of the subhalos are shifted to the point where they pass below $1\,\mathrm{R_{vir}}$. Top panel: radial distance to the centre of the cluster in dependence of time. Bottom panel: blueness, i.e. specific star formation rate multiplied by the Hubble time, dependent on time. The failure of the merger trees drastically impacts the tracking of the radial distances in the top panel.
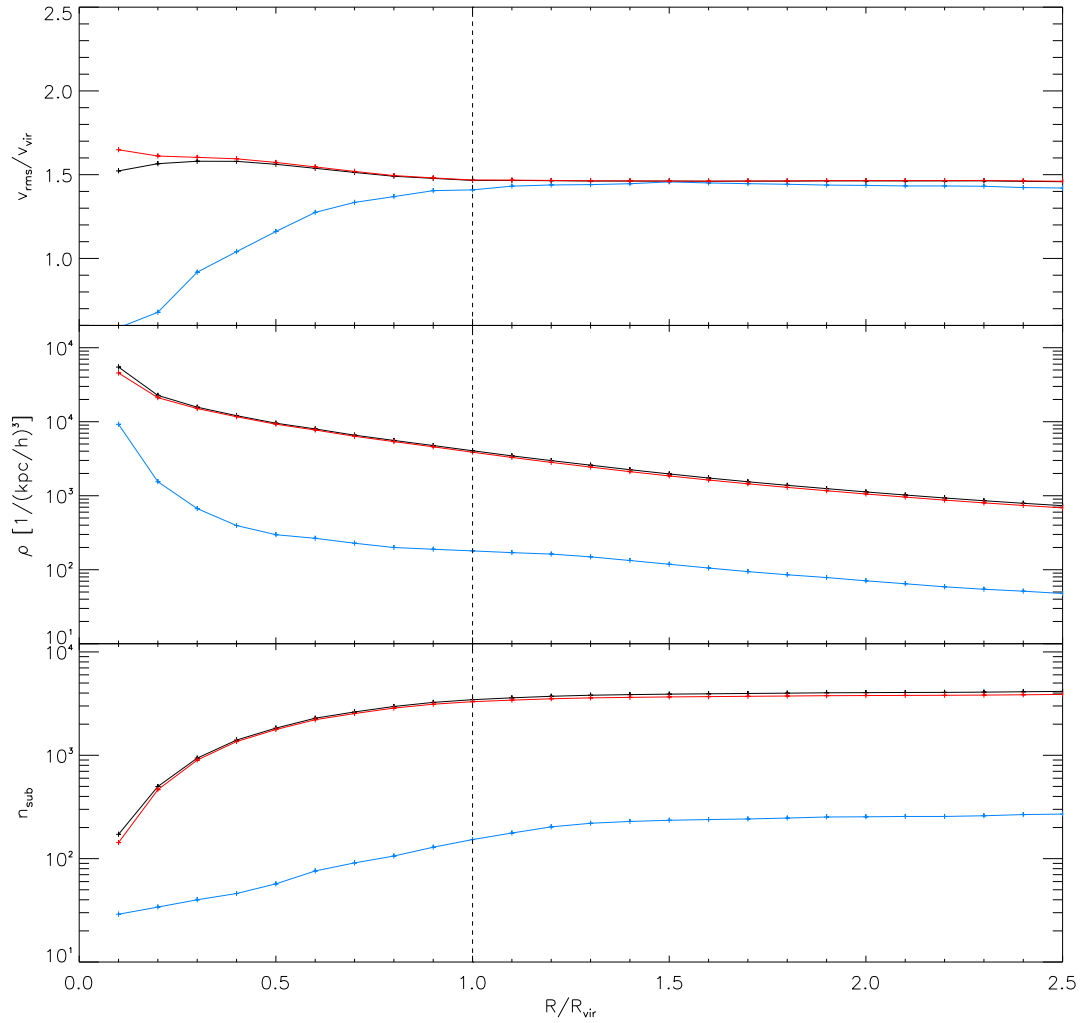
Figure 8.7: Cumulative radial profiles of 20 stacked Magneticum clusters at $z = 0.44$ for total population (black), star formers (blue) and quiescent (red) subhalos. Top panel: root mean square (rms) velocity normalised to the virial velocity v_{rms}/v_{vir}. Middle panel: radial number density profile in units of $[1/(kpc/h)^3]$. Bottom panel: number of subhalos in a given radial shell. The vertical dashed line corresponds to the virial radius.
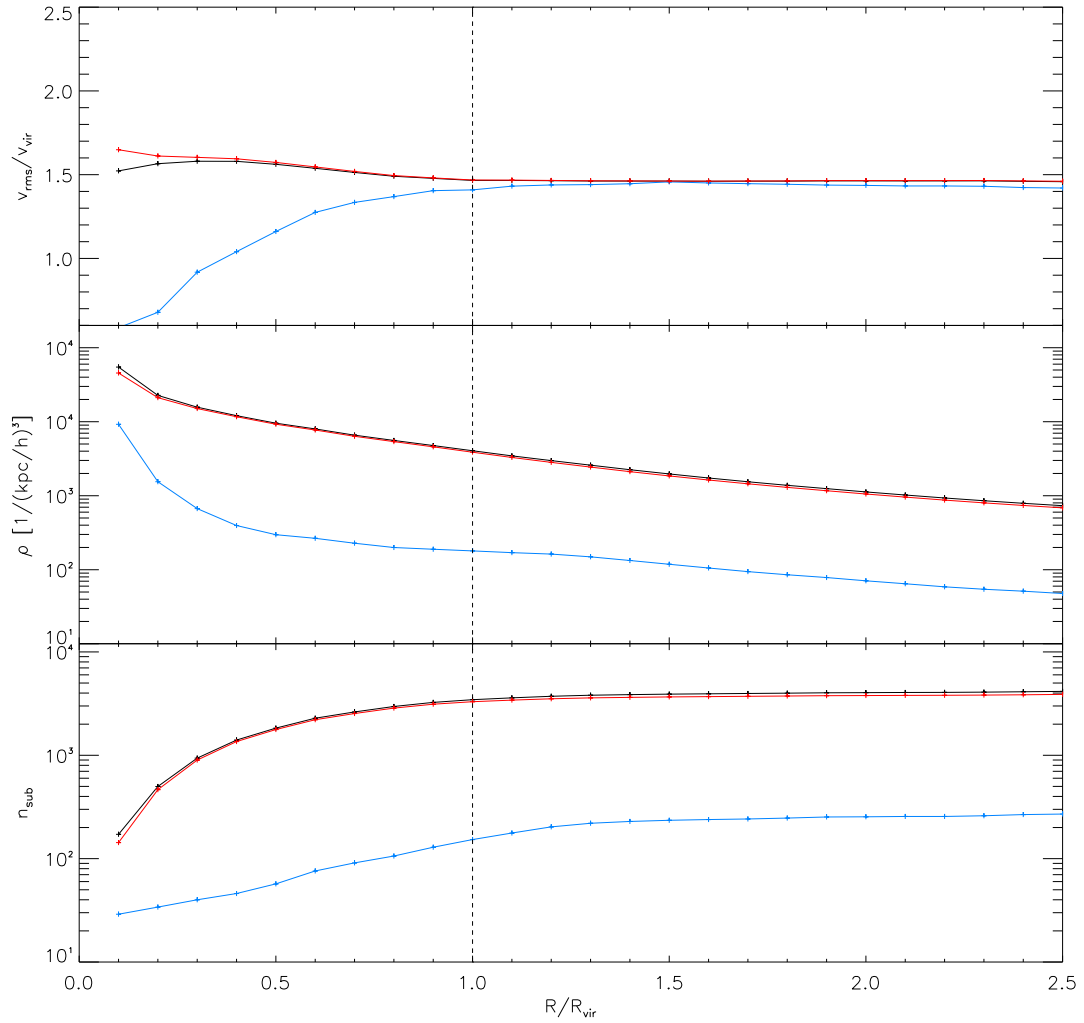
Figure 8.8: Cumulative radial profiles of 20 stacked Magneticum clusters at $z = 1.70$ for total population (black), star formers (blue) and quiescent (red) subhalos. Top panel: root mean square (rms) velocity normalised to the virial velocity v_{rms}/v_{vir}. Middle panel: radial number density profile in units of $[1/(kpc/h)^3]$. Bottom panel: number of subhalos in a given radial shell. The vertical dashed line corresponds to the virial radius.

Bibliography

Bahé, Y. M., McCarthy, I. G., Balogh, M. L., & Font, A. S. 2013, MNRAS, 430, 3017

Balogh, M. L., Navarro, J. F., & Morris, S. L. 2000, ApJ, 540, 113

Battaglia, G., Helmi, A., Morrison, H., et al. 2005, MNRAS, 364, 433

Beck, A. M., Murante, G., Arth, A., et al. 2016, MNRAS, 455, 2110

Bekki, K. 2009, MNRAS, 399, 2221

Bennett, C. L., Halpern, M., Hinshaw, G., et al. 2003, ApJS, 148, 1

Binney, J., & Mamon, G. A. 1982, MNRAS, 200, 361

Binney, J., & Tremaine, S. 1987, Galactic dynamics

—. 2008, Galactic Dynamics: Second Edition (Princeton University Press)

Biviano, A., Rosati, P., Balestra, I., et al. 2013, A&A, 558, A1

Braglia, F. G., Pierini, D., Biviano, A., & Böhringer, H. 2009, A&A, 500, 947

Butcher, H., & Oemler, Jr., A. 1978, ApJ, 219, 18

Clarkson, C. 2012, Comptes Rendus Physique, 13, 682

Conselice, C. J., Wilkinson, A., Duncan, K., & Mortlock, A. 2016, ApJ, 830, 83

Dehnen, W., & Aly, H. 2012, MNRAS, 425, 1068

Dickinson, M., Papovich, C., Ferguson, H. C., & Budavári, T. 2003, ApJ, 587, 25

Dolag, K., Borgani, S., Murante, G., & Springel, V. 2009, MNRAS, 399, 497

Dolag, K., Jubelgas, M., Springel, V., Borgani, S., & Rasia, E. 2004, ApJ, 606, L97

Dolag, K., & Stasyszyn, F. 2009, MNRAS, 398, 1678

Dolag, K., Vazza, F., Brunetti, G., & Tormen, G. 2005, MNRAS, 364, 753

Dressler, A. 1980, ApJ, 236, 351

Farouki, R., & Shapiro, S. L. 1981, ApJ, 243, 32

Fixsen, D. J. 2009, ApJ, 707, 916

Franx, M., van Dokkum, P. G., Förster Schreiber, N. M., et al. 2008, ApJ, 688, 770

Friedmann, A. 1922, Zeitschrift fur Physik, 10, 377

Gebhardt, K., Pryor, C., Williams, T. B., & Hesser, J. E. 1994, AJ, 107, 2067

Gunn, J. E., & Gott, III, J. R. 1972, ApJ, 176, 1

Guo, Q., White, S., Boylan-Kolchin, M., et al. 2011, MNRAS, 413, 101

Hansen, S. M., Sheldon, E. S., Wechsler, R. H., & Koester, B. P. 2009, ApJ, 699, 1333

Hirschmann, M., Dolag, K., Saro, A., et al. 2014, MNRAS, 442, 2304

Houghton, R. C. W. 2015, MNRAS, 451, 3427

Hubble, E. P. 1926, ApJ, 64, doi:10.1086/143018

—. 1936, Realm of the Nebulae

Iannuzzi, F. 2012, PhD thesis, Ludwig-Maximilians-Universität, `https://edoc.ub.uni-muenchen.de/15187/1/Iannuzzi_Francesca.pdf`

Kafle, P. R., Sharma, S., Lewis, G. F., & Bland-Hawthorn, J. 2014, ApJ, 794, 59

Kawata, D., & Mulchaey, J. S. 2008, ApJ, 672, L103

Komatsu, E., Smith, K. M., Dunkley, J., et al. 2011, ApJS, 192, 18

Larson, R. B., Tinsley, B. M., & Caldwell, C. N. 1980, ApJ, 237, 692

Lemaître, G. 1927, Annales de la Société Scientifique de Bruxelles, 47, 49

Lilly, S. J., Le Fevre, O., Hammer, F., & Crampton, D. 1996, ApJ, 460, L1

Ludlow, A. D., Navarro, J. F., White, S. D. M., et al. 2011, MNRAS, 415, 3895

Madau, P., Ferguson, H. C., Dickinson, M. E., et al. 1996, MNRAS, 283, 1388

Madau, P., Pozzetti, L., & Dickinson, M. 1998, ApJ, 498, 106

McCarthy, I. G., Frenk, C. S., Font, A. S., et al. 2008, MNRAS, 383, 593

McDonald, M., Benson, B. A., Vikhlinin, A., et al. 2014, ApJ, 794, 67

Mercurio, A., Rosati, P., Annunziatella, M., et al. 2014, in The evolution of galaxy clusters and cluster galaxies in the epoch of large optical/IR surveys, proceedings of a conference held 13-17 January, 2014 at the Sexten Center for Astrophysics, 12

Moore, B., Katz, N., Lake, G., Dressler, A., & Oemler, A. 1996, Nature, 379, 613

Moore, B., Lake, G., & Katz, N. 1998, ApJ, 495, 139

Navarro, J. F., Frenk, C. S., & White, S. D. M. 1997, ApJ, 490, 493

Oemler, Jr., A. 1974, ApJ, 194, 1

Planck Collaboration, Ade, P. A. R., Aghanim, N., et al. 2013, A&A, 550, A131

—. 2016, A&A, 594, A13

Remus, R.-S., Burkert, A., Dolag, K., et al. 2013, ApJ, 766, 71

Remus, R.-S., Dolag, K., Bachmann, L. K., et al. 2015, in IAU Symposium, Vol. 309, Galaxies in 3D across the Universe, ed. B. L. Ziegler, F. Combes, H. Dannerbauer, & M. Verdugo, 145–148

Remus, R.-S., Dolag, K., Naab, T., et al. 2017, MNRAS, 464, 3742

Richstone, D. O. 1976, ApJ, 204, 642

Robertson, H. P. 1935, ApJ, 82, 284

Sanders, B. C., Senden, T., & Springel, V. 2008, New Journal of Physics, 10, 125001

Sarazin, C. L. 1988, X-ray emission from clusters of galaxies

Slipher, V. M. 1917, The Observatory, 40, 304

Solanes, J. M., & Salvador-Sole, E. 1990, A&A, 234, 93

Solanes, J. M., Sanchis, T., Salvador-Solé, E., Giovanelli, R., & Haynes, M. P. 2002, AJ, 124, 2440

Springel, V., & Hernquist, L. 2003, MNRAS, 339, 289

Springel, V., White, S. D. M., Tormen, G., & Kauffmann, G. 2001, MNRAS, 328, 726

Springel, V., White, S. D. M., Jenkins, A., et al. 2005, Nature, 435, 629

Steinborn, L. K., Dolag, K., Hirschmann, M., Prieto, M. A., & Remus, R.-S. 2015, MNRAS, 448, 1504

Taylor, J. E., & Navarro, J. F. 2001, ApJ, 563, 483

Teklu, A. F., Remus, R.-S., Dolag, K., et al. 2015, ApJ, 812, 29

Toomre, A., & Toomre, J. 1972, ApJ, 178, 623

Tornatore, L., Borgani, S., Springel, V., et al. 2003, MNRAS, 342, 1025

Tornatore, M., Maier, G., & Pattavina, A. 2006, Journal of Optical Networking, 5, 858

Treu, T., Ellis, R. S., Kneib, J.-P., et al. 2003, ApJ, 591, 53

Trimble, V. 1995, PASP, 107, 1133

Umetsu, K., Medezinski, E., Nonino, M., et al. 2012, ApJ, 755, 56

van den Bosch, F. C., Aquino, D., Yang, X., et al. 2008, MNRAS, 387, 79

van der Marel, R. P. 1994, MNRAS, 270, 271

Verdugo, M., Ziegler, B. L., & Gerken, B. 2008, A&A, 486, 9

von der Linden, A., Wild, V., Kauffmann, G., White, S. D. M., & Weinmann, S. 2010, MNRAS, 404, 1231

Walker, A. G. 1935, The Quarterly Journal of Mathematics, 6, 81

Weinmann, S. M., Kauffmann, G., van den Bosch, F. C., et al. 2009, MNRAS, 394, 1213

Weinmann, S. M., van den Bosch, F. C., Yang, X., & Mo, H. J. 2006, MNRAS, 366, 2

Wetzel, A. R., Tinker, J. L., & Conroy, C. 2012, MNRAS, 424, 232

York, D. G., Adelman, J., Anderson, Jr., J. E., et al. 2000, AJ, 120, 1579

Zinger, E., Dekel, A., Birnboim, Y., Kravtsov, A., & Nagai, D. 2016a, MNRAS, 461, 412

Zinger, E., Dekel, A., Kravtsov, A. V., & Nagai, D. 2016b, ArXiv e-prints, arXiv:1610.02644

Erklärung:

Hiermit erkläre ich, die vorliegende Arbeit selbständig verfasst zu haben und keine anderen als die in der Arbeit angegebenen Quellen und Hilfsmittel benutzt zu haben.

München, 17 Juli, 2017

_____

Marcel Christopher Lotz